Nucleation and Growth of Group III-Nitride Nanowires

DISSERTATION

zur Erlangung des akademischen Grades
doctor rerum naturalium
(Dr. rer. nat.)
im Fach Physik

eingereicht an der
Mathematisch-Naturwissenschaftlichen
Fakultät I
Humboldt-Universität zu Berlin

von
Herrn Matthias Knelangen, M. Sc.

Präsident der Humboldt-Universität zu Berlin:
Prof. Dr. Jan-Hendrik Olbertz

Dekan der Mathematisch-Naturwissenschaftlichen
Fakultät I:
Prof. Stefan Hecht PhD

Gutachter:

1. Prof. Dr. Henning Riechert
2. Prof. Dr. Andreas Waag
3. Prof. Dr. Ted W. Masselink

eingereicht am: 19. November 2012
Tag der mündlichen Prüfung: 18. Oktober 2013

Abstract

This work covers the MBE growth and characterization of group III-nitride nanostructures. The work begins with the catalyst-free growth of GaN nanowires (NWs) on Si(111) by plasma-assisted MBE. The importance of substrate preparation and the formation of an amorphous SiN interlayer are described. GaN NWs are shown to nucleate as spherical islands and to furhter undergo a shape transition towards the NW geometry. The amorphous interlayer leads to a loss in epitaxial alignment and thus to NW tilt and coalescence. Coalescence leads to the formation of dislocations and stacking faults (SFs) in the NWs which greatly affect their optical properties. Dislocations are shown to have a detrimental effect on the optical quality, whereas SFs are shown to have a characteristic emission wavelength. By combining electron microscopy and cathodo-luminescence, the characteristic wavelength of the SF is determined.

Epitaxial growth of GaN on Si(111) can be achieved by using an AlN buffer layer. The nucleation and growth GaN NWs on AlN-buffered Si(111) is shown to happen via the pseudomorphical nucleation of spherical islands. As these islands grow, they undergo several characteristical shape changes, with the formation of facets in order to elastically relieve the lattice-mismatch induced strain. At a critical island size (and thus strain level), plastic relaxation happens by the formation of a misfit dislocation at the AlN/GaN interface. A subsequent transition to the NW geometry is observed, driven by the anisotropy of surface energies. Thus, the initial diameter of epitaxial catalyst-free GaN NWs is directly dependent on the lattice mismatch with the substrate.

The third part of this work covers the growth of (In,Ga)N/GaN NW heterostructures. GaN NWs with two stacked (In,Ga)N insertions are grown by MBE. The chemical composition is assessed by combining synchrotron-based HRXRD and a geometrical phase analysis of HRTEM micrographs. The structural analysis reveals that the (In,Ga)N insertions are embedded in the GaN matrix and that no plastic relaxation happens. The In content is shown to vary within a single insertion: The top region is more In rich due to In segretation during growth. The structure exhibits a strong green luminescence that is attributed to an *inter-well* transition between the stacked (In,Ga)N insertions.

Zusammenfassung

Diese Arbeit beschreibt das MBE-Wachstum und die Charakterisierung von Gruppe-III-Nitrid-Nanostrukturen. Die Arbeit beginnt mit dem katalysatorfreien Wachstum von GaN Nanosäulen (NW) auf Si(111) mittels plasmagestützter MBE. Die Substratpräparation und die Enstehung einer amorphen SiN-Zwischenschicht werden beschrieben. Es wird gezeigt, dass GaN NW als sphärische Inseln nukleieren und im weiteren Wachstum in eine NW-Geometrie übergehen. Die amorphe Zwischenschicht führt zum Verlust der epitaktischen Ausrichtung und somit zu gekippten Säulen und Koaleszenz. Diese Koaleszenz führt zur Enstehung von Versetzungen und Stapelfehlern in den Nanosäulen, welche einen starken Einfluss auf die optischen Eigenschaften haben: Während Versetzungen die Säulen optisch passivieren, haben Stapelfehler charakteristische Emissionen. Durch Kombination von Elektronenmikroskopie und Cathodolumineszenz wird die charateristische Wellenlänge eines Stapelfehlers gemessen.

Epitaktisches Wachstum von GaN auf Si(111) kann durch die Verwendung einer AlN-Pufferschicht erreicht werden. Die Nukleation von GaN auf AlN/Si geschieht in Form von sphärischen Inseln. Im weiteren Verlauf des Wachstums erfolgen mehrere charakteristische Formübergänge, bei denen Facetten gebildet werden, um die Verspannung durch Gitterfehlanpassung elastisch zu relaxieren. Bei einer kritischen Inselgrösse (und damit bei einem kritischen Spannungszustand) tritt eine platische Relaxation ein und es wird eine Versetzung an der AlN/GaN-Grenzfläche gebildet. Daraufhin tritt ein Übergang zur NW-Geometrie ein, welcher durch die Anisotropie der Oberflächen-Energien bedingt wird. Somit ist der ursprüngliche Durchmesser einer GaN Nanosäule direkt abhängig von der Gitterfehlanpassung zum Substratmaterial.

Der dritte Teil dieser Arbeit beschreibt das Wachstum von (In,Ga)N/GaN NW Heterostrukturen. Mit MBE werden GaN NW mit zwei (In,Ga)N-Einschlüssen gewachsen. Die chemische Zusammensetzung wird mittels einer Kombination von hochauflösender Röntgenbeugung und einer Gitterverzerrungsanalyse von hochaufgelösten transmissionselektronenmikroskopischen Aufnahmen bestimmt. Die Strukturanalyse zeigt, dass die (In,Ga)N-Einschlüsse vollkommen in die GaN-Matrix eingebettet sind und dass keine plastische Relaxation stattfindet. Die Heterostruktur weist eine starke Lumineszenz im grünen Spektralbereich auf, welche einem *Inter-Well*-Übergang zwischen zwei (In,Ga)N-Einschlüssen zugeschrieben wird.

Konsens ist Nonsens.

A. Okopenko

Selected publications

V. Consonni, **M. Knelangen**, U. Jahn, A. Trampert, L. Geelhaar and H. Riechert, *Effects of nanowire coalescence on their structural and optical properties on a local scale*, Appl. Phys. Lett. **95**, 241910 (2009)

V. Consonni, **M. Knelangen**, A. Trampert, L. Geelhaar and H. Riechert, *Nucleation mechanisms during self-induced growth of epitaxial GaN nanowires: Origin of their self-induced formation and radius*, Phys. Rev. B **81**, 085310 (2010)

M. Knelangen, V. Consonni, A. Trampert and H. Riechert, *In-situ analysis of strain relaxation during catalyst-free nucleation and growth of GaN nanowires*, Nanotechnology **21**, 245705 (2010)

V. Consonni, **M. Knelangen**, A. Trampert, L. Geelhaar and H. Riechert, *Nucleation and coalescence effects on the density of self-induced GaN nonwires grown by molecular beam epitaxy*, Appl. Phy. Lett. **98**, 071913 (2011)

V. Consonni, M. Hanke, **M. Knelangen**, L. Geelhaar, A. Trampert and H. Riechert, *Nucleation mechanisms of self-induced GaN nanowires grown on an amorphous interlayer*, Phys. Rev. B **83**, 035310 (2010)

M. Knelangen, M. Hanke, E. Luna, L. Schrottke, O. Brandt and A. Trampert, *Monodisperse (In,Ga)N insertions in catalyst-free-grown GaN(0001) nanowires*, Nanotechnology **22**, 365703 (2010)

B. Jenichen, O. Brandt, C. Pfüller, P. Dogan, **M. Knelangen** and A. Trampert, *Macro- & micro-strain in GaN nanowires on Si(111)*, Nanotechnology **22**, 295714 (2011)

J. Lähnemann, O.Brandt, C. Pfüller, T. Flissikowski, U. Jahn, E. Luna, M. Hanke, **M. Knelangen**, A. Trampert and H. Grahn, *Coexistence of quantum-confined Stark effect and localized states in an (In,Ga)N/GaN nanowire heterostructure*, Phys. Rev. B **84** 155303 (2011)

Contents

Chapter 1

Introduction

Group III-nitrides are widely considered as the material of choice for the fabrication of optoelectronic devices like lasers or LEDs, as the different alloys of (Al,Ga,In)N cover the entire visible spectrum from infrared to ultra-violet emission (see fig. 12-12 in [1]). However, bulk material of group III-nitrides is very expensive, therefore growth has to be realized by heteroepitaxy, i.e. on a different substrate materials. A possible candidate would be silicon carbide SiC, which has a hexagonal surface symmetry and a very similar lattice constant, but again it's a very expensive material and thus not suitable for mass production. Thus, in order to keep the production cost low and in order to integrate the devices within the silicon-based semiconductor industry processes, growth should be realized on silicon, namely Si(111) which has a hexagonal surface symmetry.

However, the lattice mismatch between GaN and Si(111) is quite large (approx. 17%) thus leading to a high defect density in the grown GaN, resulting in poor optical qualities. A solution to this problem is the growth of free-standing nanowires (NWs).

First reports on the growth of GaN NWs were given in 1998 by Sánchez-García *et al.* [2] and by Yoshizawa *et al.* [3] on Si(111) and sapphire substrates, respectively. The interest and relevance of group III-nitride NWs increased during the next years, as stated by Guha *et al.* [4] and Calleja *et al.* [5, 6]. Recently, molecular beam epitaxy (MBE) has established itself as a method of choice for the growth of GaN NWs [7], as it allows for relatively low growth temperatures, low growth rates and thus is suited for "engineering at the atomic scale".

Thus, the catalyst-free growth of GaN NWs on Si(111) has been established and applied to succesfully build optoelectronic devices like LEDs [8, 9]. However there is still a lack of understanding the exact relation between crystal structure of the NWs and their optical emission. Namely the effect of

crystalline defects on the optical properties has scarcely been investigated.

A further challenge is the understanding of the NW growth mechanisms. Whereas for the catalyst-assisted method, it is widely accepted, that growth occurs according to the vapor-liquid-solid (VLS) mechanism, described by Wagner and Ellis in 1964 [10], in the case of the catalyst-free, self-assembling growth, the mechanism of the initial NW formation remains and open question.

GaN NW heterostructures have been succesfully grown by MBE, namely (Al,Ga)N [11] and (In,Ga)N [12]. Especially the incorporation of In in the GaN NWs is of high interest, since the low fundamental bandgap [13] of 0.6-0.7 eV allows the emission in a wide spectral range, namely the visible light spectrum [14]. Recently, (In,Ga)N/GaN NW LEDs have been realized by Kishino *et al.* [8]. However the control of indium incorporation remains still a difficult task therefore precise band-gap tuning is still an issue.

In this work, I will address these three open questions.

Chapter 2 to 4 present some preliminary work, mainly the important structural properties of III-nitride nanowires, a litterature review on the state of the art on III-nitride nanowire research, as well as a presentation of the the main experimental methods used in this work: Molecular Beam Epitaxy (MBE) as the growth method of choice as well as the two major characterization techniques employed: Reflection High-Energy Electon Diffraction (RHEED) used to charaterize the growth process *in situ* (i.e. in the MBE chamber) and Transmission Electron Microscopy (TEM), as the *ex situ* characterization method of choice to investigate the NW's structural properties.

Chapter 5 covers the growth of free-standing GaN NWs on Si(111) substrates by catalyst-free plasma-assisted MBE. After a short overview of the growth modes available in MBE, the entire growth process is presented: substrate preparation prior to growth, surface nitridation of the Si(111) surface by the impinging N atoms, as well as the experimental conditions used in this study. A morphological investigation of the NWs is presented, focusing on NW tilt and in-plane orientation, two critical issues in nitrogen MBE growth on silicon. The structural properties of the NWs are investigated by TEM, namely the crystal orientation and the side facets. The optical properties of the NWs are investigated and the dependence on the growth conditions is discussed.

The second part of the chapter deals with a common problem in NW growth: coalescence. During growth, adjacent NWs may coalesce, thus creating a "polycrystalline" NW. The impact of the coalescence process on the structural and optical properties are investigated. It is shown that coalescence introduces two different structural defects: dislocations and stacking faults. These defects are highly localized within the NW thus affecting the

structural and optical properties on a *local* scale. Cathodoluminescence is carried out on selected single NWs thus giving direct evidence of the relation between crystal microstructure/defects and optical emission.

Chapter 6 discusses the *epitaxial* growth of GaN NWs on Si(111) wafers. Epitaxial orientation between substrate and NWs is achieved by the preliminary growth of an AlN buffer layer. This leads to an entirely different growth mechanism as now the two crystals grow in mutual alignment thus leading to an initial lattice mismatch of 2,54%, which has to be overcome during growth, as the fully grown GaN NWs are completely relaxed. The nucleation and growth process has been investigated by combining *in situ* RHEED and *ex situ* High Resolusion (HR) TEM. Is is shown that the self-induced growth of the GaN NWs is initially governed by the nucleation of dislocation-free coherent islands according to the Volmer-Weber growth mechanism. These islands develop through a series of shape transitions from spherical caps through truncated to full pyramids in order to elastically relieve the lattice-mismatch-induced strain. Subsequently, plastic relaxation takes place through the formation of a misfit dislocation at the AlN/GaN interface and a final shape transition to fully relaxed NWs occurs. The experimental critical radius for this final shape transition is compared to theoretical models, showing that plastic relaxation happens before the final shape transition takes place. This dislocation nucleation is asociated with a drastic change in the NW total free energy giving rise to a driving force for the final shape transition: the anisotropy of surface energy.

Chapter 7 presents the growth of (In,Ga)N/GaN NW heterostructures by catalyst-free MBE. Two vertically stacked fully embedded (In,Ga)N insertion were grown within free-standing GaN NWs. The chemical composition was investigated by high-resolution x-ray diffraction (HRXRD), which revealed two different In concentrations. The NWs were *locally* investigated by performing a Geometrical Phase Analysis (GPA) on HRTEM images of selected single NWs, which revealed that the (In,Ga)N insertions were coherently strained within the NW and have a mean In content of about 20%. The top region of these insertions has a significantly higher In content (40%), due to In segregation during MBE growth. To validate the obtained strain distribution, finite element simulations of the grown structure have been calculated. They strongly support and ineffective strain relaxation despite the NW geometry. Investigation of the heterostructure's optical properties reveals a strong emission at 2.3 meV, which is in apparent contradiction with the (In,Ga)N dimensions. This emission is attributed to an *inter*-well emission "through" the GaN barrier rather than an intra-well "pure" (In,Ga)N emission.

Chapter 8 concludes this work.

Chapter 2

Material properties

This chapter will briefly resume the properties of group III-nitrides as well as present characteristic properties of the NW geometry.

Importance of group III-nitrides

Si is the workhorse in the semiconductor industry due to its excellent properties for device applications. It is available on earth in large quantities and therefore relatively cheap and can be produced with excellent quality. It is the best investigated semiconductor material, driven by the industrial interest, and the technolgy to process Si is at a very high level. Other semiconductor materials have to show a considerable improvement in device performance in order to be considered as an alternative to Si.

A major disadvantage of Si (and germanium) is its indirect band gap, which makes it a bad candidate for optical (i. e. light-emitting) devices. As a result, other materials like arsenides and nitrides are considered as materials of choice for optoelectronics, as these materials have a direct band gap and cover a wide electromagnetic spectrum including the visible range.

Group III-nitrides are particularly interesting as they cover the entire visible range (roughly 400 nm to 700 nm). At room temperatures, the band gaps of the most common group III-nitrides InN, GaN and AlN are 0.7 eV, 3.42 eV and 6.2 eV respectively, thus (In,Ga,Al)N alloys span from infrared (IR) emission to deep ultraviolet (UV), as shown in fig. 2.1. This makes them perfect candidates for optical applications.

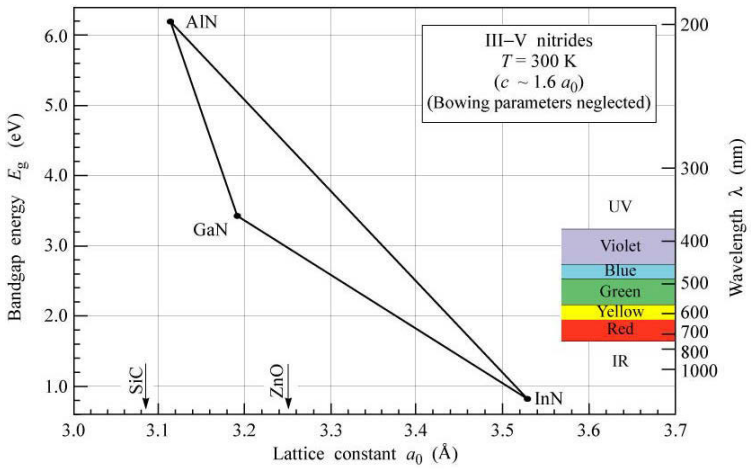

Figure 2.1 – Band gap (eV) vs. in-plane lattice parameter (Å) of selected semiconductor materials.

Crystal structure of group III-nitrides

Common III-V semiconductors like many arsenides (e.g. GaAs) and phosphides crystallize in the zinc-blende (ZB) or cubic structure, which is similar to the diamond structure of Si. The ZB structure consists of two interpenetrating fcc-lattices, one occupied by the group-III element (e.g. Ga) and one occupied by the group-V element (e.g. As).

The thermodynamically stable phase of bulk group-III nitrides is the wurtzite (WZ) or hexagonal structure, characterized by the in-plane lattice parameter a and the out-of-plane lattice parameter c. The hexagonal unit cell is depicted in fig. 2.3(a). Lattice parameters of group III-nitrides are listed in fig. 2.2.

The WZ and ZB structures are very similar. Both can be obtained by stacking atomic planes along the <111> axis, which in the hexagonal system is denoted by <0001>. The stacking orders for WZ and ZB structure is as follows: WZ: ...AaBbAaBbAaBb..., ZB: ...AaBbCcAaBbCc..., where capital letters represent group III atoms (Al, Ga, In) and lowercase letters represent

	a_0 (Å)	c_0 (Å)	C_{xx} (GPa)	C_{yy} (GPa)	C_{zz} (GPa)
AlN	3.112	4.982	410	389	125
GaN	3.189	5.186	390	398	105
InN	3.537	5.704	190	182	10

Figure 2.2 – Physical properties of group III-nitrides [15]

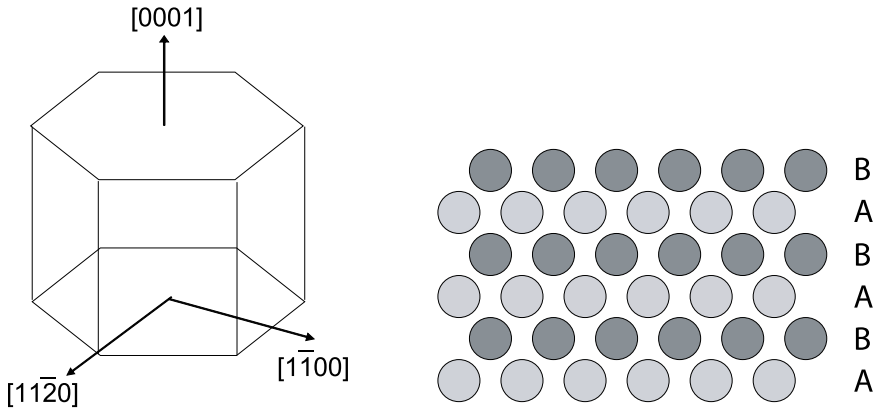

Figure 2.3 – GaN crystal schematics: (a) Hexagonal GaN unit cell, (b) Stacking sequence in the Wurtzite crystal structure

group V atoms (N). The WZ stacking is also presented in fig. 2.3(b).

Heteroepitaxy

Group III-nitrides are not found in mineral state (like for example Si) thus GaN substrates have to be grown, making it a very expensive material. Therefore group III-nitride nanostructures are usually grown by heteroepitaxy, i. e. on a different substrate material. In order to lower the preparation costs and in view of a possible implementation in the semiconductor industy, Si has been chosen as substrate material.

However, heteroepitaxy has several issues when compared to homoepitaxy (i. e. the growth of GaN on GaN for instance), namely thermal and lattice mismatch leading to material strain which is the main reason for defects in the grown crystal.

When a crystalline material A is grown on another crystalline material B, the lattice mismatch is given by $\delta a = (a_A - a_B)/a_A$. Although the materials bulk lattice constants may differ, in growth, they will always try to grow pseudomorphically, i. e. with corresponding crystal lattices. As the substrate B is a quasi infinite crystal and the grown material A will be present in very small quantity only, A will be strained due to the existing lattice mismatch.

A further source of strain is the difference in thermal expansion. MBE growth is carried out at relatively high temperatures (700-800 °C in the case of group III-nitride growth). After growth the sample is cooled down to room

temperature. As the thermal expansion of substrate and sample will differ, a further thermal strain will be induced.

These two issues may lead to a substantial strain level within the grown material leading to material defects, i. e. imperfections or mistakes in the regular periodic arrangement of atoms the crystal lattice. They can be classified as point, line, planar and volume defects. The presence of defects even in a very small amount can have an important impact on the structural and optical properties of the material. The two most critical extended defects are line defects (dislocations) and planar defects (stacking faults):

2.0.1 Dislocations

Dislocations extend through the crystal along one dimension of a crystal plane. A dislocation is caracterized by its line direction $\vec{l}$ (that is the extension direction of the defect) and its Burgers vector $\vec{b}$ which represents the displacement of the crystal lattice induced by the dislocation. Dislocations are classified in three groups, depending on the angle between line direction and Burgers vector: An *edge dislocation* is formed by the insertion of an extra half-plane into the crystal. The dislocation is the boundary of the inserted extra plane (cf. fig. 2.4a). The Burgers vector is perpendicular to the dislocation line: $\vec{b}\vec{p}\vec{l}$. A *screw dislocation* is formed by a slip of one part of the crystal with respect to the other along the line direction of the dislocation (cf. fig. 2.4b). The Burgers vector is parallel to the dislocation line: $\vec{b}\|\vec{l}$. Finally, a *mixed dislocation* presents both a srew and edge component.

2.0.2 Misfit dislocations

In the case of heteroepitaxy, when in-plane misfit strain is generated at the boundary of two crystals with different lattice parameters, strain may be plastically relieved by the insertion of misfit dislocations. These dislocations are edge-type dislocations that nucleate at the heterostructure interface and extend throughout the entire material and are thus called *threading dislocations* [16].

2.0.3 Stacking faults

Planar defects occur in crystalline materials wherevever the periodic structure of the material is interrupted across a unique plane. They are therefore characterized by the crystallographic indices of the plane and a displacement vector $\vec{R}$ specifying the relative difference of both crytal domains against each other. $\vec{R}$ is measured in sufficient distance from the strain field created by

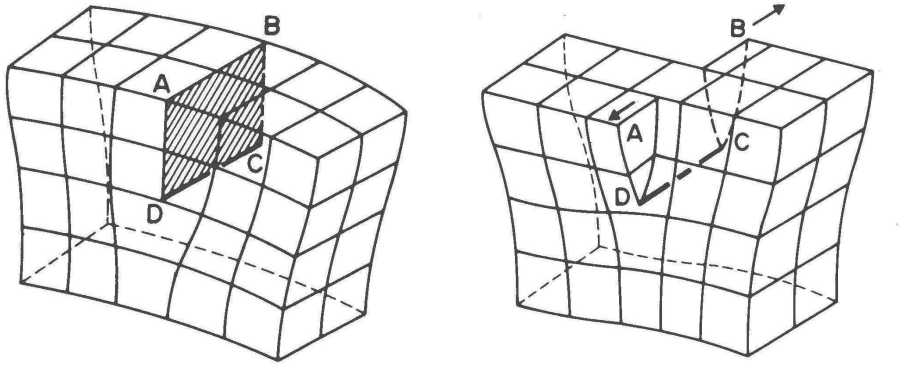

(a) **(b)**

Figure 2.4 – Planar defects in crystals: (a) Edge-type dislocation, (b) Screw-type dislocation [17]

the defect. The displacement vector $\vec{R}$ is formed by a lattice translation $\vec{T}$, sometimes a lattice inversion $\vec{i}$ is additionally involved. The most common planar defects in group III-nitrides are basal plane stacking faults.

A stacking fault is a local planar region in the crystal where the regular sequence of stacking is interrupted. Basal plane stacking faults are best described by the stacking sequence of the close-packed planes in the hexagonal structure. The stacking sequence of basal planes in a hexagonal structure is:

$$ABABABABAB\cdots \tag{2.1}$$

Basal plane stacking faults introduce a small region of face-centred cubic stacking (ABC).

- Stacking fault I_2 is formed by a slip of $\vec{R} = 1/3[1\bar{1}00]$:

$$ABABAB \quad ABCA \quad CACACA\cdots \tag{2.2}$$

- Stacking fault E is formed by the insertion of an extra half-plane: $\vec{R} = 1/2[0001]$:

$$ABABAB \quad ABCAB \quad ABABAB\cdots \tag{2.3}$$

- Stacking fault I_1 is a combination of slip and insertion of an extra plane: $\vec{R} = 1/3[1\bar{1}00] + 1/2[0001] = 1/6[2\bar{2}03]$:

$$ABABAB \quad ABC \quad BCBCBC\cdots \tag{2.4}$$

For the longest time, stacking faults have been considered non-radiative defects (similar to dislocations), thus deteorating the material's optical qualities. However, recent studies have shown the I_1 stacking fault to have a characteristic emission energy of 3.42 eV (see section 5.3).

Chapter 3

Nanowire review

This chapter will give a rapid overview on the state of the art in GaN NW research as of the beginning of 2007.

Nanowires

The word "Nanowire" (NW) consists of two parts: "nano" and "wire", characterizing its dimensions as well as the general aspect. As a "wire" (also called "column" or "rod") it's an object of relatively high aspect ratio (i.e. its length is usually much bigger than its diameter). The diameter is characterized by the word "nano", i.e. it lays in the nanometer range from 1-100 nm. The length of a NW can be several orders of magnitude higher than its diameter. Usual NWs have a regular footprint, which may be circular, square, triagonal or hexagonal.

Due to its very small footprint and their high aspect ratio, the NW geometry offers several advantages over the "classical" 2D layer. As the overall material volume of a NW is very small, the density of extended defects in NWs will be very low and defect-free NWs are possible. Furthermore, due to the small footprint of NWs on the substrate, it's possible to grow NWs on highly lattice-mismatched substrates without generating defects in the NW. The small footprint is also advantageous as it will reduce the densitiy of threading dislocations in the substrate material that will continue in the NW material. Threading dislocations have been shown to either stop at the interface between substrate and NW, or to bend towards the free surface of the NW and thus stop after several nm of NW growth, another advantage that's due to the very small lateral dimensions of the NW and the resulting large free surface. The combination of small footprint and free surface is also encouraging a very effective strain-relaxation, thus improving the material

quality of NW material when compared to 2D layers.

Besides pure material quality, NWs offer several other advantages like charge transport, mechanical properties and very effective light extraction.

NW fabrication techniques

The numerous fabrication techniques for NWs can be divided into two general fields: the *top-down* approach and the *bottom-up* approach. The *top-down* approach consists in building nanoscale objects from bulk material by a combination of lithography and etching, mostly building nanoscale patterns. This approach is the current standard in the semiconductor industry and thus is able to produce high quality objects, however, as the dimensions reach the nanoscale, processes become very complicated and cost-intensive. The biggest challenge in the conventional *top-down* approach is the lithography step: the minimum object size is directly dependent on the wavelength used in lithography. Therefore the use of conventional lithography is limited, whereas the electron beam lithography is very cost-intensive and thus no suitable technique for mass production. Another issue is the presence of structural defects in bulk material as nanoobjects are built: the presence of a single defect can completely deteriorate the structural properties of a nanowire.

The *bottom-up* approach builds nanostructures "the other way round": it uses well-definded nanoscale building blocks which are assembled to nanostructures. These nanostructures are "grown" by self-assembly, thus no mechanical or chemical fabrication processes are necessary and the material will not be subject to external mechanical forces during the fabrication process. Furthermore, the self-assembly severely limits the defect densitiy in the nanostructures. Finally, nanoobjects in the single digit nanometer scale can be fabricated by the *bottom-up* approach.

The first report of growing NWs by the *bottom-up* approach is given in the 1950's, when mercury (Hg) whiskers were grown from vapor phase on a glass plate [18]. However, it's the work by Wagner and Ellis in 1964 [10], that is widely considered to be the first succesful NW growth: Si NWs where grown with the use of gold (Au) as a catalyst, thus defining the Vapor-Liquid-Solid growth mechanism. In the 1970's, Bootsma and Gassen [19] as well as Givargizov [20] used Chemical Vapor Deposition (CVD) to grow Si and Ge whiskers, again with the use of Au as a catalyst. With advancing technology is was possible to use metalorganic precursor materials. Today, the two main fabrication techniques for NWs are Metalorganic Vapor Phase Epitaxy (MOVPE) and Molecular Beam Epitaxy (MBE).

GaN NWs by MBE

The first report of MBE-grown GaN NWs were given in the late 1990's by Sánchez-García *et al.* [2] and by Yoshizawa *et al.* [3] on Si(111) and sapphire substrates respectively. The interest in MBE-grown GaN NWs was testified by several following works like Guha *et al.* [4] and Calleja et al. [5, 6]. Since then, the growth of group III-nitride NWs has received an exponential interest and several groups have dedicated their research to these nanostructures. Recently, the first GaN NW LED has been achieved by MBE growth as reported by Kikuchi et al. in 2004 [8].

The growth of GaN NWs by MBE can be devided into two different methods: the *catalyst-assisted* growth and *catalyst-free* growth.

In the case of catalyst-assisted growth, a metallic particle (Au, Ni, ...) is used as a catalyst, i.e. the Ga adatoms on the substrate's surface are "captured" by the caralyst particle, a Ga supersaturation is reached within the catalyst and GaN growth is initiated beneath the catalyst particle. As the particle is generally in liquid form throughout the growth process, the catalyst-assisted growth is generally considered to follow the Vapor-Liquid-Solid growth process [10]. The NW position and diameter are directly given by the catalyst parcticle's position and size, respectively, thus the NW growth can be controlled through engineering of the seed particles.

However, group III-nitride NWs may also be grown by *catalyst-free* MBE, where group III atoms and nitrogen atoms are impinging on a hot surface and *spontaneously* nucleate and grow as NWs. Although GaN, (Al,Ga)N and InN NWs have been successfully grown and even (Al,Ga)N/GaN NW heterostructures have been realized, little is known about the underlying growth mechanism beyond the fact that N-rich conditions are necessary to obtain catalyst-free NW growth.

N-rich conditions are reached by obtaining a high local V/III ratio during growth, which is generally achieved either by directly supplying a high amount of atomic nitrogen and less Ga or by rising the substrate temperature during growth. Rising the substrate temperature will increase Ga desorption and thus lead to *locally* N-rich conditions at the substrate surface. It has thus been observed by Calleja *et al.* that by increasing the V/III ratio or the substrate temperature, the GaN morphology changes from a smooth 2D layer via a rough 2D layer to coalesced NWs and finally free-standing "single" NWs [7].

Catalyst-free GaN NWs have been grown by MBE on various substrates, with SiC, Al_2O_3 and Si being the most prominent ones, the former two because of their good lattice matching, the latter one due to technological reasons and ease of supply. On Si, growth has been achieved on two different

crystal orientations: Si(100) and Si(111), the latter being considered as better suited as it offers a hexagonal surface symmetry, like the group III-nitrides.

The as-grown free-standing NWs have been found to be of very good crystal quality, free of extended defects and present atomically sharp side and top facets. Optical studies of GaN NWs have shown that the NWs are strain-free [6, 21, 22]. Growth on bare Si has been found to lead to a thin Si_xN_y film between substrate and NWs. In order to avoid this, an AlN buffer layer of about 100 nm thickness is deposited on the Si surface prior to GaN growth.

(Al,Ga)N NWs have been succesfully grown on Si and sapphire substrates and recently, the first succesful growth of InN NWs has been reported (see [7] and references therein). The growth on InN poses a specific problem related to the fact that InN dissociates at temperatures above 550°C. As a high temperature is a prerequisite for N-rich growth conditions, catalyst-free InN growth still presents several technical issues.

In order to build functioning optoelectronic devices based on NWs, the growth of NW heterostructures are very interesting. Recently, Ristic *et al.* have grown (Al,Ga)N/GaN nanocolumnar heterostructures with several GaN quantum disks embedded in an (Al,Ga)N NW, by simple interruption of the Al flux during the growth of (Al,Ga)N [23]. A characteristic emission was recorded by the embedded GaN quantum disks.

Open questions

Although different group III-nitride NW structures have been successfully grown by catalyst-free MBE, there are still several important open questions:

1. The nucleation: Free-standing NWs can be grown on different substrates. However little is known about the nucleation phase, for instance the growth mode. Both Stranski-Krastanov growth and Volmer-Weber growth are possible under N-rich conditions.

2. Structural and optical properties: Although optical studies have been carried out and the first optoelectronical devices have been built, the influence of the NW structure on the optical properties has scarcely been investigated.

3. Strain: Several optical studies have shown that free-standing NWs are strain-free. It would be interesting to verify this result by an in-depth structural study, possibly taking into account the nucleation phase.

4. (In,Ga)N NWs: (In,Ga)N is the most interesting group III-nitride alloy as it allows emission in the visible spectral range. However, no (In,Ga)N/GaN NW heterostructures have been built. As a consequence, there is no knowledge about the feasibility and the structural and optical properties of such a nanostructure.

Chapter 4

Experimental methods

This chapter will present the main experimental methods and setups that were employed in this work. The nanowire samples presented in this work have been exclusively grown by catalyst-free plasma-assisted molecular beam epitaxy. *In situ* monitoring of the growth has been performed by reflection high-energy electron diffraction. *Ex situ* structural characterization has been carried out by high-resolution transmission electron microscopy.

Molecular Beam Epitaxy

Molecular Beam Epitaxy (MBE) is a well-established method to produce high-quality layers and nanostructures of different materials. An introduction to MBE growth can be found in the review by J. R. Arthur [24].

As the word *epitaxy* suggests (grom the greek *epi* = "on" and *taxis* = order), in an MBE system, the material grows in an ordered way on a provided substrate. The MBE technique is characterized by the following main features:

As the name suggest, the material is grown by molecular (or atomic)

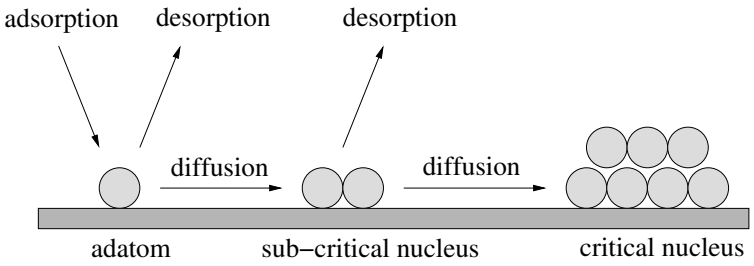

Figure 4.1 – Principles of MBE growth showing the competition between adsorption and desorption as well as the critical role of surface diffusion.

precursors, that is single moleculs or atoms impinging on the substrate and react there to form the grown material. In the case of group III-nitride growth, one of the precursors is a group III-metal, whereas the other is atomic nitrogen. The atomic flux of the metal species is generated by an effusion cell, in which the liquid metal is heated so as to reach a high pressure in the vapor phase and thus generate the atomic beam aimed at the substrate. Atomic nitrogen is provided by a plasma source, where provided N_2 molecules are dissociated to nitrogen atoms in a high-frequency plasma. The atoms of metal and gas species react on the hot substrate surface to form the final nitride material.

MBE growth is carried out in an ultra high vacuum (UHV) chamber with a background pressure of less than 10^{-9} mbar. As the material growth occurs by reaction of atomic species on the substrate surface, UHV conditions are essential to MBE growth, as higher pressures would result in the incorporation of impurities in the grown material or might even favor recombination before the substrate is reached.

The UHV conditions bear two substantial and characteristic advantages for MBE over other growth techniques: The surface diffusion of adatoms on the substrate surface is very high. Thus, high material quality is reached and atomically sharp interfaces between heterostructures can be grown. Furthermore, it allows the use of in-situ characterization techniques. A detailed description of *in situ* monitoring of the growth process by reflection high-energy electron diffraction is given below.

A simple scheme of the surface dynamics during MBE growth is shown in fig. 4.1. The nucleation process is governed by the competition between adsorption of impinging atoms, diffusion of the adatoms and desorption (re-evaporation). An atom is adsorbed to the surface, it may desorb or diffuse on the surface to encounter other adatoms and form a metastable (i. e. subcritical) nucleus. This nucleus may coarsen to reach the critical size and stabilize on the surface. This will initiate material growth.

In MBE, layers and nanostructures are grown far from thermodynamic equilibrium. As a result, kinetic processes at the substrate surface play an important role in the growth process. Impinging atoms or molecules are *adsorbed* (*physisorbed*) to the substrate surface. The adsorbed species then diffuse on the surface until they are either incorporated into the crystal lattice (*chemisorbed*) or re-evaporated (*desorbed*).

If the atom is incorporated into the crystal lattice, growth takes actually place. Surface kinetics will determine the growth mode that will be adapted. Three basic growth modes may take place in MBE (see fig. 4.2):

- In the *Frank-van der Merwe* (FM) or layer-by-layer growth mode [25],

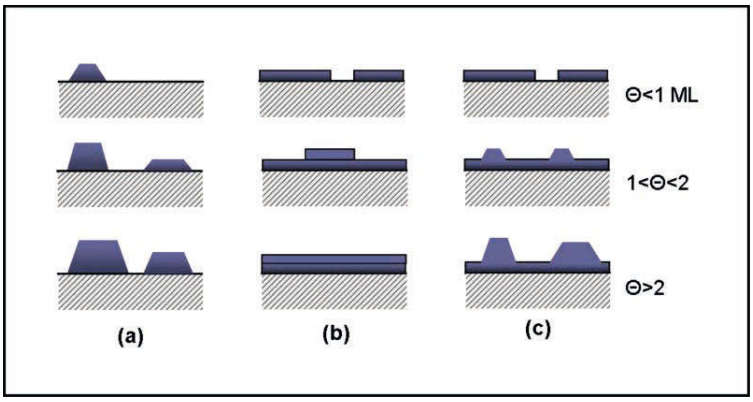

Figure 4.2 – Schematic diagram of the three basic MBE growth modes: (a) Volmer-Weber or 3D growth, (b) Frank-van-der-Merwe or 2D growth, (c) Stranski-Krastanov or layer+island growth. θ denotes the surface coverage in atomic mono layers (ML).

the interaction between substrate and layer atoms is stronger than between neighbouring layer atoms. Each new layer starts to grow only when the last one has been completed.

- The opposite case, *Volmer-Weber* (VW) or 3D growth mode [26], takes place, when the interaction between neighbouring deposit atoms exceeds the interaction between deposit and substrate. In that case, a 3D island (i.e. a multilayer conglomerate of adsorbed atoms) is formed.

- The *Stranski-Krastanow* (SK) or layer-plus-island growth mode [27] is an interesting intermediate case. After the formation of one, or several, complete 2D monolayers (*wetting layers*), 3D island formation occurs. These islands grow on top of the first full 2D layer(s).

Many factors may account for the occurrence of a certain growth mode, mainly surface and interface energies, the wetting behaviour of the deposit material as well as the lattice mismatch between substrate and deposit material.

In the case of NW growth, the two possible growth modes are the Stranski-Krastanow and Volmer-Weber growth modes, which both result in 3D islands that may lead to free-standing NWs. Therefore the presence or absence of a wetting layer will inform about the occuring growth mode.

MBE growth in this work was carried out on a RIBER system equipped with standard effusion cells for gallium, aluminum and indium for group III supply and an OXFORD plasma cell for N_2 supply.

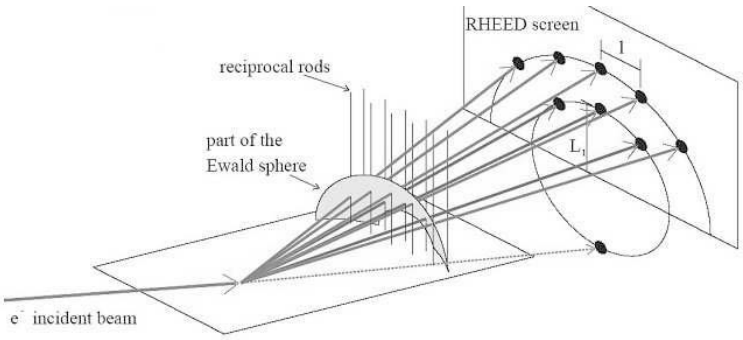

Figure 4.3 – Schematic illustration of the diffraction geometry in RHEED [29]

Reflection High-Energy Electron Diffraction

One of the main advantages of MBE in comparison to other epitaxial growth techniques is the possibility to monitor the growth process by *in situ* electron diffraction, due to the very low pressure in the MBE growth chamber. The most common employed technique is reflection high-energy electron diffraction (RHEED). A brief description of the RHEED technique as-well as an illustration of typical RHEED patterns will be given below. Further information can be found in ref. [28].

RHEED is based on the reflection of electrons with high kinetic energy (typically around 20 keV) and low incident angle (below 5 °) from the surface of a solid. The electrons will be scattered by the atomic planes of the crystal resulting in a reciprocal space representation of the investigated material. The recorded diffraction pattern is therefore the result of the intersection of the reciprocal lattice with the Ewald sphere. Figure 4.3 shows a schematic picture of the RHEED geometry. In the case of a crystalline material, the diffraction pattern allows for a *direct* measurement of the inter-plane distances $d_{\|}$, thus allowing to measure the strain state at the growth front of the material.

A characteristic property of RHEED is the grazing incidence of the electron beam. Due to the very low incident angle, only the diffraction pattern of the top 3-5 monolayers (ML) of a compact material can be recorded as the signal of deeper material layers will be lost to multiple inelastic and diffuse scattering. Therefore RHEED offers a very high surface sensibility and is of high interest to material science as it permits to investigate the physical processes that happen at the growth front.

In kinematical scattering, the possible reflections are determined by the condition that the incident wave vectors $\vec{k_0}$ and $\vec{k}$ of the incident and refracted

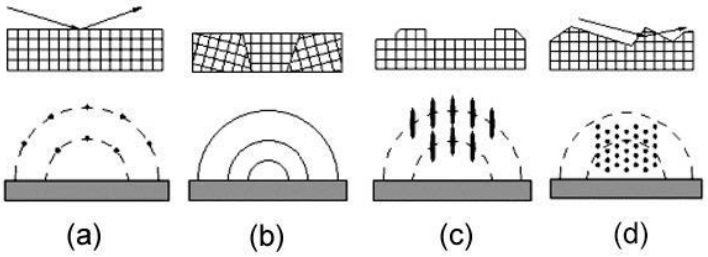

Figure 4.4 – RHEED patterns of various crystalline surfaces [30]

beams differ by a reciprocal lattice vector $\vec{G}$:

$$\vec{G} = \Delta\vec{k} = \vec{k} - \vec{k_0} \tag{4.1}$$

As the kinematic energy of multiply scattered electrons is very low compared to single scattered electrons, it is safe to neglect the contribution of multiply scattered electron to the intensity of the RHEED pattern, therefore considering only elacstic scattering, i. e. $|\vec{k}| = |\vec{k_0}|$. In that case, the diffraction condition can be cast into the geometrical construction of the Ewald sphere.

Diffraction spots will appear on the RHEED screen in the case of constructive interference according to the Bragg conditions:

$$2d \sin\theta = \lambda \tag{4.2}$$

the lattice constant $d_{\|}$ can be derived from the horizontal distance between two adjacent spots on the RHEED screen L:

$$d_{\|} = \frac{L \cdot \lambda_0}{t} \tag{4.3}$$

where λ_0 is the wavelength of the incident electron beam and t the distance between sample and RHEED screen. Thus RHEED permits an *in situ* measurement of lattice constants.

In the case of NW growth, the diffraction process is influenced by the NW morphology. As NWs are nanocrystals with vertical sidewalls and a small diameter, transmission diffraction through the NWs will take place. Therefore the RHEED pattern will undergo a characteristic transition from reflection diffraction to transmission diffraction as NW nucleation proceeds.

RHEED allows the structural investigation of the observed crystal lattice (this will be treated in detail at the beginning of chapter 4) but is also

sensitive to surface morphology. Figure 4.4 shows four characteristic surface morphologies as well as the corresponding RHEED patterns.

In the case of a specular monocrystalline substrate surface, Laue circles with diffraction spots are observed. If the surface is reconstructed, the RHEED pattern will show additional reflections depending on the surface reconstruction (fig. 4.4a). If the surface is polycrystalline, the electrons are diffracted equally in all directions, therefore concentric arcs will be observed by RHEED (fig. 4.4b). In the case of a non-ideal surface presenting surface steps of 1 ML in height, the spots will be elongated and form streaks (fig. 4.4c). Therefore this RHEED pattern is commonly named *streaky*. This is the typical pattern that will be observed in the case of layer growth in MBE. If the surface presents a very high roughness or 3D objects like quantum dots or NWs, transmission electron diffraction through these objects will happen. The resulting pattern presents diffraction spots according to the Bragg diffraction rules (fig. 4.4d). This pattern geometry is typical for nitride NW growth. If the substrate surface is not crystalline, no electron diffraction will take place and all electrons will be scattered by diffuse scattering. Therefore no pattern can be observed in RHEED as only a diffuse intensity is recorded.

RHEED investigation in this work was carried out with an acceleration voltage of 20 kV and an electron beam current of 20 µA. The incident angle of the electron beam was 3 °.

Transmission Electron Microscopy

This paragraph will give a brief introduction to transmission electron microscopy (TEM). As for the characterization of nanowires, bright field conventional TEM and high-resolution TEM (HRTEM) are the structural characterization methods of choice, they will be presented here. For further information, please consider references [31] and [32].

TEM is based on the interaction between an electron and the specimen. Electron-specimen interaction can be grouped into *elastic scattering*, where the electrons are scattered by the Coulomb force interaction between incident electrons and the electrostatic field of the specimen atoms but conserve their kinetic energy, and *inelastic scattering*, where the electron's kinetic energy is not conserved. Elastically scattered electrons are the major source for imaging in bright-field TEM and HRTEM modes.

TEM imaging based on elastically scattered electrons is thus able to give very exact information on the geometry of the scattering specimen, that is the crystal lattice, but will give less information about the nature of the

crystal's atoms. By using HRTEM, the crystal lattice can be imagined with the highest precision so as to investigate the crystal symmetry, stacking and the presence and nature of extended defects. No information however is directly obtained on the specimen's chemical composition

In the case of binary group III-nitrides, the chemical composition is given by the growth conditions, so TEM analysis focuses on structural characterization. For that matter, the used imaging modes only involve elastical scattering.

TEM investigation in this work was carried out at a JEOL 3010 microscoope with an acceleation voltage of 300 kV. Samples were prepared by mechanical grinding, polishing and ion sputtering.

Chapter 5

GaN nanowires on silicon

This chapter presents the growth of GaN NWs by MBE on Si(111). First, the sample preparation and growth process is described. The nitridation of the Si surface is shown. Nucleation of GaN NWs is investigated and shown to happen via a shape transition from cap-shaped islands to NWs. A brief morphological and structural study of the NWs is given. The second part of this chapter focuses on the important issue of NW coalescence. The coalescence process is analyzed, the resulting structural defects and optical properties are discussed in detail. Finally a comprehensive study of the main growth parameters is given in order to reduce the NW surface density and thus the NW coalescence degree.

5.1 Nucleation and growth process

5.1.1 Surface preparation

As discussed in chapter 2, MBE permits to grow single atomic layers of material with high precision and therefore offers the possibility of material engineering at the atomic scale. Growth is carried out at high temperature and in UHV conditions so as to guarantee quasi contamination-free growth. Specimen preparation prior to growth is therefore of highest importance.

The substrate of choice for this work is Si(111). As Si is the most widely used material in semiconductor industry, high quality samples are available at low cost. Due to experimental reasons, 2 inch Si(111) wafers have been used for this work. The wafers can be bought "epi-ready" from the manufacturer. However Si is extremly sensitive to oyxgen and the oxidation process of Si

$$\mathrm{Si} + x\mathrm{O} \Longrightarrow \mathrm{SiO}_x \tag{5.1}$$

can not be evaded if the substrate surface is exposed to the ambient atmosphere. This is however inevitable when loading the substrate into the MBE system.

A common preparation technique is wet chemical cleaning prior to the insertion into the MBE system in order to remove the native oxide layer and passivate the surface so as to impede the oxidation reaction. Oxide removal is commonly carried out using fluoric species like hydrofluoric acid (HF) or ammonium fluoride (NH_4F). These species have the inherent advantage that they passivate the Si surface by creating a surface termiated by Si–H bonds, therefore prohibiting the reaction of Si with oxygen. If further impurities are expected to reside on the surface or to have intermixed with the first layers of the Si substrate, it is possible to intentionally oxidize the Si surface by reaction with hydrogen peroxide and to repeat the fluoric treatment, thus "eradicating" the topmost atomic layers of the Si wafer. This technique may also improve the substrate surface morphology by reducing surface steps. The thus prepared substrate is introduced in the MBE system's load chamber. The chamber is evacuated to approx. 10^{-7} torr, then the substrate is heated to approx. 300°C for 30 minutes to remove organic adatoms from the surface. At this temperature the Si–H bonds are broken, leaving a clean Si surface that may be used for MBE growth.

Another possibility of substrate preparation, that is often used in addition to the afore mentioned *ex situ* chemical cleaning, consists in "flashing" the substrate surface *in situ* with a metallic species that is subsequently evaporated [33]. The metallic species needs to be at liquid stage and highly reactive with oxygen, so that the Si–O bonds on the oxidated surface can be broken. In the case of III-nitride MBE, Ga is the material of choice.

All samples used in the work presented in this thesis have been prepared exclusively by *in situ* "Ga-flashing". The following sequence was used:

The substrate is loaded into the MBE growth chamber and heated to a moderate temperature (approx. 500°C). At that temperature, a thin layer (several nm) of metallic Ga are deposited on the surface. Due to the high reactivity with oxygen, Ga oxide (GaO_x) will be formed. Subsequently the substrate is heated up to a temperature above the Ga desorption point (approx. 680°C). The Ga(oxide) will desorb, thus leaving a clean Si(111) surface:

$$SiO_x + Ga \Longrightarrow Si + GaO_x \text{ (des)} \tag{5.2}$$

The surface condition of the Si substrate can be investigated *in situ* by RHEED. The Si(111) surface has a characteristic (7×7) reconstruction, that it adopts at thermodynamic equilibrium. This reconstruction can be probed by RHEED and leads to a very characteristic (7×7) diffraction pattern.

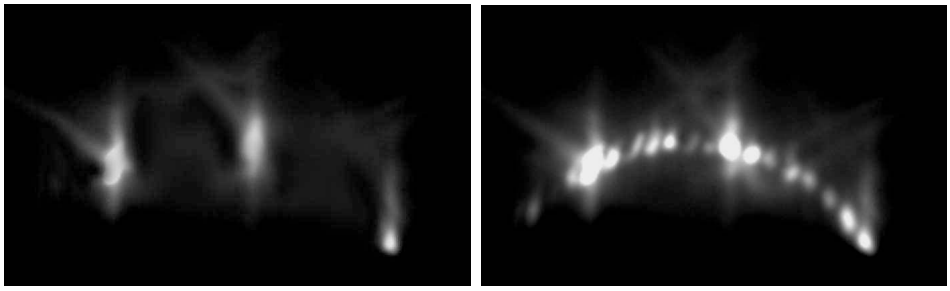

(a) **(b)**

Figure 5.1 – RHEED reflection patterns on a Si(111) surface: (a) 1×1 pattern of a surface with a thin oxide layer, (b) characteristic 7×7 pattern testifying for an atomically clean, reconstructed Si surface: 6 additional spots have appeared between the main 1×1 spots.

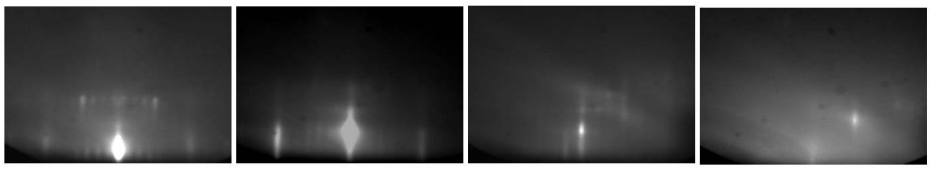

Figure 5.2 – Evolution of the RHEED pattern along the $[1\bar{1}0]$ azimuth of the Si(111) surface at t = 0, 15, 30 and 45 s (from left to right). At $t = 0$, a bright 7×7 reconstruction of the Si surface is observed. Then, atomic nitrogen is supplied to the surface. The 7×7 reconstruction vanishes and at t = 45 s, even the main 1×1 features disappear, testifying for the complete coverage of the surface by amorphous Si_xN_y.

However, as RHEED is very surface sensitive, the presence of 0.3 ML of $Si0_x$ will lead to a loss of the characteristic diffraction pattern. Therefore, the observation of the (7×7) reconstruction by RHEED is a very accurate proof of an atomically clean Si surface. Figure 5.1 shows typical RHEED patterns of a Si surface, (a) before the oxide removal, (b) the characteristic pattern on an atomically clean surface.

5.1.2 Surface nitridation

One of the main issues of nitride growth on Si and especially Si(111) is the high reactivity of the Si surface to the impinging nitrogen atoms. Silicon reacts with nitrogen to form Si nitride. The nature of the obtained Si nitride depends on the growth conditions. Under stoichiometric conditions and at a high temperature (over 1000°C), crystalline Si nitride will be formed:

$$3\,\mathrm{Si} + 4\,\mathrm{N} \Longrightarrow \mathrm{Si_3N_4} \tag{5.3}$$

In the case of III-Nitride-MBE, nitrogen is provided by a high-energy plasma (unintentionally creating a certain amount of nitrogen ions) and nitrogen atoms imping on the Si surface at relatively low temperature. Under these conditions the resulting Si nitride will be amorphous:

$$x\,\mathrm{Si} + y\,\mathrm{N} \Longrightarrow \mathrm{Si}_x\mathrm{N}_y(\mathrm{a}) \tag{5.4}$$

For the growth of nitride NWs, high substrate temperatures are needed in order to obtain a high adatom diffusion on the substrate surface. However, high substrate temperatures lead to a strong adatom desorption and thus to a low probability of GaN nucleation. Therefore the nucleation phase for nitride NWs is relatively long (several minutes). The reaction between Si and nitrogen on the other hand is of higher velocity and a continuous $\mathrm{Si}_x\mathrm{N}_y$ layer is formed in less than a minute growth time. Therefore the formation of amorphous $\mathrm{Si}_x\mathrm{N}_y$ is inevitable during growth of catalyst-free GaN NWs on Si(111).

Due to the low diffusion of nitrogen atoms through the $\mathrm{Si}_x\mathrm{N}_y$ layer, the nitridation process is self-limiting to a nominal layer thickness of about 5 nm [cf. fig. 5.8(b)].

Typical experimental conditions for the nitridation of the Si surface were chosen als follows:

- substrate temperature T_{sub} = 780 °C
- nitrogen plasma power P = 500 W
- nitrogen flux Φ_{N2} = 2 sccm
- nitridation time = 5 min

The kinetics of the nitridation process have been observed by RHEED. Figure 5.2 shows a series of 4 RHEED patterns taken at 0, 15, 30 and 45 seconds of surface nitridation, respectively. On fig. 5.2(a) a bright (7×7) Si surface reconstruction can be observed, testifying for a atomically clean Si surface, especially free of any Si oxide. At $t = 0$, the nitrogen plasma beam is directed to the Si surface. As nitridation proceeds (fig. 5.2 (b) to (d)), the (7×7) reconstruction disappears, the RHEED intensity decreases substantially and finally also the (1×1) main Si reflexes disappear, due to the formation of a continuous $\mathrm{Si}_x\mathrm{N}_y$ layer of several nm in thickness.

As shown by RHEED, the top monolayers of the Si surface are completely nitridated in less than a minute. Therefore a total nitridation time of 5

minutes was chosen in order to reach the "self-limited thickness" [1] of about 5 nm.

5.1.3 GaN NW growth

After completing the nitridation process, the Si wafer is covered by an amorphous Si_xN_y layer of several nanometers thickness. Growth of GaN NWs will be carried out on top of this interlayer. The growth is carried out under nitrogen-rich conditions, necessary for the growth of catalyst-free NWs [2], i.e. with an excess of the group V material (nitrogen) or, in other words, a high V/III-ratio.

The V/III ratio is in fact the most critical parameter for the growth of catalyst-free NWs [34]. It is calculated by establishing the ratio between the *effective* growth rates of the group V and group III material. In order to determine growth rates, it is important to evaluate the material deposited on the substrate. This is, however, very difficult in the case of NWs, as they do not cover the entire substrate. Therefore, growth rates have to be determined via the growth of 2D layers:

In order to measure the Ga-rate, is is important to make sure that no Ga is desorbed from the substrate surface. Therefore, growth is carried out at low substrate temperature (approx. 600°C). Growth is carried out under nitrogen-rich conditions, so that the growth rate will be limited by Ga. The layer is grown for one hour and the layer thickness is determined *ex situ* by cross-section scanning electron microscopy (SEM). By establishing the ratio of thickness over growth time, the Ga growth rate is assessed.

In order to measure the N-rate, the conditions must be choses so as to make sure, that the layer is grown under an excess of Ga, so that the limiting factor of the growth rate will be the supply of active nitrogen. Growth is carried out at high temperature (approx. 730°C) under Ga-rich conditions and the growth rate is determined as described above.

The growth of GaN NWs is then carried out with a high *nominal* V/III ratio, i.e. the ratio of material impinging at the substrate surface. However, growth of GaN NWs is carried out at very high temperature (750-800°C), therefore desorption at the substrate surface plays an important role. The desorption rates for metallic species (i.e. Ga) are higher than for nonmetal species. Therefore the conditions on the substrate surface, i.e. at the growth front, will be slightly more nitrogen-rich and the *effective* V/III ratio will be

[1] We have carried out the nitridation process with exposure times varying from 5 minutes to 1 hour. The thickness of the amorphous Si nitride layer measured by HRTEM was roughly 5 nm in all cases

higher that the nominal value. However, due to the issues mentioned above, the exact effective V/III ratio cannot be assessed in our MBE, therefore nominal values will be given.

Typical experimental conditions for the growth of GaN NWs on Si(111) were:

- substrate temperature T_{sub} = 780 °C
- nitrogen plasma power P = 500 W
- nitrogen flux = 2.80 Å s
- Ga flux = 0.45 Å s
- V/III ratio = 6.2

5.1.4 GaN nucleation

The early stages of the GaN NW growth process, namely the nucleation period, has been investigated by a combination of *in situ* RHEED and *ex situ* HRTEM. During growth, one RHEED pattern was recorded every 12 seconds: the RHEED intensity was determined by monitoring in situ the diffraction intensity in a fixed rectangular area at a given position that involves several GaN 3D spots, as depicted by the dashed white rectangle in the inset of fig. 5.4. The evolution of the GaN spot intensity was then assessed by integrating and summing the overall area over each GaN 3D spot: it should be noted that the background intensity between each GaN 3D spot corresponding to the diffusive contribution was not taken into account. In order to combine the RHEED measurements with a microstructural analysis, cross-sectional TEM specimens were prepared from dedicated samples grown at different durations of 7, 11, 16 and 24 min, including the incubation time. The incubation time corresponds to the initial period once both the Ga and nitrogen shutters are open during which no RHEED signal is detected: its meaning is discussed later.

The evolution of the RHEED intensity is presented in Fig.5.4 and reveals in correlation with the HRTEM images that the nucleation process consists of four consecutive different stages. Typically, the RHEED intensity is initially close to zero, then increases and eventually saturates.

Prior to GaN NW growth, the (7×7) surface reconstruction of the Si(111) substrate is observed and rapidly vanishes once the nitridation process begins by only opening the nitrogen shutter. The stage (I) of the nucleation phase starts with the subsequent opening of the Ga shutter (i.e. at t = 0 min).

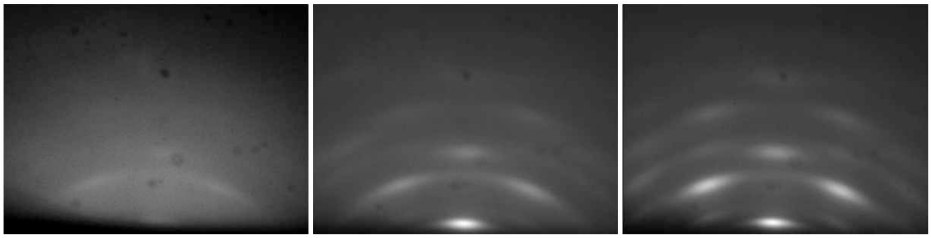

Figure 5.3 – Evolution of the RHEED pattern along the $[1\bar{1}0]$ azimuth during GaN nucleation on Si_xN_y.

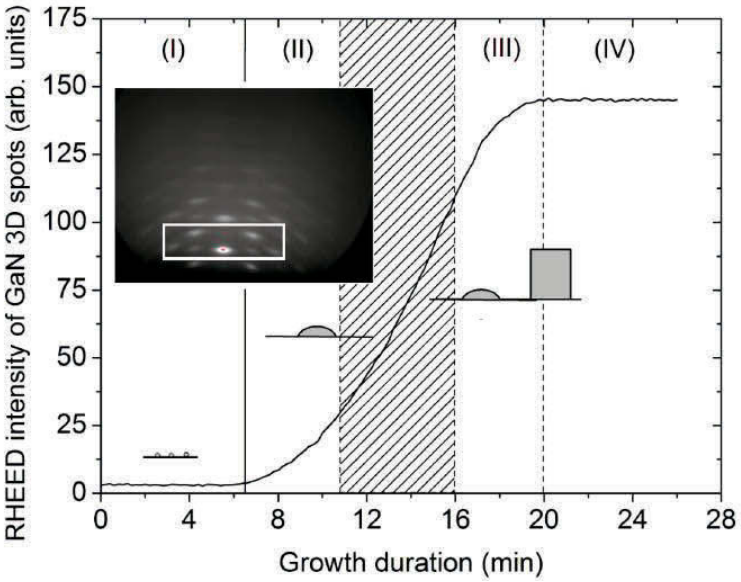

Figure 5.4 – Evolution of the RHEED intensity as growth proceeds. Four distinct consecutive regions are distinguished within such an analysis. The first insets represent simple sketches of GaN island shape, as observed by HRTEM images in fig. 5.5 recorded on dedicated samples. The dashed zone points out that the first spherical cap undergoing a shape transition towards the NW morphology takes place between a growth duration of 11 and 16 min according to HRTEM imaging. The second inset represents a typical RHEED pattern of the GaN NWs (40 min). The rectangular area depicted by dashed white lines yields the RHEED intensity from the GaN 3D spots. The roman numbers (I) to (IV) refer to the stages of the nucleation process as described in section 5.1.4

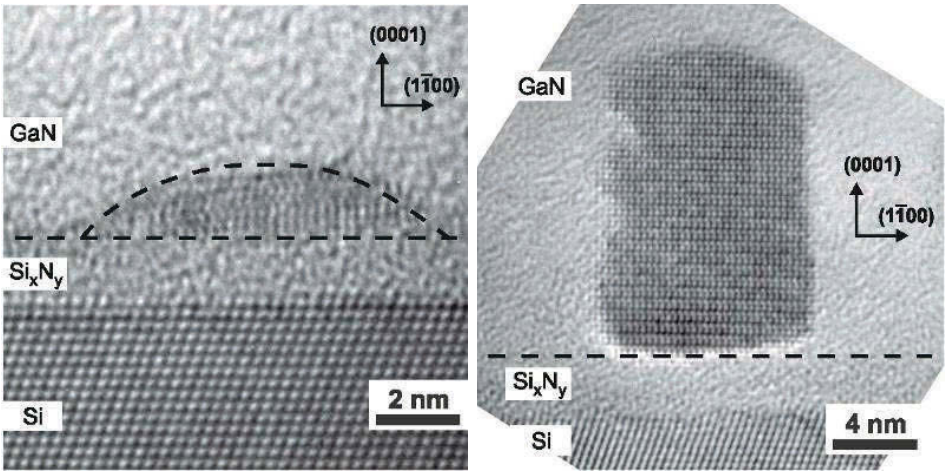

(a) **(b)**

Figure 5.5 – HRTEM images collected along the [11$\bar{2}$0] direction on dedicated samples grown for 7 and 16 min, revealing the following respective GaN island shapes at the onset of the nucleation process: (a) spherical cap-shaped island and (b) NW. The NWs are hexahedral. The shape of spherical caps is outlined for the sake of clarity.

In this stage, no RHEED signal is detected, revealing the occurrence of an incubation period. A delay in the nucleation process owing to a massive Ga desorption at the high growth temperature of 780 °C could be involved during this period as mentioned in Ref. [35]. In particular, it has recently been reported from quadrupole mass spectrometry measurements that the Ga desorbing rate is fairly high in the very early stages of the self-induced growth of GaN NWs on a Si_xN_y amorphous interlayer [36]. Furthermore, since Ga adatoms adsorb and diffuse onto the surface, metastable 2D GaN nuclei are also expected to form during this period.

The start of stage (II) takes place after an incubation time of 6.5 min and is marked by the occurrence of the first GaN spots along rings on the RHEED patterns as shown on fig. 5.3. This stage is associated with the formation of the first stable 3D GaN nuclei. A typical HRTEM image of a GaN nucleus is shown in Fig. 5.5(a): spherical cap-shaped islands are nucleated on a continuous amorphous Si_xN_y interlayer with a thickness of 2 nm. Most likely, the preferential nucleation sites are surface defects like steps of the amorphous interlayer. The caps are further strongly spherical: their free surface is composed of high index atomic planes, which can be interpolated here by a curved surface. It is worth noticing that GaN thus nucleates, under strongly nitrogen-rich conditions and at high temperature, as spherical-caps

for the self-induced growth both on the AlN buffer layer and on the Si_xN_y amorphous interlayer (as discussed in chapter 6). Throughout the stage (II), the spherical caps coarsen and their density increases, accounting for the rise of the RHEED intensity.

The start of stage (III) corresponds to the formation of the very first GaN NWs after a nucleation time of roughly 16 min and is deduced from HRTEM images collected on dedicated samples. A sample HRTEM image is presented in fig. 5.5(b) and shows the presence of GaN NWs during this stage: NW-shaped islands having a $\{0001\}$ top facet and vertical sidewalls consistent with the presence of $\{1\bar{1}00\}$ planes (i.e. m-planes) are observed. The GaN NWs are expected to be Ga-polar as reported in Ref. [37]. GaN islands thus undergo a shape transition from spherical caps to NWs during the stage (III). It should be noted here that no pyramid-shaped islands are detected in contrast to the self-induced growth on the AlN buffer layer (cf. chapter 6) showing that faceting does not proceed. This remarkable difference in the nucleation process is attributed to the distinct features of the strain: on the AlN buffer layer, the shape transition towards pyramid-shaped islands enable the elastic relaxation of the epitaxial strain in the initial spherical caps. In comparison, on the amorphous Si_xN_y interlayer, the epitaxial constraint is much weaker and the epitaxial strain is therefore very low.

Eventually, the stage (IV) starts with the changelessness of the RHEED intensity after a growth time of 20 min: this changelessness could be attributed to the saturation of the overall spherical cap and NW density. It should be noted that the presence of spherical caps is still detected in this stage, suggesting that the shape transition between spherical caps and NWs statistically takes place at different growth durations. It is expected that the NW density continuously increases with respect to the spherical cap density for longer growth durations.

5.1.5 Direct evidence of the shape transition

The height h and radius r_0 of spherical caps and NWs are systematically determined from HRTEM images recorded on dedicated samples in the stages (II), (III) and (IV), as shown in fig. 5.6. There exist two separate ranges of specific sizes for spherical caps and NWs. The spherical caps have a typical radius and height systematically smaller than 5 and 2 nm, respectively. Their wetting angle θ further equals $42 \pm 7^\circ$ in the entire range of their sizes and hence is smaller than 90° , as shown by the straight lines in fig. 5.6 delineating the experimental data points: this indicates that GaN wets the amorphous Si_xN_y interlayer and that the spherical caps coarsen with a given wetting angle, namely by retaining their shape. The shape transition from

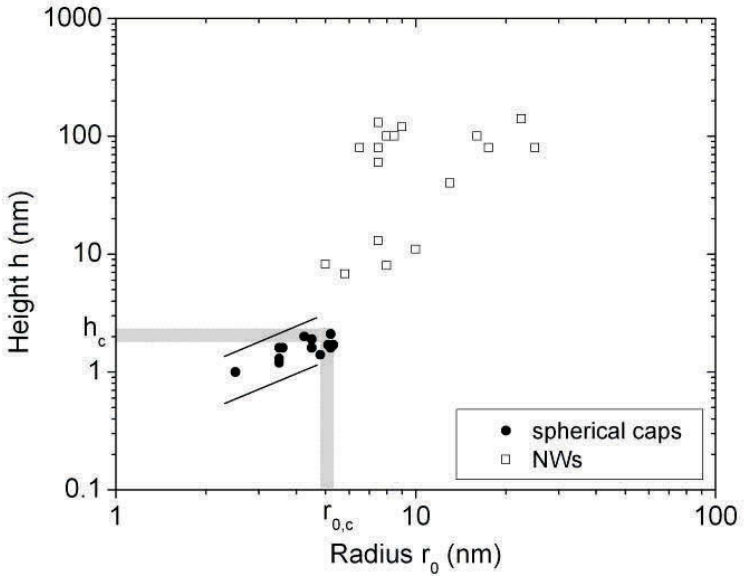

Figure 5.6 – Height h as a function of radius r_0 obtained from HRTEM images for the two different shapes of GaN islands as growth proceeds: the spherical caps and NWs are observed on dedicated samples grown for 7, 11, 16, 24 min and 16, 24 min, respectively. The grey color regions correspond to the experimental critical height and radius of NWs.

spherical caps toward the NW morphology is therefore discontinuous and of 1st order type. The formation of the very first GaN NWs abruptly occurs at an experimental critical radius of 5 nm, which is liable to be highly dependent upon the growth conditions as discussed later. From geometrical considerations, a critical height of about 2 nm is also determined.

Thus a shape transition from cap-shaped islands to NWs has been demonstrated by a combination of *in situ* RHEED and *ex situ* HRTEM.

The contributions to this shape transition of the strain energy, the surface energy anisotropy and the edge energy have been calculated by Vincent Consonni and been endorsed by FEM simulations by Michael Hanke. Those results can be found in

V. Consonni, M. Hanke, **M. Knelangen**, L. Geelhaar, A. Trampert and H. Riechert, *Nucleation mechanisms of self-induced GaN nanowires grown on an amorphous interlayer*, Phys. Rev. B **83**, 035310 (2010).

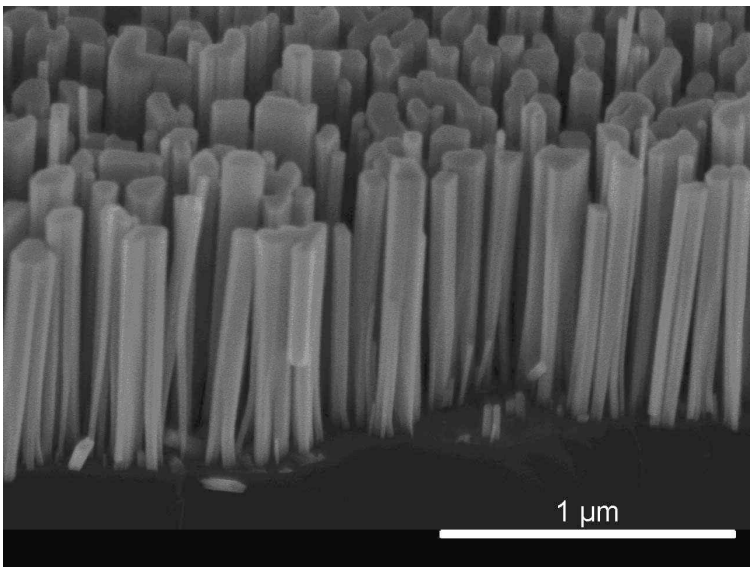

Figure 5.7 – GaN NWs grown by catalyst-free MBE. The NWs are free-standing, about 20-50 nm in diameter and several 100 nm in heigt. Due to the amorphous Si_xN_y interlayer, some NWs are slightly tilted. As the NW densitiy is quite high, coalescence may occasionally occur.

5.2 Structural and morphological characterization

The as-grown NWs were investigated by SEM, HRTEM and Photoluminescence in order to assess the morphological, structural and optical properties of the material.

5.2.1 Morphology

Catalyst-free grown GaN NWs are free-standing NWs with high aspect ratio and a high surface density. Typical characteristics of catalyst-free grown NWs on Si (111) are (cf. fig. 5.7):

- diameter: 20-50 nm
- height: several hundred nm
- density: approx. 10^{14} cm^{-2}
- growth along the [0001] direction
- vertical $\{11\bar{2}0\}$ side facets and a flat $\{0001\}$ top facet.

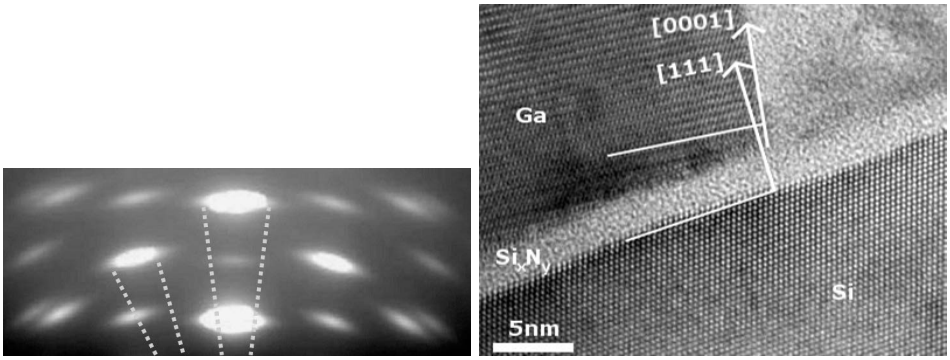

(a) **(b)**

Figure 5.8 – NW tilt induced by the amorphous Si_xN_y interlayer: (a) RHEED pattern of the $[11\bar{2}0]$ azimuth. The RHEED transmission spots are circularly broadended indicating a tilt of the NWs. (b) HRTEM image of a GaN NW on Si_xN_y. The tilt between the [111] direction of the substrate and the [0001] direction of GaN is clearly visible.

Due to the amorphous Si_xN_y interlayer, the epitaxial alignment between the Si substrate and the NWs is not conserved. The NWs therefore nucleate without a unique crystalline orientation as discussed in section 5.1.3. Due to growth kinetics, the NW grow along their *c*-axis and normal to the substrate, so vertical NWs are obtained, as seen in fig. 5.7. However the wires are twisted and tilted with respect to one another. These two aspects have been analyzed by combining *in situ* RHEED and *ex situ* HRTEM investigation.

Nanowire tilt

The nitridation of the Si surface leads to the formation of a continuous amorphous Si_xN_y layer of 3-5 nm in thickness as well as to a roughening of the surface. So GaN NWs grow without epitaxial alignment to the underlying Si substrate. Due to surface roughness, the wires will nucleate with a slight tilt to the substrate normal. The amplitude of this misalignment is of approx. 0° to 7° as observed by SEM and TEM investigation. *In situ* RHEED investigation during nucleation and growth of the NWs shows a circular broadening of the 3D GaN transmission spots (cf. fig. 5.8(a)), testifying for a broad "tilt range", as all deviations from 0° to 7° are present.

Figure 5.8b shows a HRTEM image of the bottom region of a GaN NW taken along the $[11\bar{2}0]$ direction. The amorphous Si_xN_y interlayer can clearly be seen. The angular misorientation between the Si substrate's [111] normal and the GaN lattice's [0001] growth direction is indicated by arrows and

amounts to approx. 7°. As the NW densitiy is relatively high, the misalingnment of the growth direction and the substrate normal may lead to NW coalescence. This will be discussed in section 5.3.

In-plane orientation of GaN NWs

The lack of epitaxial alignment between substrate and NW not only leads to a lack of vertical alignment (tilt) but introduces also a loss of in-plane orientation of the NWs. In the case of epitaxially grown GaN NWs on Si(111) there is an epitaxial alignment of the hexagonal GaN lattice with the pseudo-hexagonal Si(111) surface: GaN[0001] ∥ Si[111] and GaN[11$\bar{2}$0] ∥ Si[110]. However, as the formation of the amorphous Si_xN_y interlayer occurs before the beginning of the GaN nucleation, in-plane orientation of the NWs can be lost.

Figure 5.9a shows a RHEED pattern of GaN NWs grown for 60 minutes taken along the Si [110] direction. The pattern reveals circularly broadened 3D spots, characteristical for vertically misoriented (tilted) NWs. However, the pattern exhibits spots originating from two different crystalline orientations, namely GaN [11$\bar{2}$0] and GaN [1$\bar{1}$00], i.e. there are crystal parts oriented with the [11$\bar{2}$0] direction parallel to the incident beam (along Si [110]) and there are crystal parts with the [1$\bar{1}$00] direction parallel to the incident beam. However, as the incident RHEED beam has a very small angle (3°) with the substrate surface, only crystal parts with either of those two directions fulfill Bragg conditions and lead to constructive diffraction interference. All crystals oriented in a different way will lead to diffuse scattering of the incident beam. Therefore, although only two characteristic RHEED patterns are observed, a combination of all in-plane orientations may be present (see schematic illustration in fig. 5.9b).

This asumption is enforced by the fact, that the RHEED pattern is invariant to substrate rotation, that is: for an arbitrary direction, we will always observe a RHEED pattern originating from crystallites oriented along the [1$\bar{1}$00] and the [11$\bar{2}$0] direction, these being the two only direction leading to constructive interference. Therfore we have an effective statistical distribution of in-plane orientations of the grown GaN NWs, due to the loss of epitaxial alignment by the amorphous Si_xN_y interlayer.

Influence of the MBE nitrogen plasma source

During the experimental work leading to this PhD thesis, two different nitrogen plasma cells were used for the growth of GaN NWs: an SVT Model and more recently, an Oxford Plasma Cell. Although there was little to

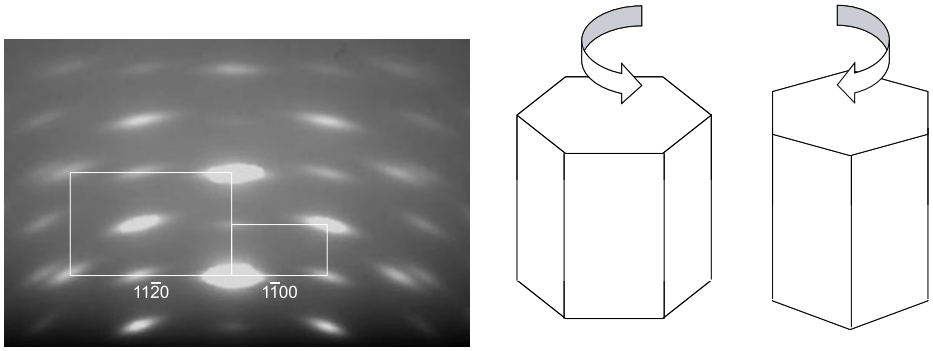

Figure 5.9 – Loss of in-plane orientation induced by the amorphous Si_xN_y interlayer: (a) RHEED pattern showing superimposed patterns corresponding to the $[11\bar{2}0]$ and the $[1\bar{1}00]$ azimuth. Observation of both azimuths indicates a random in-plane orientation of the NWs, as schematically shown in (b).

no influence on the NW growth process, two striking differences are obtained with the two sources:

Material properties The material properties, namely the optical properties were significantly better for material grown with the OXFORD cell. Therefore, for optical experiments, only "OXFORD"-NWs were used.

In-plane orientation The in-plane orientation is almost entirely conserved when working with the OXFORD cell, as will be discussed below.

When using the OXFORD plasma cell for the growth of GaN NWs, the NW in-plane alignment is changed drastically. Figure 5.10a shows a TEM top-view micrograph of GaN NWs. The hexagonal NW shape is clearly visible. In the central part of the image, several NW clusters of approx. 3-5 NWs are visible, illustrating the tilt-induced NW coalecence process. Interestingly, all NWs present well-defined side facets, that are all oriented along the same direction, thus displaying a very high in-plane ordering. This is a suprising result, as prior to growth, the Si surface was exposed to atomic nitrogen for several minutes, resulting in the formation of a continuous SiN layer, as evidenced by a completely diffuse RHEED pattern.

In order to further investigate the in-plane orientation, the sample was probed by x-ray diffraction along the GaN $[10\bar{1}4]$ direction. The resulting pole figue is shown in fig. 5.10b. Interestingly, there exists only a single in-plane orientation for the GaN NWs, i.e. the wires are fully oriented in the

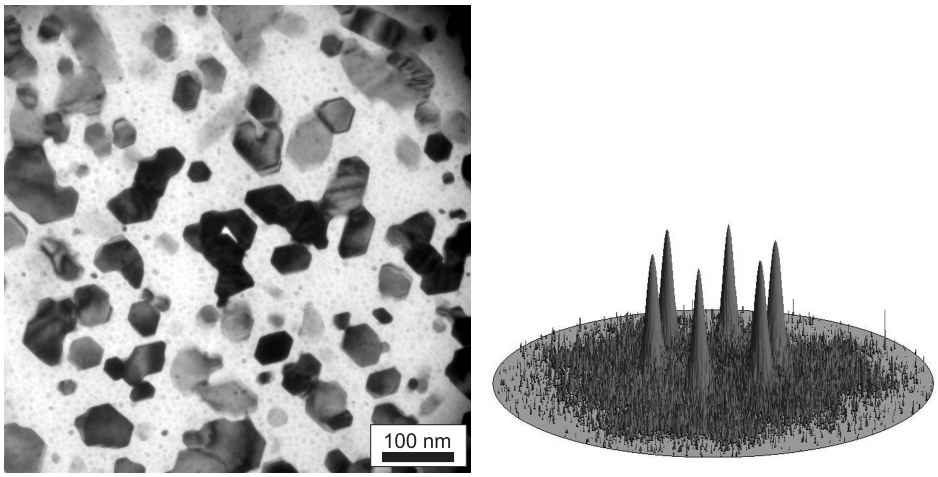

(a) **(b)**

Figure 5.10 – (a) Top-view TEM micrograph of GaN NWs grown on Si(111). NW coalescence occured do to NW tilt. Despite the presence of an amorphous Si_xN_y interlayer, the wires exhibit parallel facets (for a cross-section micrograph, see fig. 5.11. (b) XRD pole figure taken along the GaN $[10\bar{1}4]$ direction. The GaN NWs show a very homogeneous in-plane orientation, although no epitaxial alignment with the Si buffer was possible.

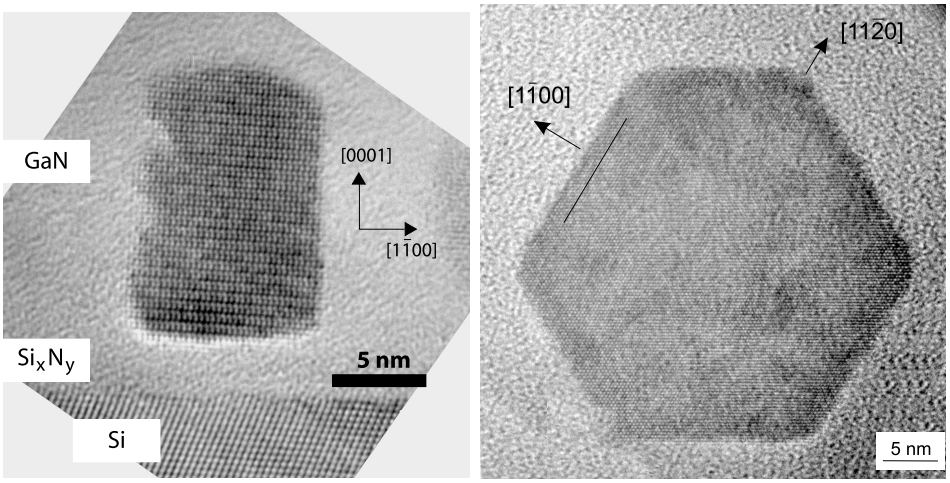

Figure 5.11 – HRTEM images of a single GaN NW grown on Si(111): (a) cross-section view, showing vertical side facets as well as the amorphous Si_xN_y interlayer, (b) plan-view showing the hexagonal base of the NW, showing that the sidewalls of the wire are $\{1\bar{1}00\}$ facets.

plane despite the presence of an amorphous layer of more than 3 nm between substrate and NWs.

To further investigate this issue, a detailed study of the SiN layer should be carried out. As optical characterization of GaN grown with the two plasma sources shows, the material quality obtained with the OXFORD cell is significantly higher, thus suggesting a lesser ion content in the nitrogen plasma. Therefore the Si nitride "grown" with the OXFORD cell could present a higher crystalline part, thus offering some long distance order, which would result in the observed epitaxial alignment between substrate and GaN NWs.

The investigation of this issue has not been carried any further. All samples for this work were grown with the "better" OXFORD cell.

5.2.2 Structural properties

Catalyst-free NWs grown on Si(111) crystallze in the wurtzite structure as described in section 2. As NWs are free-standing nanostructures, it is possible to obtain strain-free NWs that are free of extended defects.

Figure 5.11 shows two HRTEM images of single GaN NWs grown on Si (111). Fig. (a) is a cross-sectional micrograph of a small GaN NW with approx. 10 nm in diameter and 15 nm in height. Between the NW and the Si substrate the amorphous Si_xN_y interlayer is clearly visible. This amorphous

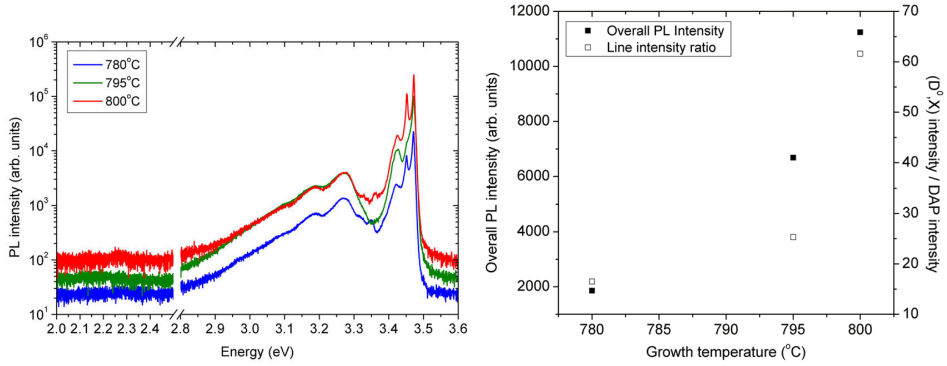

(a) **(b)**

Figure 5.12 – Evolution of the photoluminescence of GaN NWs as a function of growth temperature: (a) PL spectra of GaN NWs grown at different substrate temperatures. (b) Relative intensity of the donor-bound exciton (D°, X) as compared to the donor-acceptor-pair band (DAP).

layer covers the complete Si surface and is of approx. 3-5 nm in height, due to the self-limiting character of the Si nitridation process. The photograph was taken along the $[1\bar{1}0]$ direction of the Si substrate which conincides with the $[11\bar{2}0]$ direction in the GaN lattice.

The HRTEM image reveals that the NW has vertical $\{1\bar{1}00\}$ side facets and a flat (0001) top facet (due to the very small dimensions of this wire, the top facet is not entirely flat). The GaN lattice was grown in wurtzite structure and free of any extended defects.

Figure 5.11b shows a plan-view (i.e. taken along the [0001] direction) HRTEM image of a single GaN NW, taken at some distance to the substrate surface. The micrograph clearly reveals the hexagonal base of GaN NWs with regular side facets and sharp corners. The a- and m-planes of the GaN crystal can be clearly identified by their inter-plane distance d of 1.59Åand 2,76Å, respectively. Thus this micrograph reveals that the NW side facets are oriented along the $[1\bar{1}00]$ direction. The "corners" delimiting the side facets are very small, which is in disagreement with the theory that NW growth could be enabled by very small $\{11\bar{2}0\}$ facets that would enhance the diffusion of Ga adatoms towards the NW top [38].

5.2.3 Optical properties

Catalyst-free grown GaN NWs present many features that make them the building blocks of choice for optoelectronic components. The optical properties are however depending on the crystal structure, namely on the presence

of defects. An adequate technique to investigate the optical properties of NWs is to carry out luminescence experiments, namely photoluminescence (PL).

In the PL setup, an optical active material is excited by photons originating from a laser source. The impinging photon will promote and electron from the valence band to the conduction band, thus creating a hole in the valence band. The recombination of an electron and hole will lead to the emission of a photon. The wavelength of the photon will be characteristic of the material as well as of the defects present inside the material.

The two main growth parameters are the growth temperature (i. e. the substrate tempearture during growth) and the III/V ratio (ratio betwen the impinging Ga atoms and N atoms). We have thus grown GaN NWs varying those two parameters. The III/V ratio has been found to have little to no influence on the optical properties and are thus not shown here.

PL measurements were carried out at RT on GaN NW samples grown at substrate temperatures of 780°C, 795°C and 800°C (technical limit of the MBE system). The PL spectra are represented in fig. 5.12(a). These spectra show two main features:

- a broad emission "peak" at 3.27 eV, which is attributed to donor-acceptor-pairs (DAP) that are bound to point defects in the material [39].
- a series of three excitonic emissions culminating at 3.47 eV. The emission at 3.47 eV originates from donor-bound excitons (D°, X). This energy of this emission is equal to the bandgap of bulk material and its intensity is highest in a defect-free material [40].

Interestingly, no PL emission is detected at the spectral range from 2.0 to 2.4 eV. In 2D GaN layers, a characteristic emission, so called "yellow luminescence" is found at approx. 2.2 eV. This emission originates from deep energy states caused by defects in the material. The absence of this specific emission accounts for the high crystalline material in the NWs.

In order to characterize the optical quality, two main characteristics will be analyzed: the overall optical intensity (i.e. the "quantity" of light that is emitted by the sample), as well as the ratio between the (D°, X) emission and the unintentional DAP emission.

From fig. 5.12a, it can be observed that the overall optical intensity increases with increasing growth temperature. The overall intensity is lowered only by non-radiative recombination centers, like point defects. Therefore a higher overall intensity accounts for better crystalline quality. High growth temperatures therefore favor high crystalline quality.

In a further step, the relative evolution of the "good" donor-bound exciton band and the "parasitic" DAP band are analyzed. Figure 5.12b shows the evolution of the overall intensity compared to the evolution of the $(D^{\circ}, X)/DAP$ ratio. The relative increase of the donor-bound exciton is stronger that the increase in the DAP band, showing that high growth temperature also reduces the number of radiative defects in the GaN.

Thus, the best optical qualities are likely to be obtained at a growth temperature higher than 800°C.

5.3 NW coalescence: structure and optics

As seen in the previous section, the growth of GaN NWs on Si(111) inevitably leads to the nitridation of the substrate surface and thus to the formation of an amorphous Si_xN_y interlayer. This interlayer prohibits the epitaxial alignment between substrate and NWs, effectively leading to a respective NW tilt and twist. Although the tilt angle is generally only of a few degrees, due to the surface density and high aspect ratio of the NWs, NW tilt leads to NW coalescence. Due to geometrical reasons the coalescence typically happens at several hundred nanometers above the substrate surface.

Figure 5.13 shows a TEM micrograph of GaN NWs grown on Si(111). The NWs have coalesced at about 200 nm distance from the substrate. We systematically observe in all of the studied samples that the tilt between the two misaligned coalesced NWs is accomodated by the formation of a network of boundary dislocations. These are identical dislocations that are distributed along the contact area of the two NWs. The inset of fig. 5.13 shows a Fourier-filtered HRTEM enhancement of the contact point with two dislocations. Only the $\{1\bar{1}00\}$ planes are depicted to strengthen the edge character of the dislocations. Such boundary dislocations can be of pure edge-type with a Burgers vetor of $\vec{a}$ in order to accomodate the tilt component [41]. If besides such a component, a twist component exists between the two coalesced NWs as it is expected in our case, boundary dislocations an be of mixed type with a Burgers vetror of $\vec{a} + \vec{c}$. The number of boundary dislocations involved in the network depends on the local conditions of the coalescence process: more boundary dislocations are likely to be formed with increasing tilt and twist components between the two coalesced NWs (cf. Hall: $d \approx b/\theta$). Local stress is further generated around the network of boundary dislocations, as revealed by bend contours in fig. 5.13, but is accomodated by the lateral NW surfaces.

Further, all studied samples show presence of basal-plane stacking faults (SF) at a mean distance of several hundred nm above the contact point of

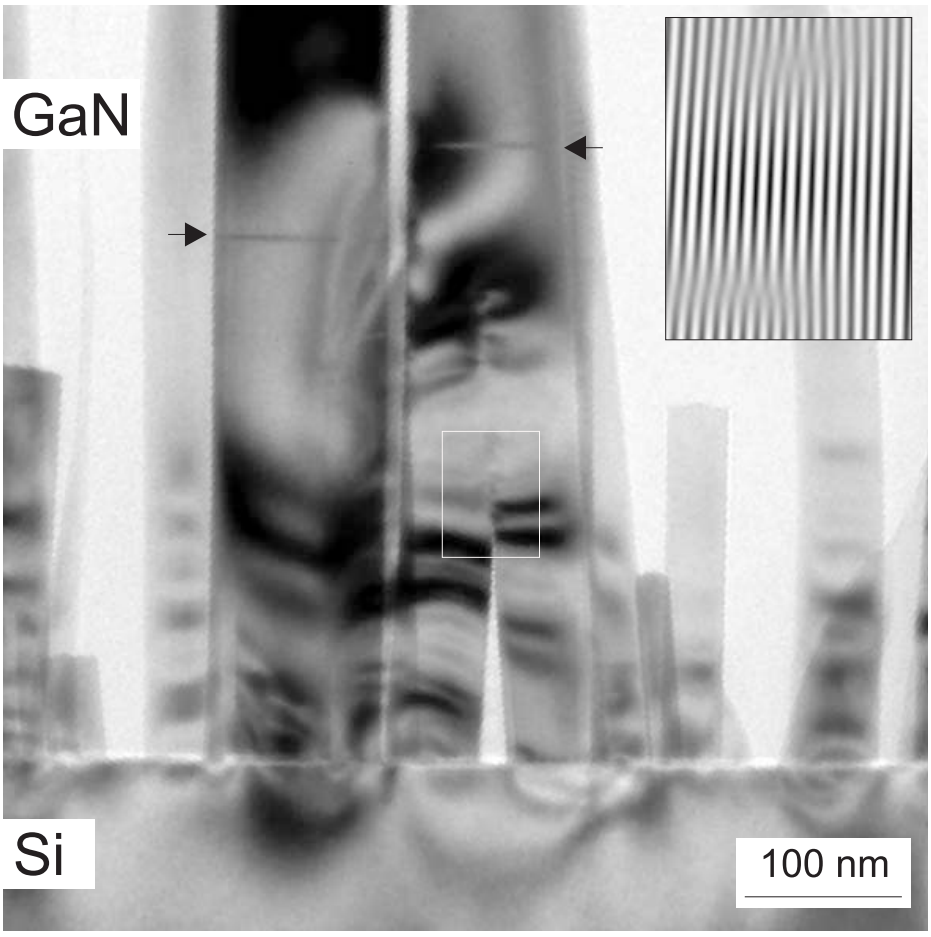

Figure 5.13 – TEM micrograph of two tilted GaN NWs. Due to the respective tilt, the NWs have coalesced at a height of approx. 200 nm. The NW tilt has been accomodated by a network of boundary dislocations above the contact point. The inset shows a Fourier-filtered HRTEM image of the contact point region, highlighting the dislocation network. Several nanometers above the contact point, stacking faults have been formed, indicated by black arrows.

the two coalesced NWs. The SFs are indicated by black arrows on fig. 5.13.

HRTEM analysis has been performed on the central region of coalesced NWs. Fig. 5.14 shows a corresponding HRTEM image. The stacking sequence of the wurtzite GaN lattice is shown to be

$$ABABAB \quad ABCA \quad CACACA\cdots, \tag{5.5}$$

indicating that the SF is of I_1-type. This type of SF is formed during growth but is not generated due to slip and strain relief. The physical origin of its formation has not completely been elucidated yet but its systematic presence at some distance above the dislocation network in coalesced NWs as well as its absence in uncoalesced NWs highlights a clear correlation with the coalescence process.

Above these SFs, the top part of the coalesced NWs is free of any type of extended defects that could be observed by HRTEM, revealing the very high crystalline quality of this NW region.

In order to investigate the effect of the coalescence-induced defects on the optical properties of GaN NWs, single NWs have to be optically probed. However, micro-PL can only probe objects with dimensions > 1 μm, therefore spatially resolved cathodoluminescence has been performed.

Cathodoluminescence (CL) occurs when a high energy electron beam impinges on a direct band-gap semiconductor. The electron beam will promote an electron from the valence band to the conduction band, thus creating a hole in the valence band. The recombination of an electron and a hole will lead to the emission of a photon. The wavelength of the photon will be characteristic of the material as well as of the defects present inside the material. For further information, see ref. [42].

CL spectra of a single free-standing coalesced NW have been recorded at 6 K. Separate spectra have been recorded for the bottom, center and top of the NW, as presented in fig. 5.15. These spectra consist of three types of distinct emission:

- **3.47 eV** Radiative recombinations of bound exitons (D°, X) to Si of oxygen donors give rise to a line at 3.47 eV [6]. In GaN, Si and oxygen act as hydrogenic donors by substituting for Ga and nitrogen sites with very close ionization energies of 30.18 meV and 33.2 meV respectively [43]. The presence of donor bound exitons in unintentoinally doped GaN is an indication of its high crystalline quality.

- **3.42 eV** The nature of the line at 3.42 eV (SF_1) remains controversially discussed in the literature. In the present case, the emission is

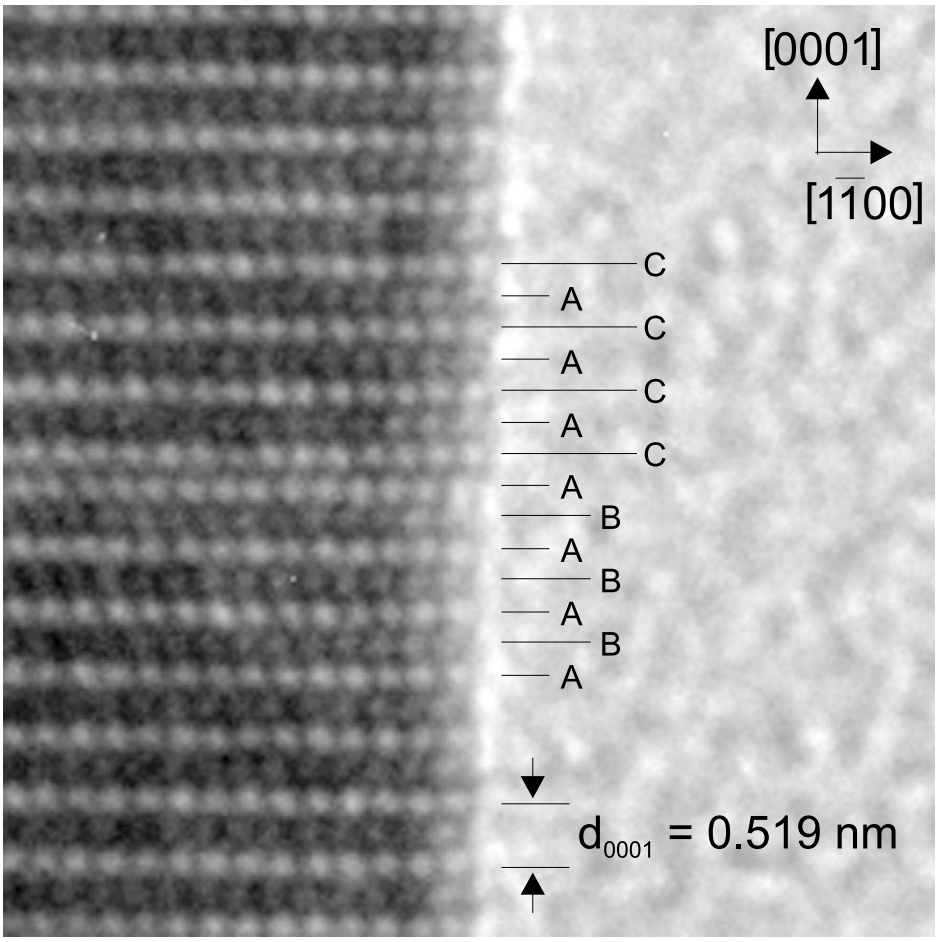

Figure 5.14 – HRTEM image of the central region of a coalesced GaN NW on Si(111). The image clearly reveals the presence of a stacking fault in the wurtzite material. The stacking sequence has been determined, showing that the stacking fault is of type I_1. This type of stacking fault systematically appears in coalesced NWs at some distance above the contact point.

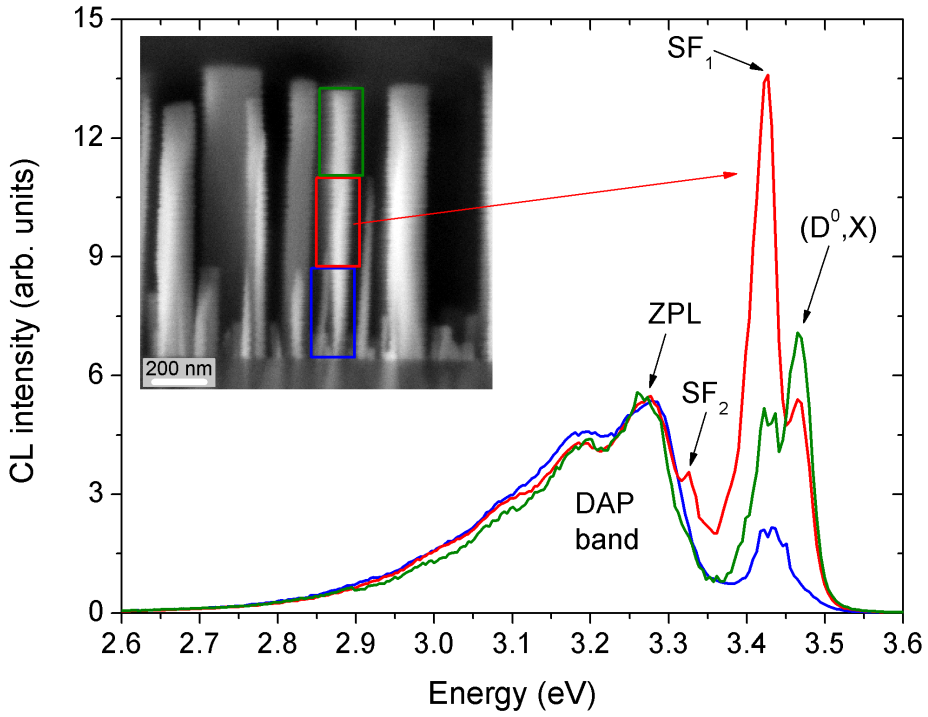

Figure 5.15 – Three CL spectra taken on a single coalesced GaN NW. The inset shows a SEM photograph indicating the analyzed NW region.

associated with radiative recombinations of excitons bound to I_1-type basal-plane SFs, as evidenced below [44, 45].

- **3.28 eV** The third characteristic feature is a donor-acceptor pair (DAP) band, composed of a zero phonon line (ZPL) at 3.28 eV followed by two longitudinal optical phonon repicla (LO) at 3.19 eV and 3.10 eV, each separated by a phonon energy of 91.7 meV [44].

Although each of these three types of emissions appears on all of the three spectra recorded along a single coalesced NW, there are major differences concerning the predominant emissions. Figure 5.16 shows monochromatic CL image of the same single free-standing coalesced NW obtained for varying CL energies (i.e. at 3.28, 3.42 and 3.47 eV) that clearly confirm that the corresponding luminescence originates predominantly from different NW regions.

The intensity of the ZPL corresponding to the DAP band at 3.28 eV remains unchanged along the entire NW in fig. 5.15 and is homogeneously distributed in fig. 5.16b. This is a strong indication that the spatial distribution of donors and acceptors composing the pairs is uniform. However, the excitonic band is much less intense at the bottom of the coalesced NW that at the center and the top and this for both CL lines at 3.42 eV and 3.47 eV. Instead the DAP band dominates the spectrum recorded at the bottom of the coalesced NW, revealing a poor crystalline quality. This can be attributed to the high density of coalescence-induced boundary dislocations in this part of the NW. Boundary dislocations are expected to trap charge carriers or to induce their nonradiative recombination, resulting in a drastic decrease in the density of excitons. This, in turn, leads to the low intensity of the excitonic band.

In contrast, the excitonic band is much more intense in the spectra recorded at the center and top of the coalesced NW, but the nature of the predominant line varies. At the NW center, the line at 3.42 eV clearly dominates the excitonic band as revealed in fig. 5.15 and fig. 5.16c. These observations give strong direct evidence that I_1-type basal-plance SFs, which have been observed by HRTEM in this specific region of the NWs (cf. figs 5.13 and 5.14), contribute to the 3.42 eV line (SF_1)by acting as active radiative recombination centers [45]. In addition there exists a line at 3.33 eV (SF_2), which is possibly related to the presence of prismatic SFs [45].

At the top of the NW, the (D°, X) line at 3.47 eV has the highest intensity, as shown in fig. 5.15. Figure 5.16(d) reveals that this type of excitonic emission is most intense at the top of the NW. These findings are in agreement with the absence of extended defects in HRTEM investigation and confim

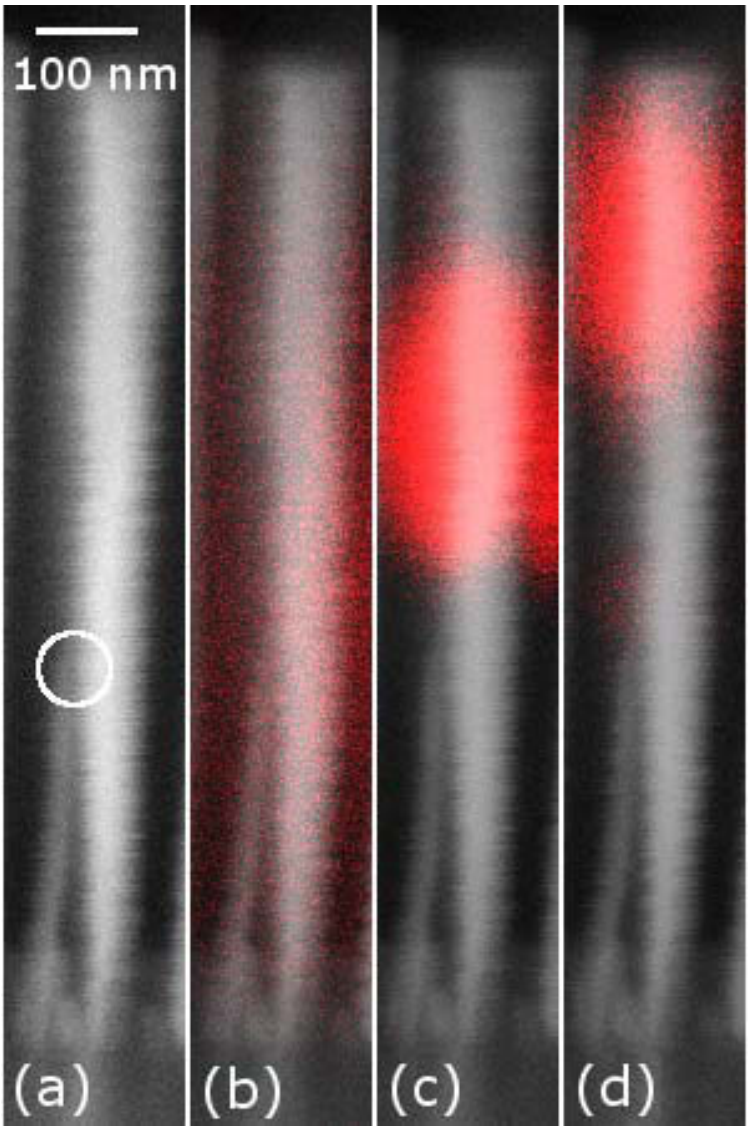

Figure 5.16 – SEM image of a coalesced GaN NW on Si(111) (a). CL of specific wavelengths has been mapped to the SEM image: (b) shows the homogeneous distribution of donor-acceptor pairs over the entire NW, (c) testifies that the the strong emission ata 3.41 eV originates from the NW center, where a high density of I_1-type stacking faults is observed, (d) shows the emission of the donor-bound exciton, testifying that the top of the NW is of very high crystalline quality.

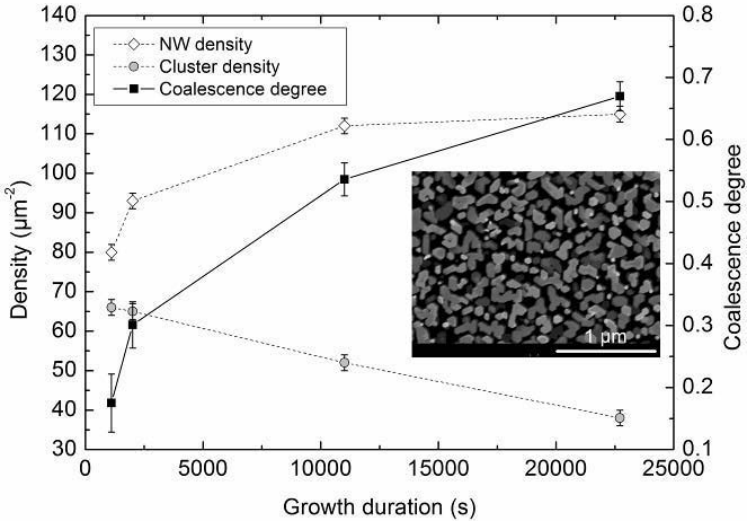

Figure 5.17 – Evolution of NW density, cluster density and coalescence degree as a function of growth time. The inset shows a typcial top-view SEM image.

that, despite coalescence, the crystalline quality at the top of the coalescend NW remains very high.

5.4 Nucleation and coalescence: NW density

In the previous section, we have discussed the occurence of NW coalescence when growing GaN NW on Si. Coalescence has been shown to lead to a high number of structural defects within the nanowires. It is therefore of high interest to reduce the NW coalescence to a minimum. In the following study we discuss the effect of several growth parameters on NW nucleation and coalescence. The parameter used to measure coalescence is the NW and cluster density.

The growth temperature and Ga rate were varied in the range of 770 - 815°C and 0.25 - 0.7 Å/s, respectively. The nitrogen rate was equal to 2.8 Å/s, which leads to a V / III ratio in the range of 4 - 11.2. The total growth time was adjusted such that the effective growth time was systematically 3h: the Ga shutter was closed 3h after the end of the incubation time indicated by the appearance of GaN spots in RHEED. Another series of samples was grown with different effective growth times between 1110 and 22710 s, for a substrate temperature and Ga rate of 780°C and 0.45 Å/s, respectively.

The cluster and NW density was determined from top-view field-emission

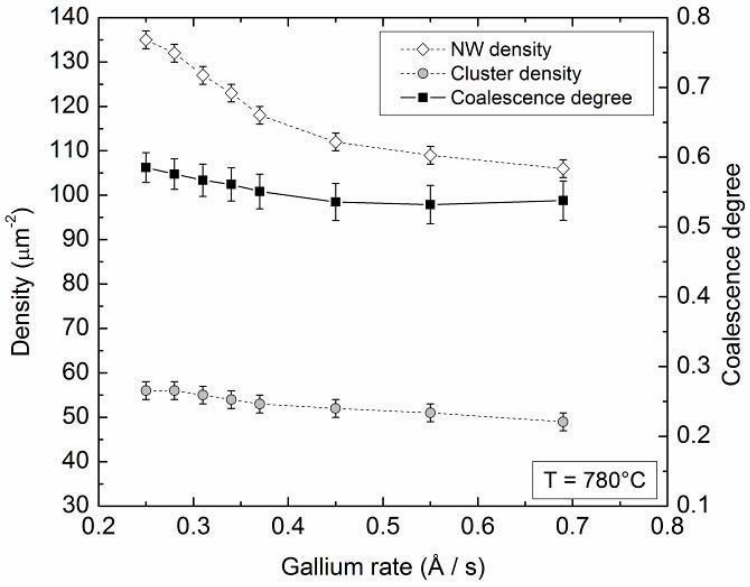

Figure 5.18 – Evolution of NW density, cluster density and coalescence degree as a function of the Ga rate.

scanning electron microscopy (FESEM) images as shown in the inset of fig. 5.17. Edges were detected and particles counted with the software ImageJ to determine the cluster density and the surface area of each cluster: subsequently, the NW density was estimated by dividing the cluster surface area by the NW mean surface area, since every NW has an hexagonal base and a very close diameter for a given growth condition. The procedure has been cross-checked by recognizing the NW shape in each cluster. For each sample, a population of more than 500 NWs was taken into account. In order to quantify the NW coalescence process, the coalescence degree $\alpha_{\text{coalescence}}$ is defined as

$$\alpha_{\text{coalescence}} = 1 - (\rho_{\text{cluster}}/\rho_{\text{NW}}) \tag{5.6}$$

where ρ_{cluster} and ρ_{NW} represent the cluster and NW density, respectively. A free-standing NW is also considered as a single cluster.

The evolution of the NW and cluster density and of the coalescence degree is presented in Figs. 5.17, 5.18 and 5.19 as a function of the growth time, Ga rate, and growth temperature, respectively. By increasing the growth time, the NW density continuously increases and saturates at 115 NWs/μm^2 while the cluster density diminishes. At the same time, the coalescence degree significantly increases due to the small but not negligible radial NW growth, which leads to the coalescence of neighbouring NWs. The maximum numeri-

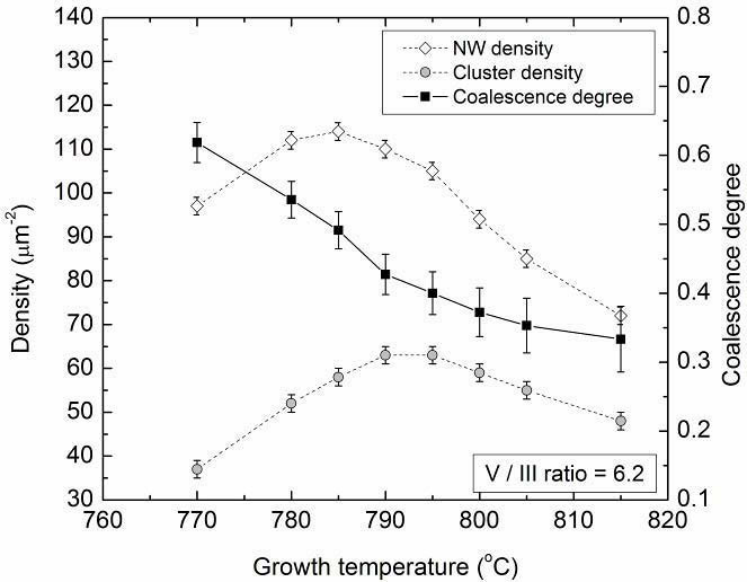

Figure 5.19 – Evolution of NW density, cluster density and coalescence degree as a function of growth temperature.

cal values for the densities are of the same order of magnitude as reported in Refs. [7] and [46]. However, the importance of distinguishing between NWs and clusters is revealed by the comparison between the trends found here in Fig. 5.17 and in Ref. [7]: the decrease in the cluster density seen in Fig. 5.17 corresponds to the decrease in the NW density observed in Ref. [7] after about 1h of growth time, while in contrast the NW density as determined here keeps on increasing.

The effects of the Ga rate (i.e. the V/III ratio) are shown in Fig. 5.18. The NW density continuously decreases with increasing the Ga rate, namely with decreasing the V/III ratio, and eventually reaches a plateau. Both the cluster density and the coalescence degree remain almost constant. Since the NW density comparably decreases strongly, which should reduce the coalescence degree, the observed trends may indicate that the radial NW growth rate increases with increasing the Ga rate. Indeed, it is well known that the growth mode switches from NW growth to planar layer growth for increasing Ga rate [47], which corresponds to an increase in the radial growth rate and a strengthening of the NW coalescence process. The higher radial growth rate at higher Ga rate has recently been deliberately used to perform a completely two-dimensional layer at the NW top [48].

More importantly is the growth temperature dependence depicted in Fig. 5.19. The evolution of the NW density follows two consecutive steps: (i) the

NW density initially increases to 114 NWs/μm^2 at about 785°C; (ii) subsequently, the NW density decreases for higher growth temperatures. The occurrence of a maximum NW density for intermediate growth temperatures is of high interest for technological applications in which increasing the NW density represents a critical point. The trend for the cluster density also exhibits a maximum, although it occurs at a slightly higher growth temperature. In contrast, the coalescence degree is strongly reduced in a monotonous way. It is remarkable that the coalescence degree decreases between 770 and 785°C while the NW density increases: this may suggest that the radial NW growth rate decreases as the growth temperature is raised. The thermal decomposition and Ga desorption are significant in such a temperature range: it is deduced from Fig. 5.19 that the associated decrease in the growth rate is stronger on the m-plane NW vertical sidewalls than on the c-plane top facets. For most practical purposes, it is relevant that the NW coalescence process can be inhibited by raising the growth temperature, which is related to a better structural morphology of the NW ensemble.

The evolution of the NW density as measured in this study only depends on the nucleation phenomena, since the coalescence effects was separated by the determination of the cluster density and coalescence degree. According to the standard island nucleation theory, the island density N_I is given by

$$N_I \sim (\phi_{Ga})^2 \exp\left[\frac{3\Lambda_S + 2E_D}{k_B T}\right] \tag{5.7}$$

where ϕ_{Ga} is the Ga flux , T is the growth temperature, Λ_S is the condensation heat and E_D is the energy barrier for the adatom diffusion on the substrate surface [49]. The NW density should thus monotonously decrease by raising the growth temperature, since the adatom diffusion on the substrate surface is enhanced. Similarly, the NW density should increase with increasing the Ga rate, since the probability to nucleate an island with critical size is increased. Obviously, the experimental results in Figs. 5.18 and 5.19 follow different trends. Therefore, the standard island nucleation theory does not suffice to describe the evolution of the NW density.

The seeming disagreement between the experimental evolution of the NW density and the island nucleation theory can be reconciled by considering the specific nucleation mechanisms of self-induced GaN NWs. These NWs do not nucleate directly with the NW shape but instead as spherical-cap-shaped islands, while the NW shape is reached only after a shape transition (see section 5.1.4 and chapter 6 of this work). Moreover, it has been argued that the shape transition takes place once an energy barrier related to edge effects is overcome. The TEM micrograph presented in Fig. 5.20 shows that, even after a long effective growth time, spherical caps and NWs co-exist: on

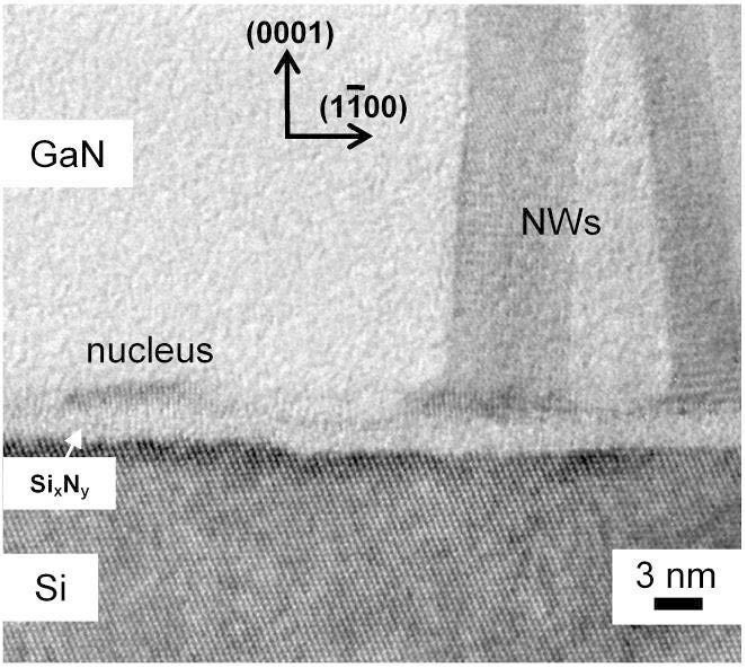

Figure 5.20 – HRTEM of GaN NWs grown for 40 min. The coexistence of spherical cap-shaped islands and fully grown NWs is shown

average in Fig. 5.20, there is one spherical cap for about 2-3 NWs. Hence, some spherical caps undergo the shape transition towards the NW morphology only after long growth time and/or spherical caps are consumed by the radial growth of neighboring NWs and/or spherical caps continue to nucleate. The latter explanation is less likely since the high NW density effectively prevents the impinging fluxes from reaching the substrate surface. At the same time, the prolonged occurrence of the shape transition is consistent with the experimental observation depicted in Fig. 5.17 showing that the NW density increases even after long effective growth time.

The standard nucleation theory is only suitable for the formation of the initial spherical caps but not for the subsequent shape transition that governs the NW density. The energy barrier for the shape transition can more easily be overcome at high growth temperature: in brief, the fraction of spherical caps undergoing the shape transition should drastically increase as the growth temperature is raised for a given Ga rate and effective growth time, accounting for the initial increase in the NW density as shown in Fig. 5.19. The subsequent decrease in the NW density for higher growth temperature is however related to the significant decrease in the spherical cap density predicted by the standard island nucleation theory: although almost all of the

spherical caps undergo the shape transition towards the NW morphology for high growth temperatures of about 785°C, this does not compensate their very low density. Furthermore, the magnitude of the energy barrier itself is expected to be highly dependent upon the V/III ratio and thus the Ga rate: the increase in the NW density with decreasing the Ga rate as seen in Fig. 5.18 suggests that increasing the V/III ratio may be energetically favorable for the shape transition and hence for the formation of GaN NWs. This interpretation is consistent with the fact that the self-induced growth of GaN NWs requires highly nitrogen-rich conditions, as widely reported.

In conclusion, the evolution of the NW density is strongly affected by the nucleation mechanisms involving a shape transition from spherical caps to NWs. Controlling the NW density both requires to control the spherical cap initial density and their subsequent shape transition. Furthermore, increasing the growth temperature leads to a beneficial reduction of the NW coalescence process.

Chapter 6

Epitaxial GaN nanowires on AlN-buffered Si

This chapter presents the *epitaxial* growth of GaN NWs on AlN-buffered Si. The lattice mismatch-induced strain of GaN during nucleation is measured by *in situ* RHEED and *ex situ* HRTEM. It is shown that GaN islands nucleate and undergo a series of shape transitions until finally reaching the NW geometry. The lattice mismatch-induced strain is shown to determine the initial NW diameter. The final shape transition towards the NW geometry is shown to be caused by plastic relaxation of the GaN island and the surface energy anisotropy has been identified as the driving force for this final shape transition.

The need for epitaxial NW growth

As discussed in the previous chapter, unintentional surface nitridation is an issue during the growth of catalyst-free nitride NWs on Si. Due to the high reactivity of Si with atomic nitrogen, the Si surface must not be exposed to the nitrogen flux. A common way to cirvumvent this problem is the growth of a thin crystalline nucleation layer prior to NW growth. However, the material choice for this nucleation layer is limited by several factors:

- **Structure:** The buffer material used has to have an epitaxial relationship to both Si(111) and GaN(0001). Both materials have a similar 3-fold/6-fold in-plane symmetry, therefore the buffer layer material should be chosen accordingly.
- **Quality:** The surface quality of the buffer layer is of crucial importance to the catalyst-free growth of group III-nitride NWs. Our experiments have shown that no NWs will form on buffer layers that have been

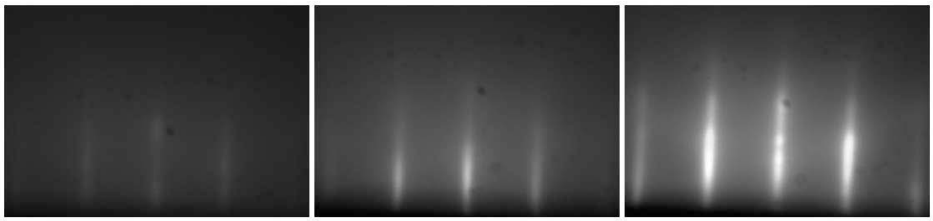

Figure 6.1 – RHEED evolution during GaN growth: No RHEED signal is obtained from the Si (111) surface covered by liquid Aluminum (left). As the nitridation starts, a smooth and monocrystalline AlN layer is formed as evidenced by regular and well defined RHEED "streaks" (center to right)

exposed to the atmosphere. Therefore, the buffer layer has to be grown within the MBE chamber prior to the NW growth.

- **Stability:** The buffer layer has to sustain temperatures up to 800°C during the NW growth.

Given these limitations to the buffer layer material, only GaN and AlN seem appropriate candidates. In fact, GaN would be by far the best buffer material, as it would permit homoepitaxial growth and therefore ensure the best structural properties for the NWs. However, in order to avoid the exposure of Si to the impinging nitrogen atoms, the buffer layer growth has to be initiated by the deposition of several monolayers (ML)of the metallic species and subsequent nitridation. Therefore it is necessary that the metallic species has a good wetting on Si(111). Ga has a high surface tension and a low melting point and therefore does not wet Si(111) [50]. On the contrary, metallic Al can be deposited by several nm thickness on a Si(111) surface, even at high temperature. Therefore the material of choice for the realization of the buffer layer is AlN.

Growth of the AlN buffer layer

After the preparation of the Si surface (see section 5.1.1), the substrate is heated to 780 °C. At that temperature, approx. 10 ML of metallic Al are deposited on the surface. Subsequently, the Al layer is exposed to an atomic N flux of 1 sccm at 250 W plasma power. The N atoms diffuse through the liquid Al and react on the hot substrate surface to form a continuous AlN buffer layer of approx. 5 nm in height [1]. The deposition and nitridation process

[1]We come to this conclusion as HRTEM studies of the ALN buffer layer reveal good epitaxial alignment: Si[111] ∥ AlN[0001]. Therefore the growth has to be initiated at the Si(111) surface

can be followed by RHEED, as shown in figure 6.1: After the Al deposition, no RHEED pattern is observed, as all impinging electrons are diffusely scattered by the liquid Al. After opening the N shutter, the nitridation process begins as testyfied by the appearance of a "streaky" AlN RHEED pattern, an indication for a single-crystalline, homogeneous AlN buffer layer. HRTEM investigation of as-grown samples reveal a AlN buffer thickness of approx. 5 nm, which is considerably thinner than buffer layers used in previous works (e.g. [51]).

The relaxation state of the resulting AlN buffer has been investigated by x-ray diffraction as well as by cross-sectional HRTEM. By X-ray diffraction, an in-plane lattice paramter of $a_{XRD} = 0.311$ nm was obtained, revealing the lattice parameter of the bulk material [52]. High-resolution TEM of the Si/AlN interface shows a regular misfit dislocation network (cf. fig. 6.8) with a mean dislocation distance of 5 atomic planes, thus confirming that the AlN buffer is fully relaxed.

GaN NW growth

GaN nanowires were subsequently grown at a substrate temperature of 800°C, under nitrogen-rich conditions with a V/III ratio of 10.

The bulk lattice constant for GaN is $a^0_{GaN} = 0.319$ nm [52], thus the lattice mismatch between GaN and AlN is:

$$\varepsilon = \frac{a^0_{GaN} - a^0_{AlN}}{a^0_{AlN}} = 0.025 = 2.5\% \tag{6.1}$$

However, epitaxial GaN NWs grown on AlN have been shown to be strain-free [6, 21, 22]. The initial lattice-mismatch induced strain has thus to be relaxed during the nucleation and growth process.

6.1 Strain relaxation during nucleation

In order to elucidate the strain relaxation process during nucleation and growth of GaN NWs, *in situ* RHEED has been performed to monitor the strain state of the growing NWs. As seen in the previous chapter, substrate rotation is a critical issue for NW growth, therefore a programmable motor was used to interrupt substrate rotation at regular time intervals and collect the RHEED pattern of the $[11\bar{2}0]$ azimuth.

Figure 6.2 shows three typical RHEED patterns taken along the $[11\bar{2}0]$ azimuth reflecting the surface morphology during the nucleation and growth of GaN NWs on AlN. Figure 6.2 (a) shows a *streaky* (1×1) pattern, evidence

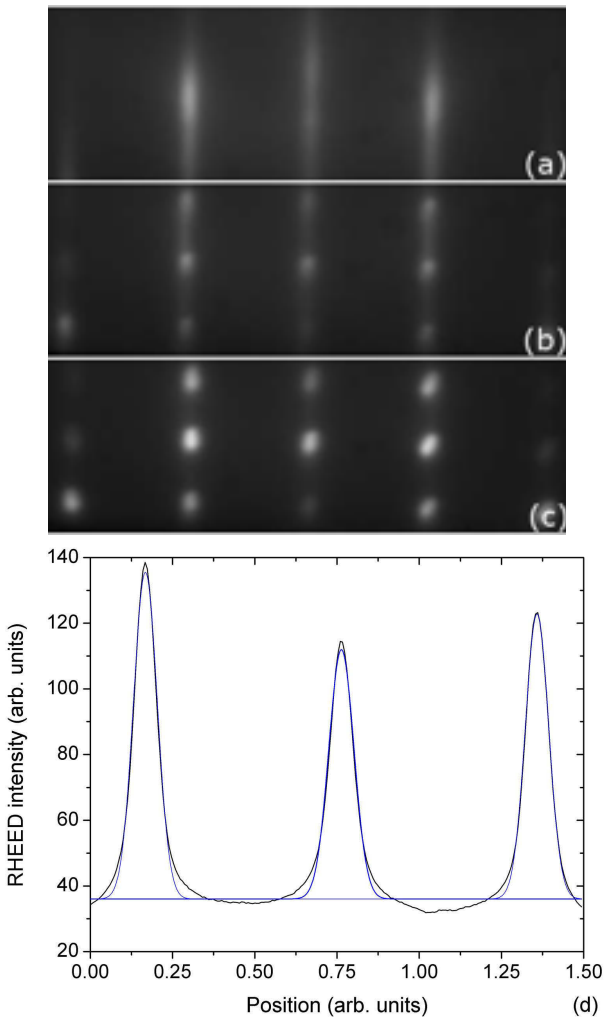

Figure 6.2 – [top] Evolution of the RHEED pattern along the [11$\bar{2}$0 during the nucleation and growth of GaN NWs on an AlN buffer layer: (a) Streaky reflection pattern of the AlN buffer layer. Homogeneous lines show a high surface quality of the AlN buffer. (b) Superposition of the streaky reflection pattern of the AlN buffer layer with a spotty transmission pattern of GaN islands at the onset of nucleation. (c) Spotty transmission pattern of the GaN NWs at end of growth. [bottom] RHEED intensity profile obtained by an integrated horizontal line scan through the RHEED pattern and Gaussian line fit, showing a very high fit precision, used to determine the in-plane lattice parameter.

of a smooth, single-crystalline AlN surface. At the onset of GaN nucleation, a *spotty* pattern characteristic for the transmission of 3D islands appears in superimposition to the AlN streaks (see fig. 6.2 (b)). As growth proceeds and the NWs increase in height, the streaky pattern completely vanishes and only the 3D transmission pattern of the GaN NWs remains (see fig. 6.2 (c)).

Besides elucidating the NW morphology, RHEED offers in-situ monitoring of the in-plane lattice paramter $a_{\parallel}$ and thus delivers insight into the strain relaxation mechanism. As the RHEED pattern is a direct representation of the reciprocal space, the crystal structure can be investigated through RHEED analysis. Namely the distance between two features on the RHEED pattern s is inverse proportional to the spacing d of the two corresponding lattice planes:

$$s_{hkl} \propto \frac{1}{d_{hkl}} \tag{6.2}$$

Therefore, on the RHEED pattern of the AlN buffer layer, the distance s^0_{AlN} between the (00) streak and the $(1\bar{1})$ streak is inversely proportional to the in-plane lattice parameter of bulk AlN, a^0_{AlN}:

$$a^0_{AlN} \propto \frac{1}{s^0_{AlN}} \tag{6.3}$$

The same holds for the RHEED pattern of GaN: the distance $s_{\parallel}$ between the (0004) spot and the $(1\bar{1}04)$ spot is inversely proportional to the in-plane lattice parameter of GaN, $a_{\parallel}$.

$$a_{\parallel} \propto \frac{1}{s_{\parallel}} \tag{6.4}$$

GaN and AlN grow both in pure wurtzite structure. Therefore the contribution of the crystal symmetry to the diffraction pattern is identical for both materials and the in-plane lattice parameter $a_{\parallel}$ of GaN is thus given by:

$$a_{\parallel} = a^0_{AlN} \cdot \frac{s^0_{AlN}}{s_{\parallel}} \tag{6.5}$$

The distances s^0_{AlN} and $s_{\parallel}$ have been precisely measured by applying a linescan and subsequent gaussian fitting to determine the exact streak / spot position on the RHEED pattern. As the AlN buffer is fully relaxed, it can be used as a reference for RHEED analysis. From there on, it is possible to monitor the evolution of the in-plane lattice parameter $a_{\parallel}$ during growth.

Figure 6.3 shows the evolution of the in-plane lattice parameter as a function of growth time. At t = 0, Ga is supplied to the substrate. GaN

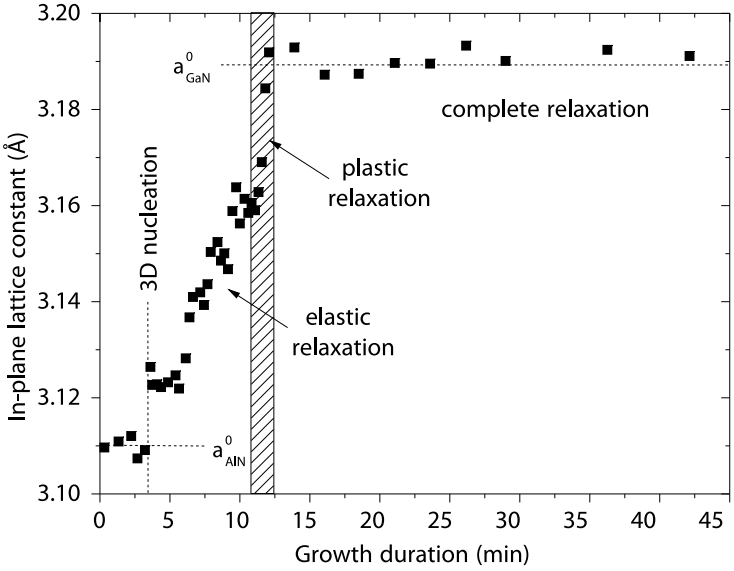

Figure 6.3 – Evolution of the in-plane lattice parameter as a function of growth duration. The bulk lattice constants of GaN and AlN are indicated by dashed lines. GaN islands nucleate coherently strained on AlN. Strain is relaxed by two steps: First an elastic relaxation, followed by a final and complete plastic relaxation.

nucleates compressively strained on AlN. With increasing growth duration, the GaN lattice relaxes until the bulk lattice constant is reached at last. The strain relaxation process can be summarized by 5 sequent phases:

1. Incubation phase
2. Heterogeneous 3D nucleation
3. Progressive elastic relaxation
4. Abrupt plastic relaxation
5. Growth of fully relaxed material

Incubation phase

At the beginning, from t = 0 min to t = 3.5 min, only the streaky pattern of the AlN buffer layer is observed and the in-plane lattice parameter remains unchanged, a clear indication that no 3D growth has started yet. Simultaneously the "overall" RHEED intensity, defined here as the cumulative intensity over the AlN streak and GaN spot positions, decreases continuously (see fig.

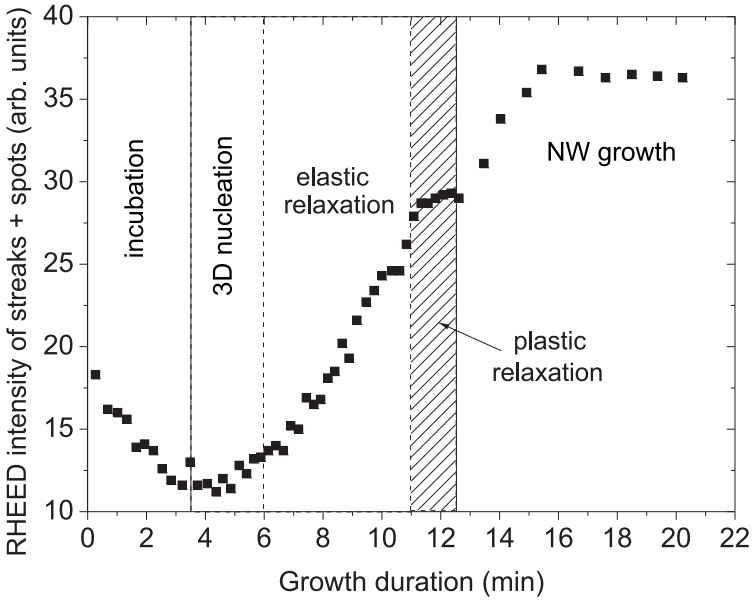

Figure 6.4 – Evolution of the RHEED intensity as a function of time during nucleation and growth of GaN NWs on AlN-buffered Si (111): The incubation phase, where the surface is covered with liquid Ga and metastable GaN clusters is testified by a decrease in the RHEED intensity due to diffuse diffraction. At the onset of nucleation, the intensity increases again as the diffuse elements on the surface crystallize and contribute to constructive RHEED interference. As growth of 3D elements on the substrate surface continues, the material volume probed by RHEED transmission diffraction grows, thus leading to an overall increase of the RHEED intensity.

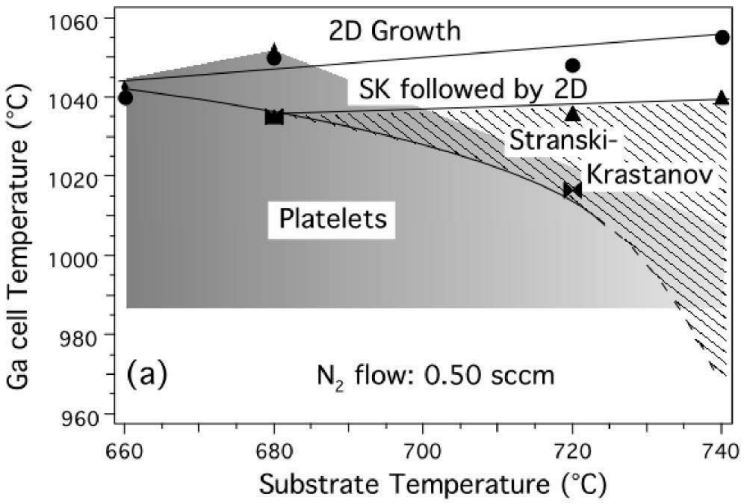

Figure 6.5 – Phase diagram for the growth of GaN on AlN by Mula *et al.* [54]. At low temperatures the Ga surfactant effect leads to a FM growth mode. At higher temperatures a SK growth mode is observed. By extending this diagram to high temperatures (800°C) and highly N-rich conditions (N_2 flux = 2 sccm) a VW growth mode may be adapted.

6.4). This intensity reduction is associated with the generation of surface steps by a roughening of the AlN buffer layer due to the impinging nitrogen atoms and ions [53] and with the formation of 2D GaN clusters on the AlN surface. These *metastable*, i.e. subcritical, clusters may act as seeds for the 3D nucleation of GaN islands.

The incubation time is expexted to depend on the growth temperature since the formation of critical nuclei is mainly governed by the interplay between the processes of adsorption, desorption and surface diffusion of Ga and N adatoms. As the growth is realized at a very high substrate temperature of 800°C, Ga desorption is significant, thus leading to an incubation time of 3.5 minutes. The duration of this incubation phase should depend on the experimental growth conditions, namely Ga flux and substrate temperature.

Heterogeneous 3D nucleation

At about 3.5 min after opening the Ga shutter, the minimum of the overall RHEED intensity is reached, and, at the same time, transmission spots belonging to the GaN lattice appear in superimposition to the streaky AlN pattern (see fig. 6.2b), revealing the initiation of a 3D nucleation and therfore suggesting the absence of a wetting layer. Such an inference is consistent with ex-situ HRTEM analysis of the as-grown samples, which clearly reveals no

evidence of the presence of a GaN wetting layer (see fig. **??** (a)). Moreover, at the onset of 3D nucleation, the in-plane lattice parameter instantaneously jumps to a value of 0.312 nm, which corresponds to a strain relief of 16 % of the natural lattice mismatch. These observations lead to the conclusion that the reduction of strain energy is able to compensate the energy barrier, which needs to be overcome, for the formation of a *critical* 3D GaN nucleus – in conformity with the VW growth mode.

Previous works by Daudin *et al.* [55, 56] have shown that GaN quantum dots nucleate on an AlN buffer according to the SK growth mechanism. This result was proven by measuring a continuous relaxation of the in-plane lattice parameter as well as by observing a 2D wetting layer on top of the AlN buffer by conventional TEM. The combined RHEED and HRTEM analysis of the present work suggests that no continuous wetting layer is formed. These apparently controversial observations can be conciliated considering the specific MBE growth conditions employed in the two experiments:

Mula *et al.* have introduced a growth-mode phase diagram for the GaN-on-AlN system (see fig. 6.5 and ref. [54]). Under Ga-rich conditions, despite of the lattice mismatch, the authors propose a layer-by-layer growth mode that is attributed to the strong surfactant effect of an adsorbed Ga monolayer. At lower Ga fluxes and higher temperatures, i.e. conditions similar to that used by Daudin *et al.* [55], the surfactant effect is reduced and, consequently, a SK growth mechanism will predominate. By extending this phase diagram towards highly nitrogen-rich conditions in combination with high substrate temperatures as used in the present work, a Ga-related surfactant effect is not expected and the wetting behavior of Ga(N) on AlN may be drastically changed, leading to a VW growth mechanism.

Elastic relaxation by shape transitions

After the initial 3D nucleation process, the GaN lattice is still compressively strained. The residual strain ε_r is given by:

$$\varepsilon_r = \frac{a_{\parallel} - a^0_{GaN}}{a^0_{GaN}} \tag{6.6}$$

The critical, cap-shaped, GaN nucleus is still strained by 2.1 %. As growth proceeds, strain will be further relaxed.

Figure 6.6 shows the evolution of the in-plane lattice parameter from nucleation (t = 3.5 min) to full relaxation (t = 12.5 min). After the initial nucleation, the in-plane lattice parameter increases slowly until t = 11 min. Instead of a continuous rise, four distinct plateaus are detected that

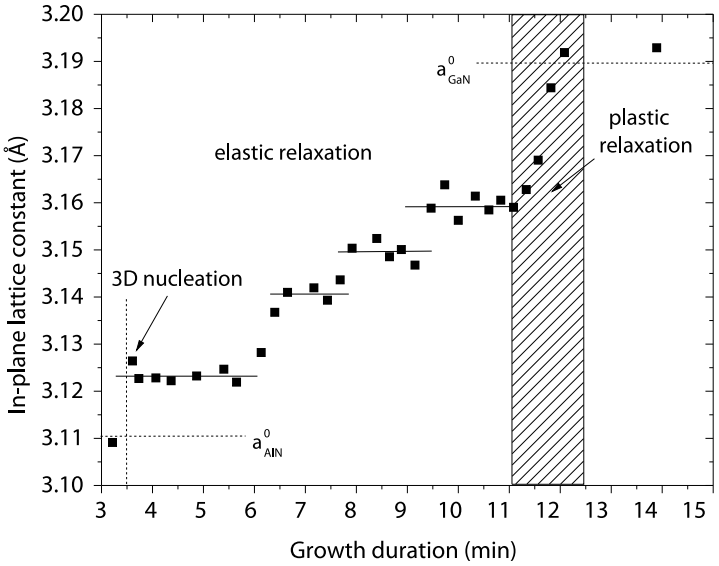

Figure 6.6 – Evolution of the in-plane lattice parameter as a function of growth time during the elastic relaxation period of GaN nucleation on AlN. The elastic relaxation is not continuous but occurs by steps: four distinct strain levels are observed and can be associated to four characteristic island shapes.

correspond to four different residual strain levels of ε = 2.1, 1.5, 1.2 and 0.9 % respectively. Due to the fact that no plastic relaxation is observed by HRTEM, this relaxation behaviour is elastic and must be completely driven by shape transitions of the coherent 3D GaN islands. Indeed, four predominant island shapes, corresponding to the four different strain levels, have been identified by HRTEM analysis (see fig. 6.7, page 70). These island shapes are in chronological order:

1. a critial cap-shaped nucleus
2. a truncated pyramid with $\{1\bar{1}0x\}$ side facets
3. a truncated pyramid with $\{1\bar{1}03\}$ side facets
4. a full pyramid with $\{1\bar{1}03\}$ side facets

The strain relaxation during epitaxial growth thus passes through several discrete steps, each of which can be associated to a first-order shape transition at a critical island size [57]: each island with a given size coarsens and, simultaneously, increases its strain energy until reaching a critical size.

At this size, the shape transition is induced to form new steeper side facets, which are more efficient in lowering the total energy by strain relief. Under equilibrium, every island shape corresponds to the lowest total energy configuration for a specifice island size. The driving force for this mechanism is the lowering of the total free energy, therefore the decrease in the strain energy must be stronger than the increase in energy by the formation of a new facet. A first-order transition from one shape to the other is therefore associated with an energy barrier.

Such a barrier should scale with the magnitude of strain relief. In particular the highest step on fig. 6.6 is related to the initial transition from the spherical cap-shaped nucleus to a truncated pyramid, revealing that faceting is the most efficient elastic strain relief mechanism but has the highest energy barrier. Furthermore is is remarkable that the first two shape transitions result in steeper side facets of the island, corresponding to larger inclination angles and thus approaching a more NW-like geometry. During the third transition from truncated pyramid to full pyramid the $\{1\bar{1}03\}$ side facets are not altered. Nevertheless, the strain relief is not continuous and an abrupt transition is observed. The discrete transition character is most likely explained by the high stability of the $\{0001\}$ facet, representing an energy barrier, that has to be overcome.

Abrupt plastic relaxation

After about 11 minutes of growth, there is a significant change of slope in the evolution of the in-plane lattice parameter on fig. 6.6. Within only 90 seconds, we observe a fast and abrupt strain relaxation, reaching the in-plane lattice parameter equal to the value of bulk GaN material. This is associated with a more efficient plastic relaxation, resulting in dislocated islands. Since nitrides present a high dislocation energy, elastic strain relaxation via shape transitions is energetically favorable. At a critical island shape, however, no further shape transitions to steeper side facets are available and island coarsening leads to an increase of the stored elastic strain energy and therefore in the total free energy. At a critical island size, the accumulated strain energy will finally balance the dislocation energy cost, thus leading to to dislocation nucleation [58, 59]

6.2 Origin of the initial nanowire diameter

The experimental data obtained by an *in situ* monitoring of the in-plane strain in GaN NWs has shown that the lattice-mismatch-induced strain is

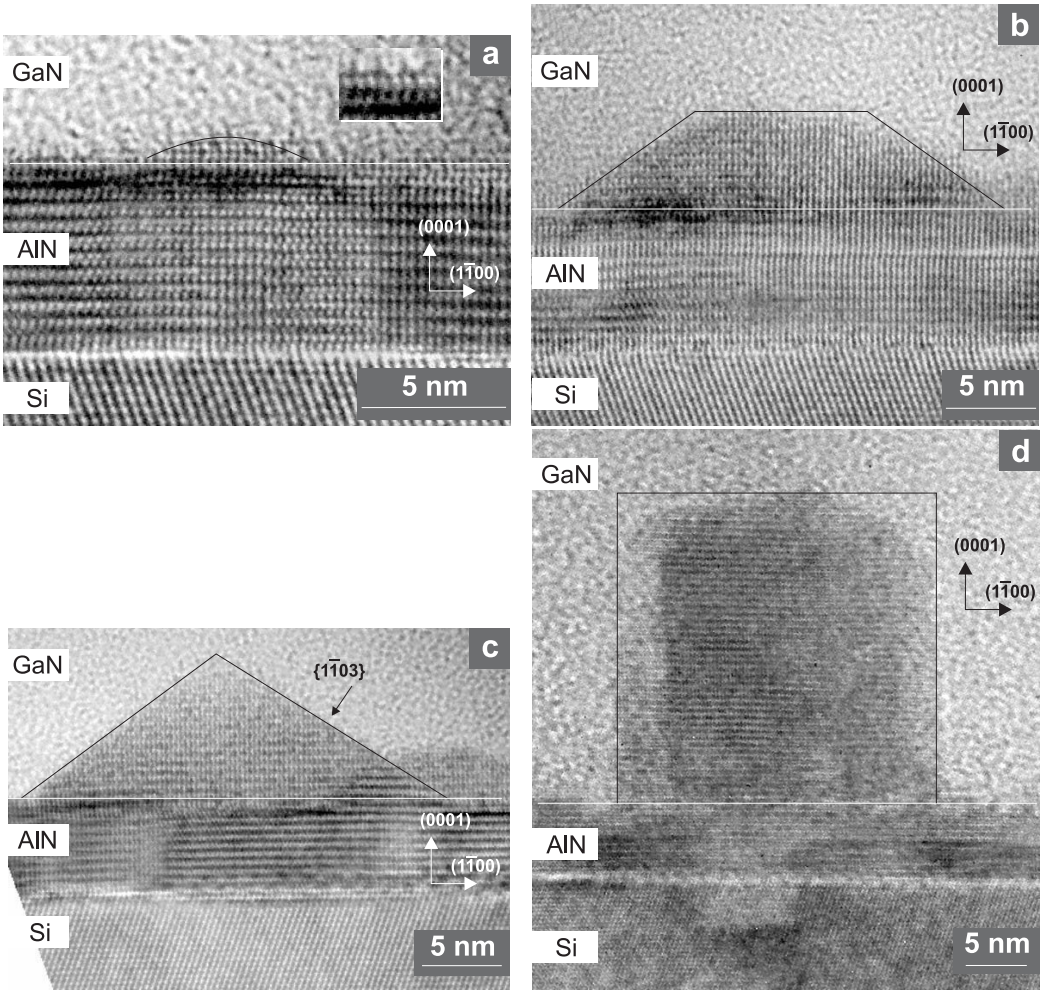

Figure 6.7 – HRTEM images collected on dedicated GaN samples grown for 4.5, 9, 10 and 15 minutes, revealing the following respective GaN island shapes during the nucleation process: (a) spherical cap-shaped island; the inset shows a higher magnification of the topmost AlN monolayers. (b) truncated-pyramid-shaped island (c) full-pyramid-shaped island, (d) nanowire

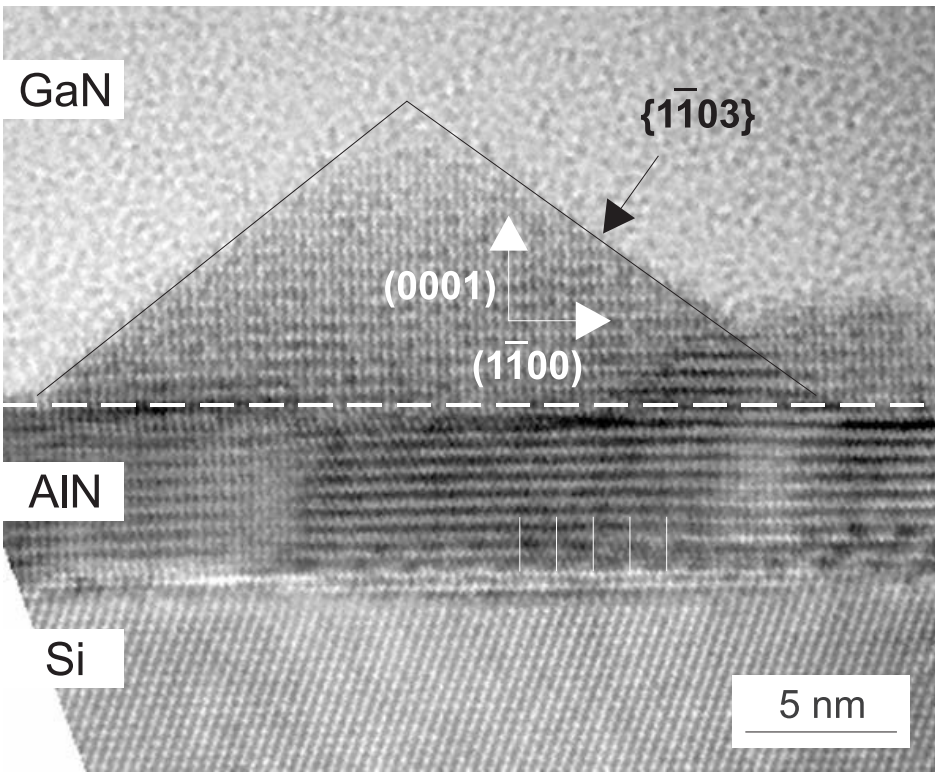

Figure 6.8 – HRTEM image of a full-pyramid shaped GaN island. The AlN / GaN interface is defect-free thus revealing that the island is coherently strained. Inclined $\{1\bar{1}03\}$ side facets account for the elastic strain relaxation of the GaN lattice. The AlN buffer layer presents regular misfit dislocations (indicated by white streaks), revealing the full relaxation of the AlN buffer layer.

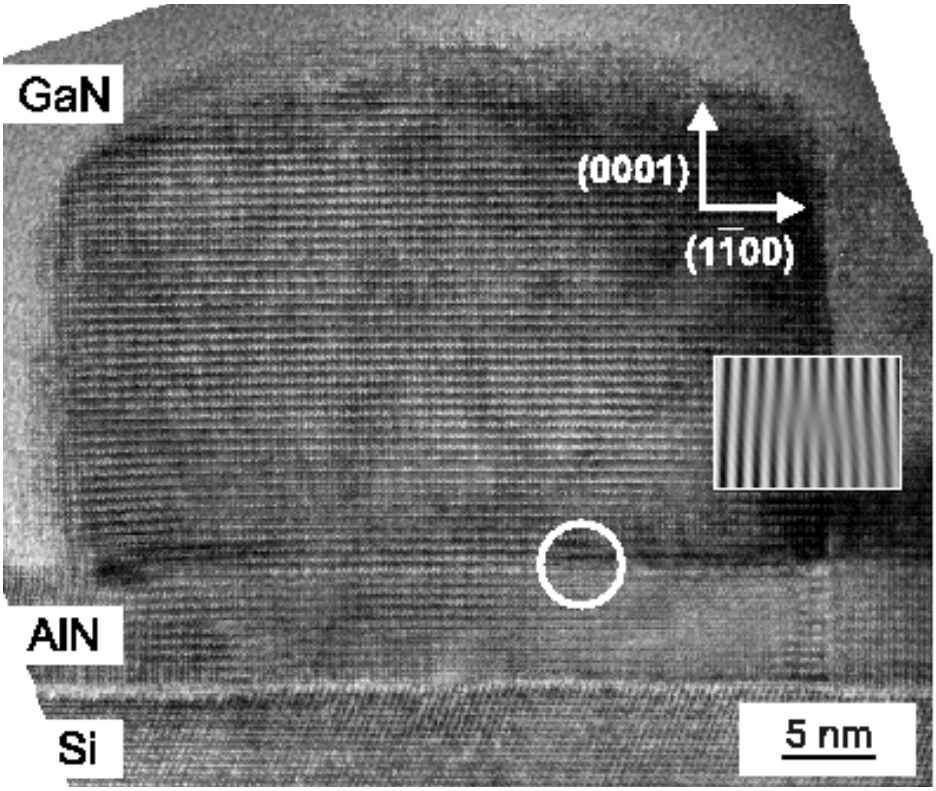

Figure 6.9 – HRTEM image of a GaN NW. The final shape transition from pyramid-shaped island to NW has been completed and vertical $\{1\bar{1}00\}$ side facets as well as a flat $\{0001\}$ top facet have been formed. At the AlN / GaN interface, a misfit dislocation has been nucleated. The inset shows a Fourier-filtered enhancement of the dislocation, strengthening its edge character.

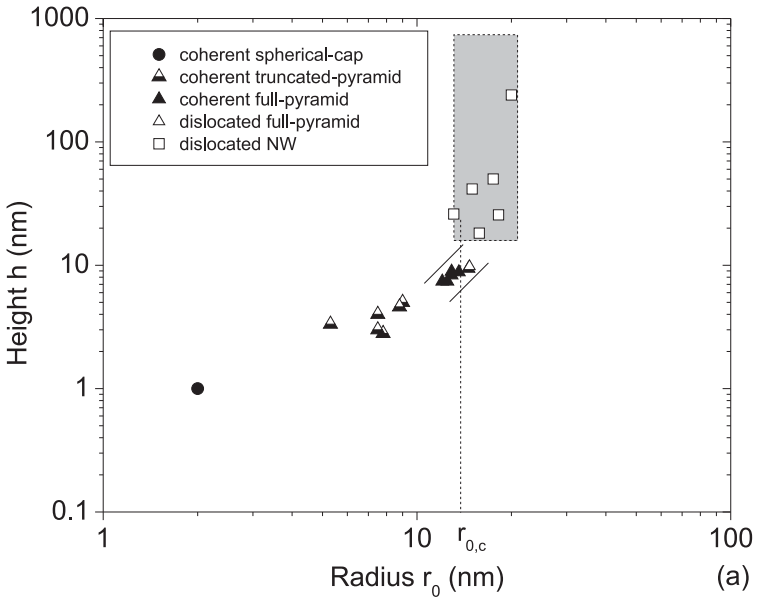

Figure 6.10 – Height h as a function of radius r_0 obtained from HRTEM image for the different shapes of GaN islands as growth proceeds. The dashed line corresponds to the eperimental critical radius $r_{0,c}$ determined for the occurrence of plastic relaxation.

relieved in two steps: Initially, strain is relaxed elastically by several shape transitions of the strained GaN islands. Upon reaching a critical island size (diameter), the residual strain leads to the formation of a misfit dislocation at the AlN/GaN interface and the transition to the nanowire geometry with vertical sidewalls. Still, the experimental data in not sufficient to determine the critical island size, at which the dislocation is nucleated, neither does it provide information whether dislocation formation happens before or after the shape transition to NW geometry.

Critical diameter for plastic relaxation

In order to determine the critical diameter at which the plastic relaxation and the final shape transition toward the NW geometry occurs, HRTEM analysis has been performed on dedicated samples grown with different growth durations and therefore featuring different island shapes. The height h, radius r_0 and shape of the islands as well as their relaxation mode (namely, whether plastic relaxation by misfit dislocation creation has occured or not) were recorded.

Figure 6.10 summarizes all HRTEM data showing the evolution of the

island height h as a function of the island radius r_0 [2] The experimental data points are represented by icons representing the island shape, i.e. coherent cap-shaped nucleus (circle), coherent truncated pyramid (semi-filled pyramid), coherent full pyramid (filled pyramid), dislocated pyramid (empty pyramid) and finally nanowire (square). Sample HRTEM images of the different shapes are depicted in fig. 6.7.

Although the catalyst-free nucleation of GaN on AlN is a follows a heterogeneous nucleation regime, and therefore can lead to the observation of two consecutive dinstinct island shapes on the same sample at a given growth time, fig. 6.10 clearly reveals that the island shape is strictly dependant on the island diameter: each specific island shape can be associated to a window of specific island dimensions. The successive shape evolution of the islands with increasing growth duration (i.e. island volume), as discussed in the last section, is thus confirmed by fig 6.10.

Furthermore, two distinct regions driven either by elastic or plastic relaxation can be distinguisehd. Interestingly, the elastic relaxation-driven region, namely the coherency region, is only composed of sperical-cap, truncated and full pyramid-shaped islands. The shape evolution of islands in this regions aims at minimizing their total free energy by relieving in particular their strain energy as previously discussed. On the contrary, the plastic relaxation-driven regions only involves one full pyramid-shaped island and the NWs, as revealed by the empty icons in fig. 6.10. Consequently, the mechanism for the formation of the very first NWs is strongly related to the plastic relaxation process: a critical radius of 13-15 nm, at which the plastic relaxation occurs, is experimentally deduced in fig. 6.10.

This critical radius differs obviously from the critical radius of 7 nm obtained for the self-induced growth of GaN NWs on different substrates [60]. Furthermore, since each full pyramid-shaped island has identical $\{1\bar{1}03\}$ facets with an angle of 32 ° with respect to the substrate surface, its dimensions and namely its height h and radius r_0 are strongly correlated. a constant aspect ratio $p = h/r_0$ of about 0.62 corresponding to $\tan(32°)$ is determined. Only a small domain of the elastic relaxation-driven region is thus explored by full pyramid-shaped islands, as indicated by the two delimiting straight lines in fig. 6.10.

After the plastic relaxation and namely the shape transition toward the NW shape, there is a significant change of slope in the evolution of the island's

[2]The island height h was measured directly on HRTEM images. This leads to some uncertainty as HRTEM samples are thin slices cut from the sample and thus may cut an island not at it's maximum height. However the trend pictured in fig. 6.10 is endorsed by a statistical analysis on a large number of islands (> 100), thus this source of error can be neglected.

aspect ratio: the axial growth rate for NWs is much higher that the radial growth rate, therefore, the diameter distribution of the first NWs is very narrow, as depicted by the grey color region in fig. 6.10. In other words, the initial radius of self-induced GaN NWs is explicitely defined here by this grey color region and appears to be strongly correlated to the process of plastic relaxation.

Theoretical considerations

The original NW radius appears to be closely related to the process of plastic relaxation and the transition from full pyramid-shaped islands to NWs. In the following, three theoretical models are presented, that treat with plastic relaxation especially for the geometries mentioned above:

Matthews and Blakeslee

In 1974, J. W. Matthews and A. E. Blakeslee proposed a model for determining the critical thickness of two-dimensional films grown by heteroepitaxy [59]. They consider misfit dislocations in a GaAs / Ga(As,P) (001) superlattice grown on a GaAs (001) substrate. TEM investigation of the as-grown samples shows that for layer thicknesses about a critical value, paired misfit dislocations with a Burgers vector of $\vec{b} = 1/2 <110>$ and line directions are [110] and [$\bar{1}$10], which are parallel to the {111} slip planes. They further observed that the mean distance between two adjacent dislocations is $S = h \cot 55°$ where h is the thickness of the GaAs or GaAsP layers and 55° is the angle between the {111} slip plane and the (001) interface between layers.

To determine the critical thickness for the formation of a misfit dislocations *in a two-dimensional superlattice*, they balance the forces applying on dislocation lines: F_ϵ, the force exerted by the misfit strain, and F_l, the tension in the dislocation line. By considering isotropic materials with identical elastic constants, they find the following expression for the critical layer thickness h_c:

$$h_c = \frac{b}{2\pi f} \frac{1 - \nu \cos^2 \alpha}{(1+\nu)\cos\lambda} \left(\ln \frac{h_c}{b} + 1 \right) \tag{6.7}$$

where b is the dislocation's Burgers vector, f the lattice mismatch, ν the Poissons ratio of the deposited material and α the angle between the dislocation line and it's Burgers vector. λ is the angle between Burgers vector and the normal in the interface to the dislocation line direction.

Matthews and Blakeslee present a model suited to predict the critical thickness for the nucleation of misfit dislocations in the case of a 2D superlattice of epitaxial layers. Even though this model may not be applied on the 3D nucleation of GaN on AlN, it has been the base for more recent models that predict critical dimensions for misfit dislocation nucleation in 3D nanostructures.

Tillmann and Förster

In 2000, K. Tillmann and A. Förster proposed a model to calculate the critical dimensions for the nucleation of interfacial misfit dislocations into epitaxially grown $In_{0.6}Ga_{0.4}As$ islands on GaAs (001) [61]. They consider a conical island form, which is equal to the "full pyramids" discussed in the previous section. Further, their calculations are based on an energy equilibrium approach, considering that the islands are in a thermodynamic equilibrium and strain relaxation is not influenced by growth kinetics. By balancing the strain energy gain related to the process of plastic relaxation and the energy associated with the strain field of the misfit dislocation, the critical radius $r_{0,c}$ is given implicitly as a function of the aspect ratio $p = h/r_0$ by the following equation:

$$\begin{aligned} r_{0,c} =& \frac{2}{b_{eff}\epsilon_0}\left\{ \frac{b_{eff}^2}{8(1+\nu_{GaN}} + \left[\cos^2\theta + \frac{\sin^2\theta}{1-\nu_{GaN}}\right] \right. \\ & \times \left[\ln\left(\frac{r_{0,c}\sqrt{p}(1-\sqrt{1-\frac{\pi^2}{16}})}{|\vec{b}|} \right) + 1 \right] \\ & \left. \times \left[\Gamma(\lambda, V)\frac{1-\nu_{GaN}}{1+\nu_{GaN}}\frac{\mu_{AlN}|\vec{b}|^2}{\mu_{AlN}+\mu GaN} \right] \right\} \end{aligned} \tag{6.8}$$

in which μ_{GaN} and μ_{AlN} are the respective shear moduli of GaN and AlN, ν_{GaN} is the Poisson's ratio of GaN, ϵ_0 is the lattice mismatch between GaN and AlN, $\vec{b}$ is the Burgers vector of the misfit dislocation and b_{eff} its edge component, θ is the angle between the dislocation line and the Burgers vector. $\Gamma(\lambda, V)$ represents a geometry factor only depending on the length of the misfit dislocation λ and on the island volume V. For full-pyramid shaped islands, it is given by:

$$\Gamma(\lambda, V) = \frac{\lambda r^2}{4\pi V} = \frac{3}{8\pi p} \tag{6.9}$$

Frank Glas

Another approach for calculating the critical dimensions leading to the nucleation of dislocations in semiconductor NWs has been presented by Frank Glas in 2006 [62]. He bases his calculations on a model of a strained layer on top of a free-standing NW. Using an equilibrium approach and therefore disregarding the kinetics of dislocation nucleation, he determines the excess energy of a dislocated NW with respect to a similar dislocation-free NW. Thus he implicitely obtaines a critical radius $r_{0,c}$, corresponding to the occurrence of dislocation nucleation in the NW:

$$\frac{2\pi}{A_\nu}\left(\frac{4b_{eff}^2}{\pi^2}-\frac{4b_{eff}\epsilon_0 r_{0,c}}{\pi}\right)+\frac{(1-\nu_{GaN}\cos^2\theta)b^2}{2\pi(1+\nu_{GaN})}\left(1+\ln\frac{2r_{0,c}}{\pi b}\right)=0 \quad (6.10)$$

in which A_ν is a numerical constant weakly dependent upon the Poisson's ratio, which equals 27.3 ± 0.55 for $\nu = 1/3$.

Comparison to experimental data

The experimental data of the typical dimensions for full pyramid-shaped islands are presented in fig. 6.11 and superimposed on the border region delimiting elastic and plastic relaxation, as predicted by Tillmann *et al.* in eq. 6.8. The width of the border region between solid and dashed lines takes into account the uncertainties of the mechanical constants used for GaN [15, 63]. It is clearly shown that the approach given by Tilmann *et al.* is in very good agreement with the critical dimensions observed for full pyramid-shaped GaN islands on AlN: the critical radius $r_{0,c}$ for plastic relaxation in GaN islands is found to be 13-14 nm from experimental results compared to 11.5-13 nm by theoretical predictions from eq. 6.8.

On the contrary, the model developed by Frank Glas is not in agreement with our experimental data, as the critical radius for plastic relaxation in GaN NWs $r_{0,c}$, as predicted by eq. 6.10, is of 32-36 nm.

As a consequence, one can deduce that the agreement of experimental data with the approach given by Tillmann *et al.* and not with the approach presented by Glas provides strong evidence that the plastic relaxation process, namely the nucleation of a misfit dislocation at the GaN / AlN interface, occurs within full pyramid-shaped islands and not within NWs. In other words, the plastic relaxation process occurs prior to the shape transition towards the NW morphology. Thus the final shape transition takes place from a dislocated full pyramid-shaped island toward a dislocated NW. Furthermore, the initial radius of the first NWs directly corresponds to the critical radius

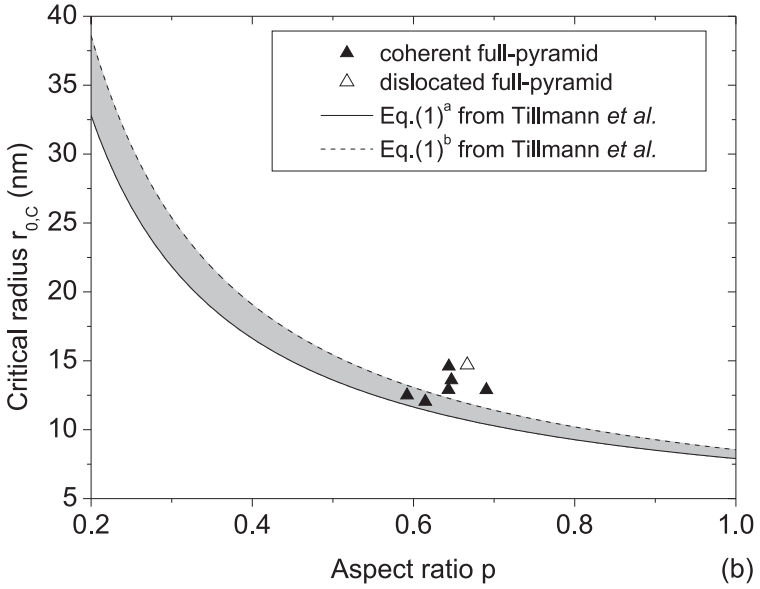

Figure 6.11 – Radius r_0 as a function of aspect ratio $p = h/r_0$ obtained from HRTEM images of full-pyramid-shaped GaN islands. The grey color regions corresponds to the critical radius $r_{0,c}$ predicted by Tillmann *et al.* from eq. 6.8 with $\epsilon_0 = 2.41\%$, $b = a = 3.189$ Å and $\theta = 90$ ° for one pure-edge dislocation, $\mu_{AlN} = 142.2$ GPa. Solid line: $\nu = 0.203$ and $\mu_{GaN} = 127.8$ GPa [15], dashed line: $\nu = 0.353$ and $\mu_{GaN} = 64.9$ GPa [63]

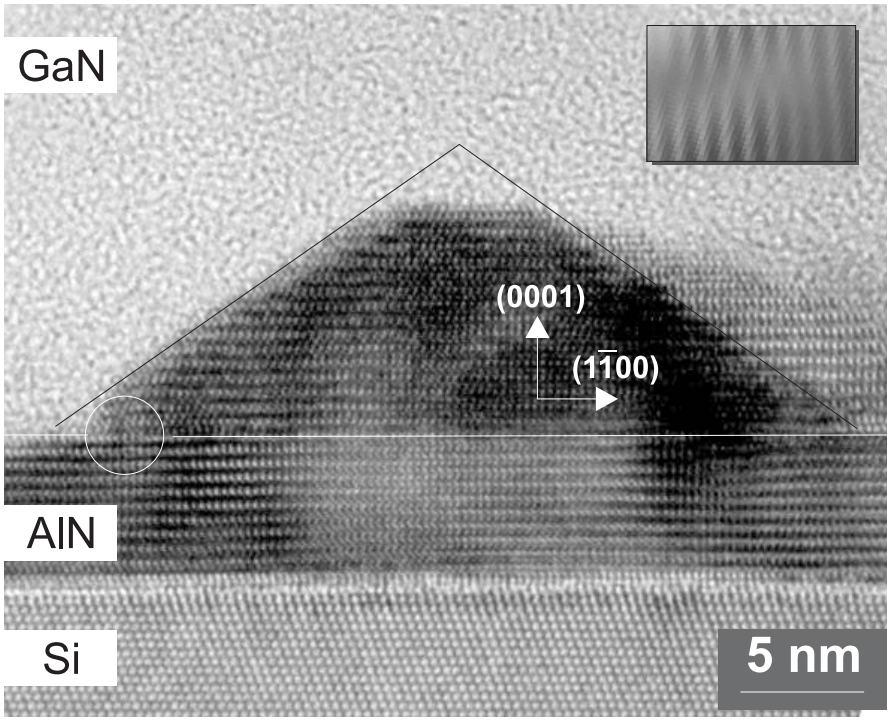

Figure 6.12 – HRTEM image of a plastically relaxed island. The pyramid contours are outlined by the dashed lines. A misfit dislocation has been nucleated at the very edge of the pyramid in the GaN/AlN interface (indicated by the white circle) to accomodate the misfit strain. The inset shows a Fourier-filtered enhacement of the misfit dislocation.

required for the plastic relaxation by misfit dislocation nucleation within full pyramid-shaped islands.

The specific mechanism of plastic relaxation

It has been shown by theoretical considerations of plastic relaxation in semiconductor nanostructures that plastic relaxation takes part in full pyramid-shaped islands. Figure 6.12 shows a full pyramid-shaped island with one misfit dislocation. The dislocation is located very close to the island edges, as revealed by the inset in fig. 6.12. Such a spatial position suggests that the dislocation is nucleated at the island edges where the strain concentration is maxiaml, as theoretically predicted and observed experimentally for instance in the $In_xGa_{1-x}As$ / GaAs material system [64–66]. The dislocation is of mixed type with a Bergers vector of $1/3 < 11\bar{2}0 >$ and an edge component of more than 80 cent.

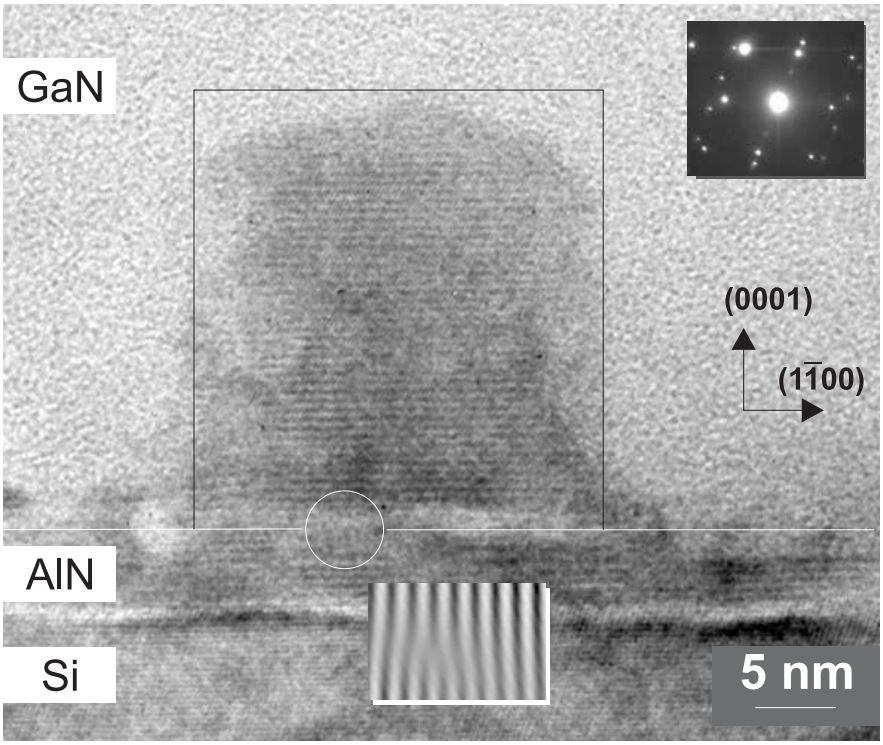

Figure 6.13 – HRTEM image of a plastically relaxed NW. The NW contours are outline by dashed lines. The misfit dislocation is located near the center of the NW (white circle), a Fourier-filtered enhancement is shown in the bottom inset. The top inset shows a selected area electron diffraction pattern of this nanowire, revealing that the GaN lattice is fully relaxed.

On the contrary, the misfit dislocation in the NWs are located close to their center but not completely in their center, as revealed in fig. 6.13. Marzegalli *et al.* [67] recently evidenced that the relative energy gain in dome- and bard-shaped islands in the SiGe / Si material system is maximized when the dislocation is located close to the island center at a distance of 0.3 times the island diameter. The misfit dislocation in the NW could thus be located where its efficiency for the overall strain relaxation in the NW is maximal. Furthermore, selected area electron diffration (SAED) on the dislocated NW reveals that the NW is completely relaxed (see inset of fig.6.13): from a line scan along the $(1\bar{1}00)$ direction, an in-plane lattice parameter of 3.19 ± 0.01Åis determined. This is consistent with the fact that one misfit dislocation is sufficient to entirely relieve the lattice mismatch-induced strain. As the radii of dislocated full pyramid-shaped islands and dislocated NWs are similar, one can deduce that the movement of the misfit dislocation accounts for its relative position change within the two different structures. The dislocation moves from the edges of full pyramid-shaped islands towards their center so as to relieve strain more efficiently. Once the dislocation reaches the center of the island and thus permits complete strain relaxation, a shape transition towards the NW geometry occurs.

Therefore, the experimental observations suggest that dislocation nucleation is essential for the growth of self-induced NWs, although it occurs within full pyramid-shaped islands. Indeed, such a formation favors the subsequent shape transition from dislocated full pyramids to dislocated NWs by entirely relieving the lattice mismatch-induced strain.

6.3 Shape transition towards NW morphology

Several theoretical approaches are based on thermodynamics considerations to account for the shape transitions occurring during the QD growth, in the Si/Ge material system for instance [57, 68–70]. These approaches mainly state that the preferential island shape is given by the minimization of the total free energy. In other words, the strong variation of the total free energy for the two considered distinct morphologies can induce a large driving force in a shape transition: it is thus expected that, for a given volume, the total free energy of dislocated NWs is significantly smaller than the one of dislocated full pyramid-shaped islands. Several distinct energies contribute to this driving force [70, 71]: the shape transitions are usually mainly driven by the interplay between the elastic strain energy and the total interface and surface energies of all the facets composing the dislocated full pyramid-shaped island and the dislocated NW, respectively. The elastic strain energy

can originate from the strain induced by the lattice mismatch and the strain related to the discontinuity of surface stress at island edges, as discussed by Shchukin *et al.* [71]. Yet, once the misfit dislocation reaches the center of full-pyramid-shaped islands, the lattice-mismatch-induced strain is relieved so that only the contribution of edge effects could be involved in the elastic strain energy. Nevertheless, the ratio of the typical dimensions of edges over the radius of full-pyramid-shaped islands is relatively low so that edge effects could only play a minor role in the driving force of the shape transition. A similar discussion can also be made concerning the edge energy. In addition, given that the shape transition occurs between dislocated full-pyramid-shaped islands and dislocated NWs with similar radii, the interface area does not change significantly between the two different morphologies: this indicates that the increase in the interface area costs a very large energy, which prevents in turn the interface from spreading itself. One can thus exclude that the interface energy contributes to the driving force of the shape transition, since it remains constant for both dislocated full-pyramid-shaped islands and dislocated NWs.

Consequently, only the surface energy can play a major role in such a shape transition: indeed, full-pyramid-shaped islands and NWs present different facet orientations. Yet, the value of the surface energy depends on the crystallographic orientation of the involved facets [72]. In particular, the surface energies of $\{0001\}$ and $\{1\bar{1}00\}$ planes are relatively small with respect to the surface energy of $\{1\bar{1}03\}$ facets, which is expected to be much higher [72, 73]. Nevertheless, no value for the surface energy of $\{1\bar{1}03\}$ facets is mentioned in the literature. One can however maintain that, once the lattice-mismatch induced strain vanishes, the driving force for the shape transition is governed by the anisotropy of surface energy and by edge effects, as the respective major and minor contributions.

Simple thermodynamic considerations can account for the preferential growth of NWs starting from dislocated full-pyramid-shaped islands, which are completely relaxed. Nevertheless, GaN islands adopt the equilibrium shape, namely NWs, for which the total free energy is minimal, as long as both growth and coarsening processes are relatively slow compared to the time scale required for the shape transition. Furthermore, growth could also help with the shape transition since material is supplied in such a way that it can easily arrange into a new shape, in correlation with geometrical effects for instance [74]. Therefore, varying the growth temperature or the V/III ratio can directly change the time scale involved and even the nature of the mechanisms involved; this can also be the case when increasing the lattice mismatch: such a growth could induce a shorter time scale for all the nucleation processes described here, limiting for instance the nature and the

number of the shapes involved. It could also lead to a plastic relaxation process involving a larger number of misfit dislocations and occurring at smaller critical dimensions. However, it is expected that the nucleation processes for the self-induced growth of GaN NWs on highly lattice-mismatched substrates is similar as regards the general aspects discussed here. In other words, the specific growth conditions for GaN NWs play an essential role in the involved mechanisms by directly influencing kinetic aspects for instance.

In particular, the growth of GaN NWs requires a high V/III ratio, which is often coupled with a high growth temperature [2, 34, 75, 76]. As the surface energy of a given plane strongly depends on the surface reconstruction at work, the control of the V/III ratio is crucial [77]. Indeed, the anisotropy of surface energy as the main driving force could be efficient enough to favor the NW growth only in an appropriate window of V/III ratio: the modulation of surface energies for $\{0001\}$, $\{1\bar{1}00\}$ and $\{1\bar{1}03\}$ facets could induce the shape transition towards the NW morphology only if highly N-rich conditions are strictly used. Furthermore, similar arguments can also account for the Volmer-Weber mechanism that is involved in the self-induced growth of GaN NWs compared to the Stranski-Krastanov mechanism reported for the growth of GaN QDs.

Chapter 7

(In,Ga)N/GaN nanowire heterostructures

This chapter shows the growth of embedded (In,Ga)N/GaN NW heterostructures. The strain profile and chemical composition of these heterostructures are precisely measured by a combination of HRXRD and a geometric phase analysis on HRTEM images. Finite element calculations (FEM) are carried out to support the experimental data. A possible band diagram for an *inter-well* emission between two stacked embedded (In,Ga)N insertions in a GaN NW is presented.

As discussed in the previous chapters, GaN NWs are promising building blocks for optoelectronic devices. Ever since the bandgap of In has been found to be 0.6-0.7 eV, (In,Ga)N NWs have received great interest for being able to emit light in the visible spectrum. Several groups have successfully built LEDs based on (In,Ga)N NWs, e. g. [78]. LEDs based on (In,Ga)N/GaN NW heterostructures have been first realized by Kishino *et al.* in 2004 [8]; several other groups have also succesfully built working LEDs, recently achieving the emission of white light [79].

However, whereas the building a (In,Ga)N/GaN NW based LED has been achieved, some of the more fundamental issues have not been solved. Up to date, the *controlled* incorporation of In into GaN NWs has not been demonstrated, furthermore the investigation of such structures is difficult, as the In content of an (In,Ga)N/GaN NW cannot be easily measured.

The relation between the structural properties of embedded (In,Ga)N/GaN heterostructures has been subject to several investigations: Bardoux *et al.* [80] and Park *et al.* [81] have carried out an in-depth optical caracterization, but lack structural information to completely assess the In incorporation. Lin *et al.* [79] carry out an exclusively optical study and claim that (In,Ga)N

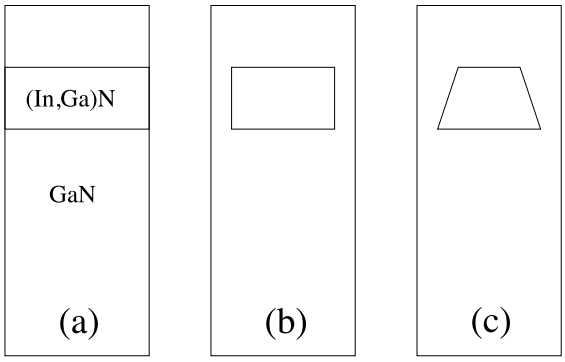

Figure 7.1 – Possible geometry of (In,Ga)N/GaN NW axial heterostructures: (a) quantum well, (b) embedded quantum dot with vertical sidewalls, (c) embedded quantum dot with inclined sidewalls

quantum dots have been embedded strain-free in an GaN NW. Finally Armitage *et al.* [82] and Chang *et al.* [83] offer a first combined study of TEM/EDX and luminescence analysis, but lack the necessary precision to completely asses the embedded nanostructures.

Furthermore, the general morphology of (In,Ga)N/GaN NW heterostructures is still controversely disussed, as several different geometries might be possible: an (In,Ga)N quantum well that extends horizontally through the entire GaN NW, an embedded insertion with vertical (i. e. parallel to the NW) sidewalls or and embedded insertion with inclined sidewalls (see fig. 7.1).

7.1 Growth and structural properties

As described above, the incorporation of In into GaN nanowires is a technical challenge due to temperature issues: Nitride NW growth needs high adatom mobilities on the substrate surface. These are guaranteed by high growth temperatures. As seen in chapter 3, GaN NW material quality is optimum for temperatures higher than 780°C. However, at these high temperatures, InN decomposition and re-evaporation are critical issues. Therefore the (In,Ga)N quantum structures have to be grown at relatively low temperature. Based on literature, the optimum temperature range for the growth of (In,Ga)N NWs is 600°C -650°C. Thus, there is a big discrepancy between optimum growth temperatures for the two materials involved in the (In,Ga)N/GaN heterostructure.

The heterostructure of choice for this case study is a GaN NW with two vertically stacked identical (In,Ga)N insertions of approx. 10 nm in thickness, separated by a GaN barrier of a similar thickness (cf. fig 7.2). The GaN NW

base can be grown at high temperature (780°C) as at that time, there is no In in the system. The active region, i.e. the (In,Ga)N insertions and GaN barrier, will then be grown at low temperature (600°C). Thus, the structure compounds two (In,Ga)N insertions grown on two different GaN substrates (as the GaN barrier is grown at low temperature).

In order to obtain an optically active structure, it is important to grow a siginificant GaN "cap" on top of the two insertions, as it is necessary for carrier generation that are to recombine within the (In,Ga)N layers. Consequently, it is important that this GaN "hat" be of high crystal quality, i. e. grown at high temperature. This leads to the following issues:

- If the GaN cap is grown at a low temperature of 600°C to 650°C, the GaN material quality will be low, due to a high density of defects (evidenced by TEM investigation), which are detrimental to the optical qualities of the heterostructure.

- If the GaN cap is grown at the optimum temperature of 780°C, the underlying In will diffuse trough the barrier and into the NW core so that the entire NW top region will present a *quasi* homogeneous In concentration instead of an (In,Ga)N/GaN heterostructure.

- InGaN tends to segregate and/or build clusters during growth [84], therefore a *radially* homogeneous In concentration is hard to achieve.

Thus, one has to grow the GaN cap at high enough temperature for an optically active crytal, at the same time, the In diffusion into the GaN NW core has to be prevented. The growth recipe we succesfully used is described in fig. 7.2.

Other important parameters for the growth of (In,Ga)N/GaN NWs are the V/III ratio as well as the In/Ga ratio. A series of 10 samples has been grown with two different V/III ratios of 5.9 and 6.3, covering In/Ga ratios from 0.5 to 24.1. A complete list of the realized growth experiments is given in the appendix on page 101.

Unfortunately, due to technical issues with the MBE equipment, the growth experiments have been limited to this single series. However, in one of these samples (M8872), two embedded (In,Ga)N insertions have been succesfully grown in a high-quality GaN NW. In the following, we will present a structural and optical characterization of this sample.

GaN cap	730°C	30 min
GaN barrier 2	600°C	10 min
InGan 2	600°C	10 min
GaN barrier 1	600°C	10 min
(In,Ga)N 2	600°C	10 min
GaN base	780°C	90 min

Figure 7.2 – Growth sequence used for (In,Ga)N/GaN NW heterostructures.

7.2 Strain and chemical composition

Figure 7.3(a) shows a bright-field TEM micrograph of a single GaN NW top with two (In,Ga)N insertions stacked along the (0001) growth direction. The insertions do not stretch through the entire nanowire base and thus are fully embedded within the GaN NW matrix. The dark (In,Ga)N insertions are surrounded by brighter contours which reveal an important strain within the heterostructure.

The determination of the local In content is far from being straightforward. X-ray diffraction may be used as an analytical tool, but requires a very homogeneous NW distribution, as it usually can only probe an ensemble of nanoscale objects. A further technique relies on the analysis of the elastic strain state of the layers using, for instance, the geometric phase analysis (GPA) of lattice fringes in high-resolution transmission electron microscopy (HRTEM) images.[86] This is, however, a quite complex method, where experimental conditions may cause severe artifacts of the evaluated strain and, consequently, of the In composition [87]. Thus, the combination of complementary experimental techniques supported by theoretical calculations appears a crucial point.

In order to probe total strain and thereby indirectly the chemical composition profile within the NWs, we have applied high-resolution x-ray diffraction close to the GaN(0002) reciprocal lattice point. The respective measurements have been performed at beamline ID01 at the European Synchrotron Radiation Facility using an x-ray energy of 8 keV with an energy resolution $\Delta E/E$ of 10^{-4} [88].

Figure 7.3(b) shows an $\omega/2\theta$ scan (along the surface normal) through the

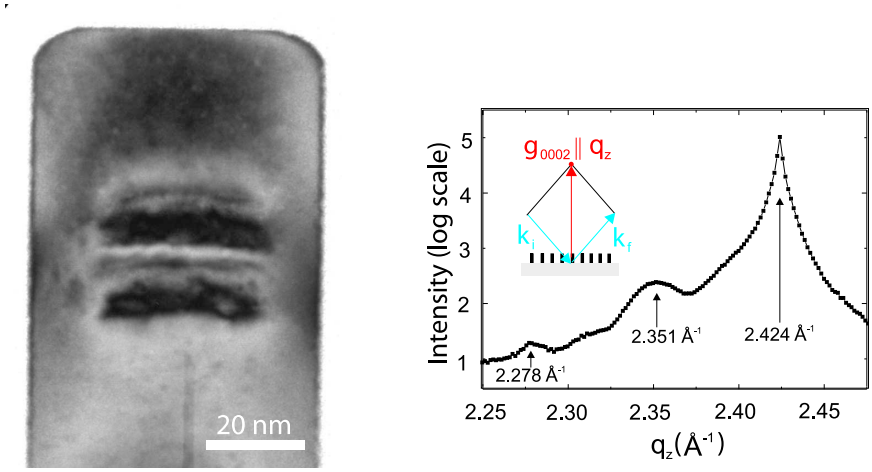

(a) **(b)**

Figure 7.3 – Growth of embedded (In,Ga)N/GaN NW heterostructures: (a) Cross-sectional TEM micrograph of an as-grown NW. The micrograph reveals two vertically stacked embedded (In,Ga)N insertions in the GaN NW matrix. (b) Out-of-plane HRXRD near the GaN(0002) lattice point probing an ensemble of (In,Ga)N/GaN NWs. Three different vertical lattice constants are observed corresponding to pure wurtzite GaN, and (In,Ga)N with a relative In content of 19% and 39%. Fig. (b) by M. Hanke [85].

GaN(0002) reflection. Three different peaks are observed at q_z = 2.278Å, 2.351Å and 2.424Å^{-1}, respectively. The most intense one at q_z=2.424Å^{-1} stems from the GaN(0002) reflection. The two additional peaks are tentatively attributed to the embedded (In,Ga)N insertions, as the three peaks show similar distributions in the in-plane q_x direction **(not shown here)**. The corresponding vertical lattice constants are $c_\perp$=$4\pi/q_z$=5.345Å and 5.516Å, respectively. The In content can be calculated by the relation of in-plane ($\varepsilon_{xx} = \varepsilon_{yy} = \varepsilon_\parallel$) and out-of-plane ($\varepsilon_{zz} = \varepsilon_p$) elastic strain:

$$\varepsilon_p = \frac{c_p - c_{\mathrm{InGaN}(x)}}{c_{\mathrm{InGaN}}(x)} = -\frac{2C_{13}(x)}{C_{33}(x)} \times \frac{a_\parallel - a_{\mathrm{InGaN}}(x)}{a_{\mathrm{InGaN}}(x)} = -\frac{2C_{13}}{C_{33}}\varepsilon_\parallel \qquad (7.1)$$

where c_{InGaN} and a_{InGaN} are the bulk lattice constants and C_{13} and C_{33} are the elastic constants of (In,Ga)N both of which are assumed to obey Vegard's law. Assuming, furthermore, fully strained (In,Ga)N defined by $a_\parallel = a_{\mathrm{GaN}}$, the lattice constants measured correspond to In contents of 19% and 39%, respectively.

7.2.1 Geometric Phase Analysis (GPA)

The above interpretation of the $\omega/2\theta$ scan is rather simple. From the growth parameters of the structure, a single In content would be expected, however x-ray analysis indicates a more complex chemical composition. To get further insight into the structural and compositional configuration of the (In,Ga)N insertions, cross-sectional HRTEM was carried out on selected NWs. Samples were prepared by mechanical lapping and polishing, followed by Ar ion-milling according to standard techniques. HRTEM was performed in the $[11\bar{2}0]$ zone axis. Images of (0002) lattice fringes were obtained by tilting the sample about 3-4° around the $[1\bar{1}00]$ direction away from the zone axis (see fig. 7.4a).

Several dozens of NWs were investigated, that all exhibited two stacked (In,Ga)N insertions with a high uniformity in size and shape. A TEM micrograph of a typical NW is shown in fig 7.3a. It contains two (In,Ga)N insertions with 11 nm in height and about 30 nm in diameter, located at approximately 300 nm of NW length from the substrate. The (In,Ga)N insertions exhibit flat [0001] bottom and top facets and vertical $[1\bar{1}00]$ side facets. The insertions are fully embedded in the GaN matrix and coherently strained as no plastic relaxation has been observed by HRTEM.

The evaluation of the strain state from lattice fringes is performed using the LADIA software [89, 90], which contains a subroutine for GPA [91–93]. The analysis includes the following steps: (i) a Bragg spot, e. g., (0002),

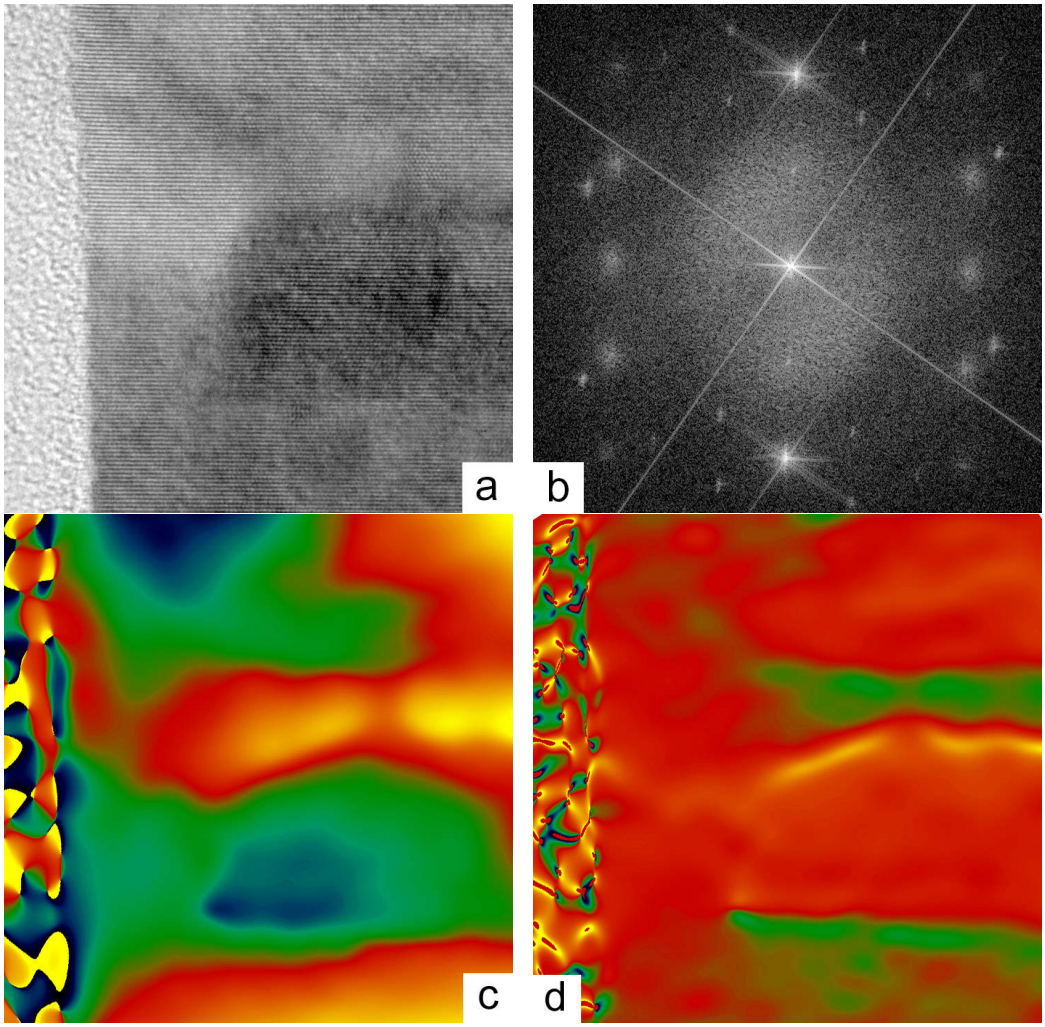

Figure 7.4 – Geometrical Phase Analysis (GPA) on an embedded (In,Ga)N/GaN NW heterostructure: (a) The original HRTEM image, (b) Diffraction pattern of the HRTEM image, revealing two bright (0002) spots, (c) Phase map of the filtered and inverse fourier-transformed image, (d) Final strain map.

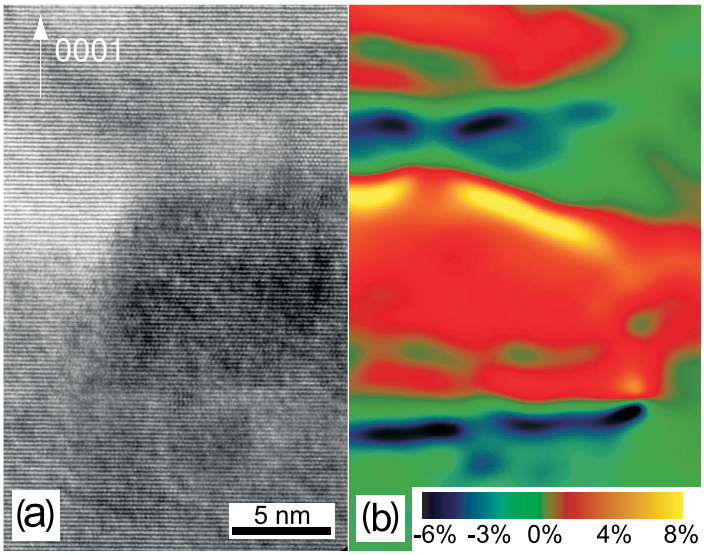

Figure 7.5 – HRTEM based strain analysis of embedded (In,Ga)N insertions in a GaN NW: (a) HRTEM image of one (In,Ga)N insertion. The picture has been taken slightly off-axis so as to strengthen the (0002) lattice fringes. (b) GPA strain mapping based on the electron micrograph on the left side (laterally reversed for displaying purposes).Fig. (b) by E. Luna [85].

is selected from the Fourier spectrum of the experimental image with an exponential mask and moved to the center of the Fourier spectrum, (ii) an inverse Fourier transform is performed on the selected Bragg spot and the phase of the transformation is displayed, (iii) the differential of the phase is calculated along the direction normal to the image fringes. This differential value corresponds to the misfit strain in this direction. Because an (0002) spot is selected in step (i), the estimated difference in lattice plane distance will be along the [0001] direction. Hence, the misfit strain is given by

$$\epsilon_p^{\mathrm{GPA}} = \frac{\Delta c_{\mathrm{GaN}}}{c_{\mathrm{GaN}}} = \frac{c_p - c_{\mathrm{GaN}}}{c_{\mathrm{GaN}}}, \tag{7.2}$$

where c_{GaN} is the GaN lattice constant.

Figure 7.5(b) shows a mapping of $\Delta c/c$ in a single GaN NW with two (In,Ga)N insertions. The two (In,Ga)N insertions are compressively strained indicated by the red color as compared to the unstrained GaN NW matrix represented in green. The mean compressive strain at the central part of the insertion is about 3% . The misfit strain measured by GPA can be expressed as:

$$\epsilon_p^{\mathrm{GPA}} = \frac{c_{\mathrm{InGaN}}(x)}{c_{\mathrm{GaN}}} \left[1 - \frac{2C_{13}(x)}{C_{33}(x)} \left(\frac{a_{\mathrm{GaN}} - a_{\mathrm{InGaN}}(x)}{a_{\mathrm{InGaN}}(x)} \right) \right] - 1 \tag{7.3}$$

from where the In mole fraction x can be inferred. C_{ij} denote the elastic constants [94]. Assuming Vegard's law for both lattice parameters $a_{\mathrm{InGaN}}(x)$ and $c_{\mathrm{InGaN}}(x)$, this corresponds to a relative In content of $18\% \pm 3\%$ and is thus in good agreement with the In content derived by HRXRD.

Interestingly, the GaN lattice close to the (In,Ga)N insertion is subject to a tensile strain as indicated by the blue color. The c lattice constant of GaN between the vertical sidewalls of the (In,Ga)N insertions and that of the NWs themselves is larger than the unstrained GaN reference lattice constant. This dilation is a result of the pseudomorphic overgrowth of the (In,Ga)N sidewalls.

The top region of the (In,Ga)N insertions exhibits a very high compressive strain, much higher than the rest of the insertions, as indicated by the yellow color in fig. 7.5b. The (compressive) misfit strain of this region amounts to about 7%, corresponding to a mean relative In content of $41\% \pm 3\%$, which is in good agreement with the XRD result. As the highly In-rich region expands over the top facet of the insertion, namely the growth front during NW growth, this local concentration of In is probably caused by In surface segregation as described in ref. [95]: a liquid In layer segregates at the growth front during (In,Ga)N deposition. This surface segregation of In also explains

why the (In,Ga)N insertion is so much thicker than the GaN barriers despite their equal growth times. As the In supply is interrupted during the growth of GaN on top of the insertion, the In incorporation is enhanced due to even N-richer conditions, resulting in the high In-content at the top of the (In,Ga)N insertion shown in Fig. 7.5(b) by the yellow *hat-like* area.

Besides the described In growth front segregation, the (In,Ga)N insertions are found to be of very homogeneous In content and no clusters are formed. This is noteworthy as In clustering is a serious issue in the 2D InGaN growth, where gross discontinuities and compositional variations within the 2D quantum layers are found on a 20-100 nm length scale [96]. The strong vertical and lateral limitation of the (In,Ga)N insertions dimensions within the NW seems not to allow the clusters to form. Thus, the NW geometry is an interesting technique tu improve the material quality of (In,Ga)N heterostructures.

The results obtained by applying the GPA method on HRTEM image are in very good agreement with the In content derived from HRXRD investigation. However, HRXRD only allows to analyze an ensemble of NWs at the same time, whereas HRTEM may only be carried out on very thin samples, thus analyzing a *quasi* 2D cut through a single NW. In order to comprehensively verify these results, a simulation by the Finite Element Method has been undertaken.

7.2.2 Finite Element Method (FEM)

Most analytical solutions of the misfit strain field suffer from their restriction to a particular type of low-dimensional structures. On the other hand, numerical FEM calculations may serve as a powerful alternative on the basis of linear elasticity theory, as they inherently enable the study of arbitrary morphologies and chemical composition profiles. So we have probed the impact of embedded vertical stacks of (In,Ga)N insertions on the misfit strain field within the insertions and the surrounding GaN matrix.

Based on the structural characterization by TEM and HRXRD, we simulate the misfit strain field (with the unstrained GaN matrix as a reference) for the NW shown in Fig. 7.6a, using the same lattice parameters and elastic constants as for GPA [94]. Due to the larger lattice parameter of the (In,Ga)N insertion as compared to the GaN matrix, the surrounding host lattice undergoes a tension between the insertions (vertical distortion < 0) and toward the sidewalls (both in-plane components of the distortion become negative). This observation is in good quantitative agreement with the TEM results shown Fig. 7.5. FEM simulations further predict that the GaN lattice appears undisturbed at vertical separations comparable to the thickness of the insertion. It is remarkable that the abrupt vertical concentration

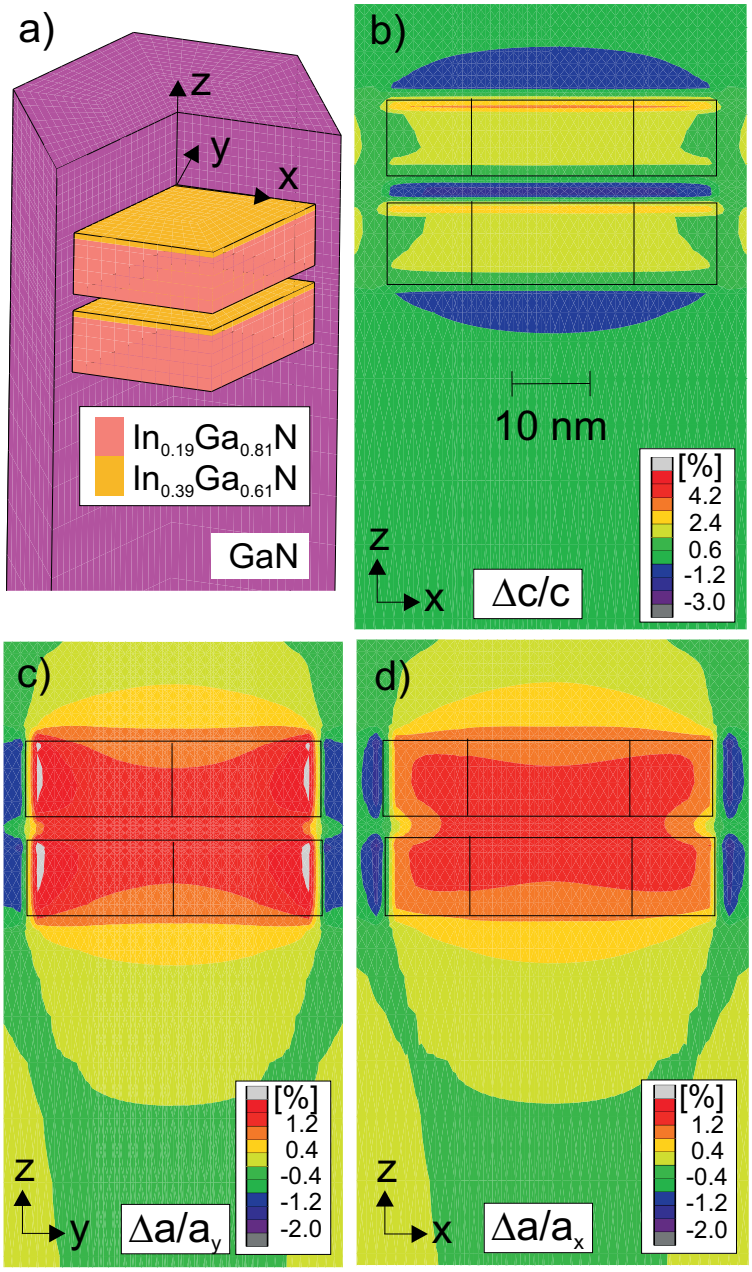

Figure 7.6 – The NW model (a) used for the finite element calculation considers two identical subsequently stacked (In,Ga)N insertions in GaN. Each of the two (In,Ga)N insertions consist of 2 nm $In_{0.39}Ga_{0.61}N$ and 9 nm $In_{0.19}Ga_{0.81}N$ within a 20nm thick GaN shell. The GaN barrier inbetween the insertions is 3 nm thick. Numerical results for the misfit strain are shown for two high symmetry planes: (b) depicts the out-of-plane component $\Delta c/c$ within the xz-plane, while (c) and (d) give the corresponding in-plane values of $\Delta a/a$ within yz- and xz-planes. Figure by M. Hanke [85].

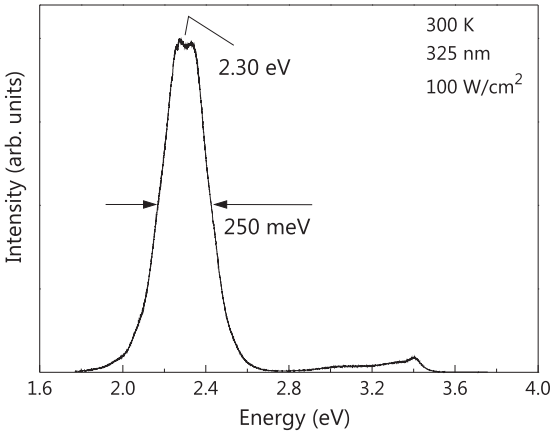

Figure 7.7 – Photoluminescence spectrum of (In,Ga)N/GaN NWs taken at 300 K. The spectrum was excited by the 325 nm line of a He-Cd laser with an excitation energy of 100 W.cm^{-2}. Figure by O. Brandt [85].

step from 19 to 39% In near the insertion apex mainly influences the vertical strain component shown in Fig. 7.6b, while the in-plane components in Figs. 7.6c and 7.6d remain basically unaffected. Therefore, in particular the vertical strain distribution (probed by a symmetric x-ray reflection as shown in Fig. 7.3b) may serve as a sensitive fingerprint to the chemical composition within the NWs.

The strain values obtained by FEM calculations differ slightly from the ones obtained by the GPA analysis. While the qualitative strain analysis is identical (a compression of the embedded (In,Ga)N insertions, and an according reaction of the surrounding GaN host matrix), the strain values do differ. The obtained *mean* strain at the center of an (In,Ga)N insertion is about 3% by GPA and about 2% by FEM. Likewise, the strain in the In-rich "hat" region is 7% by GPA and 5% by FEM. This discrepancy is due to the different sample premises: whereas FEM considers a free-standing three-dimensional NW, GPA is carried out on a TEM micrograph, taken on a thin slice of a NW, embedded in an epoxy matrix. This matrix is a further constraint to the NW, therefore leading to higher strain values.

7.3 Discussion

The photoluminescence (PL) spectrum of the as-grown NWs at room temperature is shown in fig. 7.7. The spectrum is dominated by an intense green emission at 2.30 eV (540 nm) due to the (In,Ga)N insertions, two orders of magnitude stronger than the free exciton line of GaN at 3.42 eV. The width

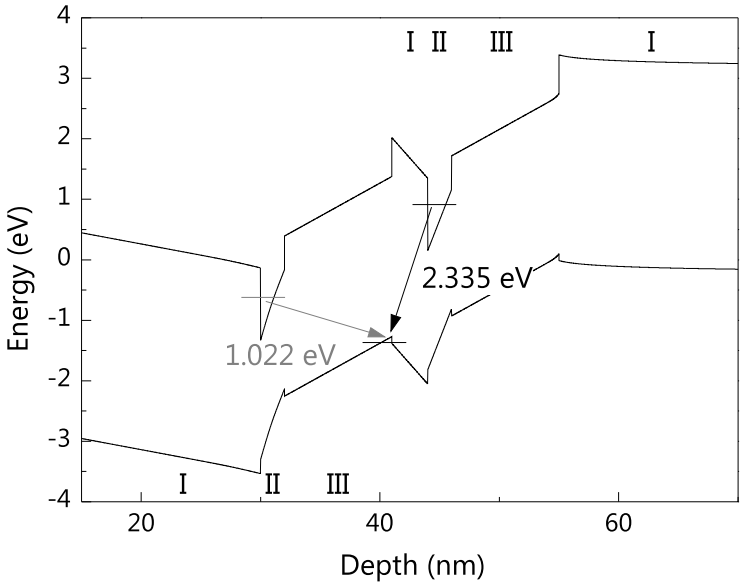

Figure 7.8 – Band profile and lowest-energy transitions between occupied states in the investigated (In,Ga)N/GaN NW as obtained by a solution of the one-dimensional Poisson-Schrödinger equations for the same-layer sequence as used for the FEM calculations in fig. 7.6 (I: GaN; II: $In_{0.39}Ga_{0.61}N$; III: $In_{0.19}Ga_{0.81}N$). Figure by L. Schrottke [85].

of this band amounts to 250 meV, not excessively broad even when compared to state-of-the-art 2D (In,Ga)N quantum wells emitting in a similar wavelength range.[97] This observation suggests that the size and composition of the (In,Ga)N insertions is surprisingly homogeneous and not overly affected by the wide NW diameter distribution.

We have performed the above HRTEM analysis for many individual NWs, and can thus be sure that the dimensions deduced are indeed representative for the entire NW ensemble. For these dimensions, however, it is difficult to understand both wavelength and intensity of the emission observed and displayed in Fig. 7.7, as we would expect a significantly longer wavelength and a very much suppressed emission due to the quantum confined Stark effect. For definitively clarifying this situation, we would need a calculation of the transition energies and wave functions of the three-dimensional structure depicted in Fig. 7.6. As a first order approximation, we obtain the transition energies for a structure identical in layer sequence to the one above by a one-dimensional self-consistent Schrödinger-Poisson calculation [84], thus entirely ignoring the complex strain-field (cf. fig. 7.6) and the resulting three-dimensional potential landscape in the actual structure. Figure 7.8 shows the

band profile and the two lowest energy transitions between occupied states calculated under these simplifying assumptions. Obviously, the lowest energy transition cannot account for the observed emission energy. In addition, the calculations show that the overlap between the electron and hole wavefunctions for this transition is essentially zero. In contrast, the overlap between the electron and hole wavefunctions for the higher-energy transition exhibits a finite value of 2.7×10^{-3} due to the thin barrier between the two (In,Ga)N insertions. We thus tentatively attribute the emission observed in fig. 7.7 to an *inter-well* rather than an intra-well transition, as illustrated in fig. 7.8.

Chapter 8

Conclusion

The purpose of this work was to develop a detailed understanding of the growth process of GaN NWs and of the correlation between structural and physical properties.

GaN NWs were grown by plasma-assisted MBE on Si(111) substrates. The impinging nitrogen atoms will react with the Si surface to form an amorphous Si_xN_y interlayer, which will prohibit the epitaxial alignment of substrate and NWs. The resulting NW tilt causes the NW to coalesce. The structural and optical properties of coalesced NWs have been studied, showing that coalescence induces two major strucural defets: boundary dislocations and I_1-type stacking faults. We have *locally* investigated the luminescence of single NWs, revealing that dislocations cause a severe loss of optical output, but that I_1-type stacking faults have a very characteristic luminescence emission at 3.24 eV. Interestingly, the top of the coalesced NW is shown to be nearly defect-free, which makes controlled NW coalescence an interesting growth method to obtain high quality bulk GaN material.

GaN NWs can be *epitaxially* grown on Si(111) by growing a thin AlN buffer layer prior to deposition. We have investigated the growth process of GaN NWs on an AlN buffer layer combining *in situ* RHEED analysis and *ex situ* HRTEM. The growth process is initially governed by the nucleation of dislocation-free coherent islands. As growth proceeds, these coherent islands undergo a series of shape transitions in order to elastically relax the lattice-mismatch-induced strain. The final shape transition towards the NW geometry is shown to be governed by the nucleation of a misfit dislocation at the AlN/GaN interface within a pyramid-shaped island. The drastic change of total free energy associated with the dislocation nucleation is identified as the driving force for this final shape transition. The initial diameter of catalyst-free epitaxial NWs is thus equal to the critical diameter for plastic relaxation of a full-pyramid shaped island.

(In,Ga)N insertions embedded in GaN NW heterostructures were grown by plasma-assisted MBE. High-resolution XRD in combination with a geometric phase analysis of HRTEM images was used to plot an In incorporation and strain profile of the NW heterostructure. It was shown that the In distribution inside the (In,Ga)N insertios was not homogeneous along the growth direction, instead the top region was found to be more In-rich, due to In segregation during the NW growth process. No plastic relaxation at the (In,Ga)N/GaN interface was found, so FEM simulations were calculated, revealing that the (In,Ga)N quantum dots are coherently strained within the NW. The (In,Ga)N/GaN heterostructures showed a strong PL emission at 2.3 eV, which could not be associated to the (In,Ga)N inclusion's dimensions. We therefore propose a band model suggesting a inter-well recombination through the GaN barrier between two stacked (In,Ga)N inclusions. Thus, we have established a method to precisely analyze strain and chemical composition in (In,Ga)N/GaN NW heterostructures. This analysis has led to the observation of In segregation during growth and to the discovery of an alternative carrier recombination in stacked (In,Ga)N/GaN NW heterostructures.

Outlook

The investigation of GaN NW coalescence has shown that it allows the growth of high quality material on largely lattice-mismatched substrates. Therefore the controlled coalescence of GaN NWs during growth may be a suitable technique to grow GaN bulk material on cheap substrates like silicon.

The growth model established for the epitaxial growth of GaN NWs on an AlN buffer has shown that the lattice-mismatched-induced strain is the main driving force for NW nucleation and that the initial NW diameter is defined by this very mismatch. Therefore, NW diameter control should be possible by choosing the substrate and thus the lattice mismatch accordingly.

Whereas the work on (In,Ga)N/GaN NW heterostructures has not solved the issue of controlling the In incorporation, it has shown the important strain fields involved in this kind of heterostructures. As the strain has a direct influence on the quantum dots geometry, which subsequently may change the preferred recombination method used within the NW, the investigation of this issue should be continued, namely using the information gained by FEM for future structural analyses so as to reach a profound understanding of In incorporation, a necessary step on the way to controlling it.

Appendix

InGaN growth experiments

List of growth experiments for InGaN/GaN NW heterostructures as referred to in section 7.1, page 88.

Sample	Growth Temp.	V/III	In/Ga (nom.)
8857*	—	6.4	0
8859	600	5.3	24.1
8860	600	5.3	17.5
8868	600	5.3	16.8
8871	600	5.3	1.1
8872**	600	5.9	2.0
8873	650	5.9	2.0
8874	650	5.9	0.9
8875	650	5.9	0.5
8878	600	5.9	1.1

Table 1 – Growth parameters used for embedded InGaN/GaN NW heterostructures. *) Sample 8857 is a GaN reference sample. **) Sample 8872 is the only one emitting a PL signal characteristic for InGaN.

Acknowledgements

This work would not have been possible without the contribution of many people, some of which I would like to thank here:

I would like to thank Prof. Klaus Ploog and Prof. Henning Riechert for giving me the opportunity to work at PDI and for their compelling enthusiasm for the NW cause. I am greatly indebted to Prof. Ted W. Masselink and Prof. Andreas Waag for kindly accepting to refer this work. I am thankful to Studienstiftung des Deutschen Volkes for financial support of my research.

I would like to thank all my colleagues and co-workes at PDI, especially Oliver Brandt for his valuable help with optical and XRD characterization, as well as for his help on MBE growth, Michael Hanke for HRXRD investigation and FEM simulations, Lutz Schrottke for his contribution to the InGaN band profile, Esperanza Luna for contributing to the TEM and GPA analysis, Uwe Jahn for CL experiments, Lutz Geelhaar for many fruitful discussions, Hans-Peter Schönherr and Claudia Herrmann for MBE maintenance, Doreen Steffen and Astrid Pfeiffer for TEM maintenance and sample preparation, and everybody else who made my stay at PDI a very comfortable one.

My very special thanks go to Vincent Consonni, whom I had the pleasure to collaborate closely with on a major part of my work, many of the results published here wouldn't have been possible without his help and advice.

I would like to thank Achim Trampert for his advice and friendship and for not letting me abandon the thesis on so many occasions. Without his constant support, my work simply wouldn't have been possible.

Finally I'd like to thank my wife Julia for her support, especially reminding me about my soon-to-be-finished thesis on a regular basis.

Bibliography

[1] E. F. Schubert. *Light Emitting Diodes*. Cambridge Univ. Press, 2006.

[2] MA Sanchez-Garcia, E Calleja, E Monroy, FJ Sanchez, F Calle, E Munoz, and R Beresford. *J. Cryst. Growth*, 183(1-2):23–30, JAN 1998.

[3] M. Yoshizawa, A. Kikuchi, N. Fujita, K. Kushi, H. Sasamoto, and K. Kishino. *J. Cryst. Growth*, 189/190:138, 1998.

[4] S Guha, NA Bojarczuk, MAL Johnson, and JF Schetzina. *Appl. Phys. Lett.*, 75(4):463–465, JUL 26 1999.

[5] E. Calleja, M. A. Sánchez-García, F. Sánchez, F. Calle, F. B. Naranjo, E. Muñoz, S. I. Molina, A. M. Sánchez, F. J. Pacheco, and R. García. *J. Cryst. Growth*, 201/202:296, 1999.

[6] E Calleja, MA Sanchez-Garcia, FJ Sanchez, F Calle, FB Naranjo, E Munoz, U Jahn, and K Ploog. *Phys. Rev. B*, 62(24):16826–16834, DEC 15 2000.

[7] Raffaella Calarco, Ralph J. Meijers, Ratan K. Debnath, Toma Stoica, Eli Sutter, and Hans. Luth. *Nano Lett.*, 7(8):2248–2251, AUG 2007. doi: 10.1021/nl0707398.

[8] A. Kikuchi, M. Kawai, M. Tada, and K. Kishino. *Jap. J. Appl. Phys.*, 43:L1524, 2004.

[9] H. Sekiguchi, K. Kato, J. Tanaka, A. Kikuchi, and K. Kishino. *Phys. stat. sol. (a)*, 205:1067, 2008.

[10] R. S. Wagner and W. C. Ellis. *Appl. Phys. Lett.*, 4:89, 1964.

[11] U. Jahn, J. Ristic, and E. Calleja. *Appl. Phys. Lett.*, 90:161117, 2007.

[12] T. Kouno, A. Kikuchi, and K. Kishino. *Phys. stat. sol. (b)*, 243:1481, 2006.

[13] Y. Saito, N. Teraguchi, A. Suzuki, T. Araki, and Y. Nanishi. *Jpn. J. Appl. Phys.*, 40:L91, 2001.

[14] H. Sekiguchi, K. Kishino, and A. Kikuchi. *Appl. Phys. Lett.*, 96:231104, 2010.

[15] A. F. Wright. *J. Appl. Phys.*, 82:2833, 1997.

[16] A. Trampert, J. Ristic, U. Jahn, and K. H. Ploog. *Inst. Phys. Conf. Ser.*, 180:167, 2003.

[17] D. Hull and D. J. Bacon. *Introduction to dislocations*. Robert Maxwell, Liverpool, UK, 1984.

[18] G. W. Sears. *Act. Metall.*, 1:457, 1953.

[19] G. A. Bootsma and H. J. Gassen. *J. Cryst. Growth*, 10:223, 1971.

[20] E. I. Givargizov. *J. Cryst. Growth*, 31:20, 1975.

[21] E. Calleja, M. A. Sánchez-García, F. Calle, F. B. Naranjo, E. Muñoz, U. Jahn, K. H. Ploog, J. Sánchez, J. M. Calleja, K. Saarinen, and P. Hautojarvi. *Mater. Sci. Eng. B*, 82:2, 2001.

[22] J. Grandal, M. A. Sánchez-García, F. Calle, and E. Calleja. *phys. stat. sol. (c)*, 2:2289, 2005.

[23] J. Ristic, E. Calleja, M. A. Sánchez-García, J. M. Ulloa, J. Sánchez-Páramo, J. M. Calleja, A. Trampert, U. Jahn, and K. H. Ploog. *Phys. Rev. B*, 68:125305, 2003.

[24] J. R. Arthur. *Surface Science*, 500:189, 2002.

[25] F. C. Frank and J. H. van der Merwe. *Proc. R. Soc. A*, 198:205, 1948.

[26] M. Volmer and A. Weber. *Zeit. Phys. Chemie*, 119(277), 1926.

[27] I. N. Stranski and L. von Krastanow. *Abhandlungen der Mathematisch-Naturwissenschaftlichen Klasse*, volume 146. Akademie der Wis. und Lit. Mainz, 1939.

[28] A Ichimiya and P. I. Cohen. *Reflection high-energy electron diffraction*. Cambridge University Press, Cambridge, UK, 2004.

[29] J. Klein. *Epitaktische Heterostrukturen aus dotierten Magnaten.* PhD thesis, Univ. of Cologne, 2001.

[30] wwwex.physik.uni ulm.de.

[31] P. B. Hirsch, A. Howie, R. B. Nocholson, D. W. Pashley, and M. J. Whelan. *Electron microscopy of thin crystals.* London Butter Worths, Oxford, UK, 1965.

[32] L. Reimer. *Transmission Electron Microscopy.* Springer Verlag, Berlin, Germany, 1984.

[33] O. Brandt, R. Muralidharan, P. Waltereit, A. Thamm, A. Trampert, H. von Kiedrowski, and K. H. Ploog. *Appl. Phys. Lett.*, 75:4019, 1999.

[34] KA Bertness, A Roshko, NA Sanford, JM Barker, and A Davydov. *J. Cryst. Growth*, 287(2):522–527, JAN 25 2006. doi: 10.1016/j.jcrysgro.2005.11.079.

[35] G. Koblmüller, P. Pongratz, R. Averbeck, and H. Riechert. *Appl. Phys. Lett.*, 80:2281, 2002.

[36] C. Chèze, L. Geelhaar, A. Trampert, and H. Riechert. *Appl. Phys. Lett.*, 97:043101, 2010.

[37] C. Chèze, L. Geelhaar, O. Brandt, W. Weber, H. Riechert, S. Münch, R. Rothemund, S. Reitzenstein, A. Forchel, T. Kehagias, P. Kominou, G. P. Dimitrakopulos, and T. Karakostas. *Nano Res.*, 3:528, 2010.

[38] L. Lymperakis and J. Neugebauer. *Phys. Rev. B*, 79:241308(R), 2009.

[39] O. Brandt, C. Pfüller, C. Chèze, L. Geelhaar, and H. Riechert. *Phys. Rev. B*, 81:045302, 2010.

[40] V. Bougrov, M. E. Levnshtein, S. L. Rumyantsev, and A. Zubrilov. *Properties of Advanced Semiconductor Materials GaN, AlN, InN, BN, SiC, SiGe*, pages 1–30. John Wiley & Sons, Inc., New York, 2001.

[41] F. A. Ponce, D. Cherns, W. T. Young, and J. W. Steeds. *Appl. Phys. Lett.*, 69:770, 1996.

[42] V. L. Petrov. *Phys. stat. sol. (a)*, 133:189, 1992.

[43] W. J. Moore, J. A. Freitas, S. K. Lee, S. S. Park, and J. Y. Han. *Phys. Rev. B*, 65:081201, 2002.

[44] M. A. Reshchikov and J. Morkoc. *J. Appl. Phys.*, 97:061301, 2005.

[45] R. Liu, A. Bell, F. A. Ponce, C. Q. Chen, J. W. Yang, and M. A. Khan. *Appl. Phys. Lett.*, 86:021908, 2005.

[46] R. Songmuang, O. Landre, and B. Daudin. *APPLIED PHYSICS LETTERS*, 91(25), DEC 17 2007. doi: 10.1063/1.2817941.

[47] S. Férnandez-Garrido, J. Grandal, E. Calleja, M. A. Sánchez-García, and D. López-Romero. *J. Appl. Phys.*, 106:126102, 2009.

[48] D. Cherns, L. Meshi, I. Griffiths, S. Khongphetsak, S. V. Novikov, R. P. Campion, C. T. Foxon, C. Liu, P. Shields, and W. N. Wang. *J. Phys: Conf. Ser.*, 209:012001, 2009.

[49] V. G. Dubrovskii, I. P. Soshnikov, N. V. Sibirev, G. É. Cirlin, V. M. Ustinove, M. Tchernycheva, and J. C. Harmand. *Semiconductors*, 41: 865, 2007.

[50] R. K. Debnath, T. Stoica, A. Besmehn, K. Jeganathan, E. Sutter, R. Meijers, H. Lüth, and R. Calarco. *J. Cryst. Growth*, 311:3389, 2009.

[51] E. Calleja, J. Ristić, S. Fernández-Garrido, L. Cerutti, M. A. Sánchez-García, J. Grandal, A. Trampert, U. Jahn, G. Sánchez, A. Griol, and B. Sánchez. *Phys. stat. sol. (b)*, 244:2816, 2007.

[52] J. H. Edgar. *Properties of Group III Nitrides*. EMIS, London, UK, 1994.

[53] O. Landré, C. Bougerol, H. Renevier, and B. Daudin. *Nanotechnology*, 20:415602, 2009.

[54] G Mula, C Adelmann, S Moehl, J Oullier, and B Daudin. *Phys. Rev. B*, 64(19), NOV 15 2001.

[55] B Daudin, F Widmann, G Feuillet, Y Samson, M Arlery, and JL Rouviere. *Phys. Rev. B*, 56(12):R7069–R7072, SEP 15 1997.

[56] B. Daudin. *J. Phys.: Condens. Matter*, 20:473201, 2009.

[57] I Daruka, J Tersoff, and AL Barabasi. *Phys. Rev. Lett.*, 82(13):2753–2756, MAR 29 1999.

[58] J. H. van der Merwe. *Appl. Phys. Lett.*, 34:117, 1963.

[59] J. W. Matthews and A. E. Blakeslee. *J. Cryst. Growth*, 27:118, 1974.

[60] Toma Stoica, Eli Sutter, Ralph J. Meijers, Ratan K. Debnath, Raffaella Calarco, Hans Lueth, and Detlev Gruetzmacher. *SMALL*, 4(6):751–754, JUN 2008. doi: 10.1002/smll.200700936.

[61] K. Tillmann and A. Förster. *Thin Solid Films*, 368:93, 2000.

[62] Frank Glas. *Phys. Rev. B*, 74(12), SEP 2006. doi: 10.1103/PhysRevB.74.121302.

[63] R. B. Schwarz, K. Khachaturian, and E. R. Weber. *Appl. Phys. Lett.*, 70:1122, 1997.

[64] H. T. Johnson and L. B. Freund. *J. Appl. Phys.*, 81:6081, 1997.

[65] S. Guha, A. Madhukar, and K. C. Rajkumar. *Appl. Phys. Lett.*, 57: 2110, 1990.

[66] B. J. Spencer and J. Tersoff. *Phys. Rev. B*, 63:205424, 2001.

[67] A. Marzegalli, V. A. Zinovyev, F. Montalenti, A. Rastelli, M. Stoffel, T. Merdzhanova, O. G. Shmidt, and L. Miglio. *Phys. Rev. Lett.*, 99: 235505, 2007.

[68] J Tersoff and F. K. Legoues. *Phys. Rev. Lett.*, 72:3570, 1994.

[69] J. Tersoff, B. J. Spencer, A. Rastelli, and H. von Känel. *Phys. Rev. Lett.*, 89:196104, 2002.

[70] V. A. Shchukin, N. N. Ledentsov, P. S. Kop'ev, and D. Bimberg. *Phys. Rev. Lett.*, 75:2968, 1995.

[71] V. A. Shchukin and D. Bimberg. *Rev. Mod. Phys.*, 71:1125, 199.

[72] J. E. Northrup and J. Neugebauer. *Phys. Rev. B*, 53:R10477, 1996.

[73] J. E. Northrup, J. Neugebauer, R. M. Feenstra, and A. R. Smith. *Phys. Rev. B*, 61:9932, 2000.

[74] C. T. Foxon, S. V. Novikov, J. L. Hall, R. P. Campion, D. Cherns, I. Griffiths, and S. Khongphetsak. *J. Cryst. Growth*, 311:3423, 2009.

[75] M Yoshizawa, A Kikuchi, M Mori, N Fujita, and K Kishino. *Jap. J. Appl. Phys.*, 36(4B):L459–L462, APR 15 1997.

[76] R Meijers, T Richter, R Calarco, T Stoica, HP Bochem, M Marso, and H Luth. *J. Cryst. Growth*, 289(1):381–386, MAR 15 2006. doi: 10.1016/j.jcrysgro.2005.11.117.

[77] A. R. Smith, Feenstra. R. M., D. W. Greve, J. Neugebauer, and J. E. Northrup. *Phys. Rev. Lett.*, 79:3934, 1997.

[78] W. Guo, M. Zhang, A. Banerjee, and P. Bhattacharya. *Nano Lett.*, 10: 3355, 2010.

[79] H.-W. Lin, Y.-J. Lu, H.-Y. Chen, H.-M. Lee, and S. Gwo. *Appl. Phys. Lett.*, 97:073101, 2010.

[80] R. Bardoux, A. Kaneta, M. Funato, Y. Kawakami, A. Kikuchi, and K. Kishino. *Phys. Rev. B*, 79:155307, 2009.

[81] Y. S. Park, M. J. Holmes, T. W. Kwang, and R. A. Taylor. *Nanotechnol.*, 21:115401, 2010.

[82] R. Armitage and K. Tsubaki. *Nanotechnol.*, 21:195202, 2010.

[83] Y.-L. Chang, J. L. Wang, F. Li, and Z. Mi. *Appl. Phys. Lett.*, 96:013106, 2010.

[84] P. Waltereit, O. Brandt, J. Ringling, and K. H. Ploog. *Phys. Rev. B*, 64:245305, 2001.

[85] M. Knelangen, M. Hanke, E. Luna, L. Schrottke, O. Brandt, and A. Trampert. *Nanotechnology*, 22:365703, 2010.

[86] S. Kret, P. Dluzewski, A. Szczepanska, M. Zak, R. Czernecki, M. Krysko, M. Leszczynski, and G. Maciejewski. *Nanotechnol.*, 18:465707, 2007.

[87] A. Rosenauer, D. Gerthsen, and V. Potin. *Phys. stat. sol. (a)*, 203:176, 2006.

[88] Experiment carried out by Michael Hanke, 2010.

[89] K. Du, Y. Rau, N. Y. Jin-Phillipp, and F. Phillipp. *J. Mat. Sc. & Technol.*, 18:135, 2002.

[90] K. Du and F. Phillipp. *J. Microsc.*, 221:63, 2006.

[91] M. J. Hÿtch. *Scanning Microsc.*, 11:53, 1997.

[92] M. J. Hÿtch, E. Snoeck, and R. Kilaas. *Ultramicrosc.*, 74:131, 1998.

[93] M. J. Hÿtch, J. Putaux, and J. Pénisson. *Nature*, 423:270, 2003.

[94] I. Vurgaftman and J. R. Meyer. *J. Appl. Phys.*, 94:3675, 2003.

[95] P. Waltereit, O. Brandt, M. A. Tagliente, L. Tapfer, and K. H. Ploog. *Phys. Rev. B*, 66:165322, 2002.

[96] M. J. Galtrey, R. A. Oliver, M. J. Kappers, C. McAleese, D. Zhu, C. J. Humphreys, P. H. Clifton, D. Larson, and A. Cerezo. *Appl. Phys. Lett.*, 92:041904, 2008.

[97] C. Skierbiszewskia, M. Siekacz, P. Wiśniewski, P. Perlin, A. Feduniewicz-Zmuda, G. Cywiński, J. Smalc, S. Grzanka, I. Grzegory, M. Leszczyński, and S. Porowski. *Acta Phys. Pol. A*, 110:345, 2006.

[98] E. F. Schubert. Light-Emittind Diodes. www.LightEmittingDiodes.org.

List of Figures

Selbständigkeitserklärung

Ich versichere, daß ich die vorliegende Doktorarbeit selbständig angefertigt und keine anderen als die angegebenen Quellen und Hilfsmittel benutzt habe. Alle Stellen, die wörtlich oder sinngemäß aus veröffentlichen und nicht veröffentlichen Schriften entnommen sind, habe ich als solche kenntlich gemacht. Die Doktorarbeit hat keiner anderen Prüfungsbehörde vorgelegen.

Halle (Saale), im August 2012

Matthias Knelangen